

## Horizon 2020

Space Call - Earth Observation: EO-3-2016: Evolution of Copernicus services  
Grant Agreement No. 730008

# ECoLaSS

## Evolution of Copernicus Land Services based on Sentinel data



## D11.2

### "D41.1b – Prototype Report: Time Series-derived Indicators and Variables (Issue 2)"

Issue/Rev.: 2.0

Date Issued: 24.12.2019

submitted by:



in collaboration with the consortium partners:



submitted to:



European Commission – Research Executive Agency

This project has received funding from the European Union's Horizon 2020 Research and Innovation Programme, under Grant Agreement No. 730008.

## CONSORTIUM PARTNERS

No.	PARTICIPANT ORGANISATION NAME	SHORT NAME	CITY, COUNTRY
1	GAF AG	GAF	Munich, Germany
2	Systèmes d'Information à Référence Spatiale SAS	SIRS	Villeneuve d'Ascq, France
3	JOANNEUM RESEARCH Forschungsgesellschaft mbH	JR	Graz, Austria
4	Université catholique de Louvain, Earth and Life Institute (ELI)	UCL	Louvain-la-Neuve, Belgium
5	German Aerospace Center (DLR), German Remote Sensing Data Center (DFD), Wessling	DLR	Wessling, Germany

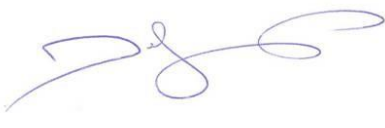
### CONTACT:

GAF AG  
Arnulfstr. 199 – D-80634 München – Germany  
Phone: ++49 (0)89 121528 0 – FAX: ++49 (0)89 121528 79  
E-mail: copernicus@gaf.de – Internet: www.gaf.de

### DISCLAIMER:

The contents of this document are the copyright of GAF AG and Partners. It is released by GAF AG on the condition that it will not be copied in whole, in section or otherwise reproduced (whether by photographic, reprographic or any other method) and that the contents thereof shall not be divulged to any other person other than of the addressed (save to the other authorised officers of their organisation having a need to know such contents, for the purpose of which disclosure is made by GAF AG) without prior consent of GAF AG. Nevertheless single or common copyrights of the contributing partners remain unconditionally unaffected.

### DOCUMENT RELEASE SHEET

	<b>NAME, FUNCTION</b>	<b>DATE</b>	<b>SIGNATURE</b>
Author(s):	Pierre Defourny (UCL) Omar Ali Eweys (UCL) Thomas De Maet (UCL) Matthieu Taymans (UCL) Jolan Wolter (UCL) Annekatrin Metz-Marconcini (DLR) Benjamin Leutner (DLR) Nicolas Ekicier (SIRS) Antoine Masse (SIRS) Sophie Villerot (SIRS)	16.12.2019	
Review:	Sophie Villerot (SIRS)	20.12.2019	
Approval:	Eva Sevillano Marco (GAF)	24.12.2019	
Acceptance:	Massimo Ciscato (REA)		
Distribution:	ECoLaSS project consortium; Project Officer and European Commission Services		

### DISSEMINATION LEVEL

<b>DISSEMINATION LEVEL</b>		
PU	Public	X
CO	Confidential: only for members of the consortium (including the Commission Services)	

### DOCUMENT STATUS SHEET

<b>ISSUE/REV</b>	<b>DATE</b>	<b>PAGE(S)</b>	<b>DESCRIPTION / CHANGES</b>
1.0	10.08.2018	58	First issue of the Prototype Report: Time Series-derived indicators and Variables
2.0	24.12.2019	65	Second issue with final results from implementation in phase 2.

## APPLICABLE DOCUMENTS

ID	DOCUMENT NAME / ISSUE DATE
AD01	Horizon 2020 Work Programme 2016 – 2017, 5 iii. Leadership in Enabling and Industrial Technologies – Space. Call: EO-3-2016: Evolution of Copernicus services. Issued: 13.10.2015
AD02	Guidance Document: Research Needs Of Copernicus Operational Services. Final Version issued: 30.10.2015
AD03	Proposal: Evolution of Copernicus Land Services based on Sentinel data. Proposal acronym: ECoLaSS, Proposal number: 730008. Submitted: 03.03.2016
AD04	Grant Agreement – ECoLaSS. Grant Agreement number: 730008 – ECoLaSS – H2020-EO-2016/H2020-EO-2016, Issued: 18.10.2016
AD05	D8.2: D33.1b - Methods Compendium: Time Series Analysis for Thematic Classification (Issue 2), Issued: December 2019
AD06	D15.2: D.45.1b – Prototype Report: New Land Cover/Land Use (LC/LU) Products (Issue 2), Issued: December 2019

## EXECUTIVE SUMMARY

The Horizon 2020 (H2020) project, “Evolution of Copernicus Land Services based on Sentinel data” (ECoLaSS) addresses the H2020 Work Programme 5 iii. Leadership in Enabling and Industrial technologies - Space, specifically the Topic EO-3-2016: Evolution of Copernicus services. ECoLaSS is being conducted from 2017–2019 and aims at developing and prototypically demonstrating selected innovative products and methods as candidates for future next-generation operational Copernicus Land Monitoring Service (CLMS) products of the pan-European and Global Components. ECoLaSS assesses the operational readiness of such candidate products and eventually suggests some of these for implementation. This shall enable the key CLMS stakeholders (i.e. mainly the Entrusted European Entities (EEE) EEA and JRC) to take informed decisions on potential procurement as (part of) the next generation of Copernicus Land services from 2020 onwards.

To achieve this goal, ECoLaSS makes full use of dense time series of High-Resolution (HR) Sentinel-2 optical and Sentinel-1 Synthetic Aperture Radar (SAR) data, complemented by Medium-Resolution (MR) Sentinel-3 optical data if needed and feasible. Rapidly evolving scientific developments as well as user requirements are continuously analysed in a close stakeholder interaction process, targeting a future pan-European roll-out of new/improved CLMS products, and assessing the potential transferability to global applications.

This report **D11.2 “D41.1b Time Series Derived Indicators and Variables”** constitutes methods developed and applied for the Work Package (WP) 41 of ECoLaSS Task 4 targeting filling the thematic gaps in the current Copernicus Land Service Portfolio of the phenology and Agriculture services. In particular, providing indicators and variables of high spatial resolution is targeted along with for improving one of the main pan-European Copernicus Land products, i.e. the current (2012) and future (2015, 2018) HRLs on Forest and Imperviousness, improving permanent grassland identification targeting the HRL Grassland 2015, monitoring crop area and crop status/parameter and providing novel LC/LU products serving a potential future Agricultural use.

The developed methods of this WP are generally introduced in section 1 of this report while the background and summary of requirements are given in section 2. Section 3 describes the Demonstration sites; (Demonstration West and South-Africa sites). Section 4 provides an over view of the applied methods for determining first generic land cover metrics, then crop growth conditions, and finally multiannual trends and potential changes for the specific changes of land covers, i.e. the HRL Grassland and Forest layers. Then, the prototype implementation is detailed in section 5 including descriptions of the integrated EO and ancillary data and pre-processing steps as well as presenting the actual prototype results in the Demonstration sites with the accuracy assessment. Finally, conclusion of the used methods and main results together with the main outlooks are provided in Section 6.

Main findings of WP show that using multi-year Landsat datasets is successful in computing the generic phenological metrics and, however, more frequent observations; mainly Sentinel-2 dataset; is highly demanded for better capturing the phenological behaviour by computing vegetation indices twice a month. Furthermore, the multi-annual trends and the potential changes are captured by designing a more targeted phenological product exploiting the density of Sentinel-1 time series for updating the Grassland and Forest HRLayers. However, the signal response to various elements other than change should be considered. In addition, the crop growth condition is developed and applied using the Leaf Area Index (LAI) biophysical variable derived from Sentinel-2 time series. LAI is analysed at the field level considering the neighbouring fields of the same crop (within a radius of 3 km) for Winter Wheat, Winter Barley and Maize. The resulting products enable identifying local marginal behaviour along the season in terms of crop growth cycle, crop development or management practices. Finally, the emergence date product for maize is determined based on a comprehensive methods benchmarking based on a large reference dataset collected on the ground form the South Africa Demonstration site. Among the applied methods, the relative threshold method is identified as the most suitable in terms of performance and robustness and applied to a large part of the Free State province (South Africa).

## Table of Contents

<b>1</b>	<b>INTRODUCTION .....</b>	<b>1</b>
<b>2</b>	<b>BACKGROUND AND SUMMARY OF REQUIREMENTS .....</b>	<b>2</b>
<b>3</b>	<b>DEMONSTRATION SITES.....</b>	<b>3</b>
3.1	ECoLaSS DEMONSTRATION SITES .....	3
3.2	DEMO-SITE WEST FOR GENERIC LC METRICS, CROP GROWTH CONDITION, EMERGENCE DATE, MULTIANNUAL TRENDS AND POTENTIAL CHANGES .....	4
3.3	DEMO-SITE SOUTH AFRICA FOR EMERGENCE DATE DETECTION .....	5
3.4	DEMO-SITE SOUTH-WEST FOR GENERIC LC METRICS .....	7
3.5	DEMO-SITE CENTRAL FOR GENERIC LC METRICS .....	8
<b>4</b>	<b>OVERVIEW OF APPLIED METHODS.....</b>	<b>10</b>
4.1	METHOD FOR GENERIC LC METRICS.....	10
4.2	METHOD FOR CROP GROWTH CONDITION .....	11
4.3	METHOD FOR MULTIANNUAL TRENDS AND POTENTIAL CHANGES BASED ON SAR DATA FROM S-1.....	12
4.3.1	Pre-processing on the input data .....	12
4.3.2	Statistical analysis of seasonal and annual metrics within the HRL classes to identify potential change 16	
4.4	METHODS FOR EMERGENCE DATE DETECTION .....	17
4.4.1	Emergence date as phenological parameter .....	18
4.4.2	VIs and hue time series as candidate data sources .....	18
4.4.3	Candidate detection methods .....	19
4.4.4	Performance indicators .....	23
<b>5</b>	<b>PROTOTYPE IMPLEMENTATION.....</b>	<b>24</b>
5.1	INPUT DATA, PRE-PROCESSING AND DATA INTEGRATION .....	24
5.1.1	Generic LC metrics .....	24
5.1.2	Crop growth condition anomaly .....	25
5.1.3	Emergence date detection .....	25
5.1.4	Multiannual trends and potential changes.....	28
5.2	RESULTS AND VALIDATION .....	30
5.2.1	Generic LC metrics .....	30
5.2.2	Crop growth condition .....	37
5.2.3	Multiannual trends and potential changes based on SAR data from S-1 .....	44
5.2.4	Emergence date detection .....	50
5.3	PROTOTYPE SPECIFICATIONS .....	57
<b>6</b>	<b>CONCLUSION AND OUTLOOK .....</b>	<b>64</b>
<b>REFERENCES.....</b>		<b>66</b>

## List of Figures and Tables

Figure 3-1: European Demonstration Sites ( <i>Map: © European Environment Agency; administrative boundaries: ©EuroGeographics</i> ).....	3
Figure 3-2: Overview of demonstration site West, draped over CLC dataset.....	5
Figure 3-3: Location of the Free State in South Africa and mean annual rainfall in mm in South Africa (1950-2000) (Schulze, 2007).....	6
Figure 3-4: Demonstration site in the Free State (South-Africa) corresponding to a 310x100 km east-west transect covered by three Sentinel-2 tiles .....	6
Figure 3-5:: Demonstration site South-West, with CLC 2018 background layer ( <i>©European Environment Agency, © EuroGeographics for the administrative boundaries</i> ) .....	8
Figure 3-6 - Overview of the demonstration-site Central draped over the CORINE Land Cover classes (2018). .....	9
Figure 4-1: Sentinel-2 tiles for Belgium test site and harmonized grassland HRL of 2015 .....	13
Figure 4-2: Examples of temporal S-1 metrics: Backscattering temporal statistics of 2015 of the S-1 relative orbit 161 in ascending pass over the BELGIUM demo site: (a) backscattering temporal mean, (b) backscattering temporal standard deviation, (c) backscattering temporal minimum, (d) backscattering temporal maximum (outlines of S-2 granules in yellow) .....	15
Figure 4-3: Workflow for identification of potential pixels for update within a certain HRL .....	17
Figure 4-4: Four methods based on the NDVI to detect start and end of the season. a) fixed threshold, b) derivative, c) Fourier transform, d) quadratic fitting based on AGDD (de Beurs and Henebry, 2010).....	20
Figure 4-5: Overview of the six emergence estimation methods. Methods without parameterization: (a) inflection point,(b) base logistic (c) maximumvalue. Methods with parameterization: (d) highest slope, (e) absolute threshold, (f) relative threshold. The threshold methods are both tested on the linear and logistic interpolated observations. Presented vegetation profiles are examples from the maize calibration sample .....	22
Figure 5-1: Available satellite images (not fully clouded): (a) 35JMK and 35JNK (left) tiles; (b) 35JNK (right) and 35JPK .....	26
Figure 5-2: Illustration of the PICES field boundary layer, in the Free State. Background image are the NDVI pixel value on the 15th of January 2017. NDVI values are multiplied by 1000 .....	27
Figure 5-3: Linking field observation and field delineation by the intersection of a 20-m inner field border buffer with a 120-m circle buffer around each observation. Background image shows the NDVI pixel value on the 15th of January 2017. NDVI values are multiplied by 1000 .....	28
Figure 5-4: Histogram of emergence dates, aggregated per week of the year for the planting window for maize in 2016-2017 .....	28
Figure 5-5: K-Means resulting image, with 30 classes, based on the maximal NDVI values for a year. The white dots being no data due to the presence of clouds.....	31
Figure 5-6: 3 classes exhibiting no seasonal variations during the year .....	33
Figure 5-7: 9 first following classes as listed by the clustering algorithm - the NDVI is much higher and variable than for the 'no-season' classes .....	34
Figure 5-8: 9 second following classes as listed by the clustering algorithm - the NDVI is much higher and variable than for the 'no-season' classes .....	34
Figure 5-9: 9 last following classes as listed by the clustering algorithm - the NDVI is much higher and variable than for the 'no-season' classes .....	35
Figure 5-10: Classes displaying mowing events at various months of the year .....	35
Figure 5-11: Layers generated by the reclassification: PSS (phenological start of season), PPS (phenological peak of season), PES (phenological end of season) and PLS (phenological length of season) .....	36
Figure 5-12 - Various classes of phenological activity over the T32TNT tile from the Central demsonstration site. The coherence of the landscape can clearly be seen. ....	37
Figure 5-13: Characterisation of the crop growth condition of six different maize parcels for 2017. The orange LAI profile corresponds to the local average of all the maize fields within a radius of 3 km, excluding the field of interest plotted here in blue .....	38

Figure 5-14: Characterisation of the crop growth condition of six different winter wheat parcels for 2017. The orange LAI profile corresponds to the local average of all the maize fields within a radius of 3 km, excluding the field of interest plotted here in blue .....	39
Figure 5-15: Characterisation of the crop growth condition of six different winter barley parcels for 2017. The orange LAI profile corresponds to the local average of all the maize fields within a radius of 3 km, excluding the field of interest plotted here in blue .....	40
Figure 5-16: Distribution of the local LAI anomalies for the three main crops in 2017. The anomaly corresponds to the difference between the area under LAI curve for the field of interest and the one for the local average .....	41
Figure 5-17: Map zooms of the maize anomalies for 2017 .....	41
Figure 5-18: Map zooms of the winter wheat anomalies for 2017 .....	42
Figure 5-19: Map zooms of the winter barley anomalies for 2017.....	42
Figure 5-20: Distribution of the 2018 local LAI anomalies in the demo-site West (Wallonia) expressed as the cumulative LAI difference for the vegetative period (min LAI to max LAI) between the field of interest and the local LAI average of the wheat fields within 3km radius around the given field.....	43
Figure 5-21: Spatial distribution of the local LAI anomalies for the 2018 wheat season (demo-site West, Wallonia) .....	43
Figure 5-22: First example of HRL grass updates for three consecutive years. Above: background layer for visual comparison of surrounding land cover. Below: detected pixels for possible update.....	44
Figure 5-23: Second example of HRL grass updates for three consecutive years. Above: background layer for visual comparison of surrounding land cover. Below: detected pixels for possible update .....	45
Figure 5-24: Identified pixels (in %) for update across three years of the demosite for HRL grass. Stable and not change pixels (green), category 1 for update (yellow), category 2 for update (red).....	46
Figure 5-25 Overview over the TSI Grassland aggregate layers 2016-2019 for the demonstration sites West and Central. Note that the appearance of high percentage grassland cover is due to overview resampling for better display at the large scale of this figure. ....	46
Figure 5-26 Proportion of HRL grassland pixels belonging to one of the TSI change classes for the Central site (left) and the West site (right). .....	47
Figure 5-27 Temporal development of the Grassland TSI over three consecutive years as well as their fusion into the more robust aggregated 2016 – 2019 TSI in the demonstration site Central.....	48
Figure 5-28: First example of HRL forest updates for three consecutive years. Above: background layer for visual comparison of surrounding land cover. Below: detected pixels for possible update .....	48
Figure 5-29: Second example of HRL forest updates for three consecutive years. Above: background layer for visual comparison of surrounding land cover. Below: detected pixels for possible update .....	49
Figure 5-30: Third example of HRL forest updates for three consecutive years. Above: background layer for visual comparison of surrounding land cover. Below: detected pixels for possible update .....	49
Figure 5-31: Emergence date map for maize in the Free State (South-Africa). A strong gradient of emergence date is highlighted from east to west.....	53
Figure 5-32: Within field emergence date provided at pixel level for six maize fields of the Free State. ..	54
Figure 5-33: Temporal dynamics of the MSAVI index for the 2016-2017 (red) and 2015-2016 (black) growth seasons. Results are presented for the relative threshold method on logistic interpolation .....	55
Figure 5-34: Profile of five maize fields showing the MSAVI average value at field level, the maximum slope point and the detected emergence dates. ....	56
Figure 5-35: Spatial distribution of the maize emergence date in 2018 for the demo-site West (Belgian tiles). ....	57

Table 3-1: Description of the selected Prototype Sites .....	4
Table 5-1: List of the optical and thermal bands of Landsat-8.....	24
Table 5-2: Calculated TSI prototypes.....	29
Table 5-3: Phenological parameters (start, peak, end and length of season) manually determined for each of the 30 classes, as well as mowing event appearances .....	32
Table 5-4: Comparison of the calibration and monthly samples for all methods for MSAVI .....	51

Table 5-5 Sunflower results for all estimation methods. Results are expressed in days. Results for LAI on logistic interpolation are not presented. The min/bias row corresponds for the calibration sample to the indicator (SD or MAD) which is minimized while bias is the difference between the zero-mean expected validation and validation emergence date estimation.....	55
Table 5-6: Detailed specifications for primary CGC status layer of the demonstration site West .....	60
Table 5-7: Detailed specifications for primary CED status layer of the demonstration site South-Africa ..	61
Table 5-8: Detailed specifications for PHL of the demonstration site South-West.....	62
Table 5-9: Detailed specifications for the Time Series Indicator prototypes.....	63
Table 5-10: Colour palette for the probability layers.....	64

## Abbreviations

AGDD	Accumulated Growing Degree Days
AOI	Area of Interest
BBCH	Biologische Bundesanstalt und Bundessortenamt und Chemische Industrie
CLC	Corine Land Cover
CLMS	Copernicus Land Monitoring Service
CSDM	Canopy Structure Dynamic Model
DEM	Digital Elevation Model
ECoLaSS	Evolution of Copernicus Land Services based on Sentinel data
EEA	European Environment Agency
EEE	Entrusted European Entities
EO	Earth Observation
FAPAR	Fraction of Absorbed Photosynthetically Active Radiation
FOR	Forest
GAI	Green Area Index
GRA	Grassland
H2020	Horizon 2020
HRL	High Resolution Layer
JJA	June, July, August
JRC	Joint Research Centre
L1TP	L1T Collection
LAI	Leaf Area Index
LC/LU	land Cover/Land Use
LPIS	Land Parcel Identification System
MAD	Median absolute deviation
MAM	March, April May
MIR	Mid-Infrared
MMA	Maximal Monthly Activity
MPA	Maximal Phenological Activity
MSAVI	Modified Soil-adjusted Vegetation Index
NDVI	Normalized Difference Vegetation Index
NDWI	Normalized Difference Water Index
NIR	Near Infrared
OLI	Operational Land Imager
PCA	Principal Component Analysis
PES	Phenological End of Season
PICES	Producer Independent Crop Estimate System
PLS	phenological length of season
PPS	phenological peak of season
PSS	phenological start of season
S-1	Sentinel-1
S-2	Sentinel-2
S-3	Sentinel-3
SAR	Synthetic Aperture Radar
SD	Standard deviation
SON	September, October, November
SWIR	Short Cavelength Infrared
TIRS	Thermal Infrared
TOA	Top of Atmosphere
VIs	Vegetation Indices
WBS	Work Breakdown Structure

WP

Work Package

WPD

Work Package Description

## 1 Introduction

The Horizon 2020 (H2020) project, “Evolution of Copernicus Land Services based on Sentinel data” (ECoLaSS) addresses the H2020 Work Programme 5 iii. Leadership in Enabling and Industrial technologies - Space, specifically the Topic EO-3-2016: Evolution of Copernicus services. ECoLaSS is being conducted from 2017–2019 and aims at developing and prototypically demonstrating selected innovative products and methods as candidates for future next-generation operational Copernicus Land Monitoring Service (CLMS) products of the pan-European and Global Components. ECoLaSS assesses the operational readiness of such candidate products and eventually suggests some of these for implementation. This shall enable the key CLMS stakeholders (i.e. mainly the Entrusted European Entities (EEE) EEA and JRC) to take informed decisions on potential procurement as (part of) the next generation of Copernicus Land services from 2020 onwards.

To achieve this goal, ECoLaSS makes full use of dense time series of High-Resolution (HR) Sentinel-2 optical and Sentinel-1 Synthetic Aperture Radar (SAR) data, complemented by Medium-Resolution (MR) Sentinel-3 optical data if needed and feasible. Rapidly evolving scientific developments as well as user requirements are continuously analysed in a close stakeholder interaction process, targeting a future pan-European roll-out of new/improved CLMS products, and assessing the potential transferability to global applications.

This Deliverable **D11.2: “D.41.1b – Prototype Report: Time series-derived Indicators and Variables”** aims to develop the potential thematic exploitation of time series analysis derived from Sentinel time series. As such it is part of WP 41 of Task 4: “Thematic Proof-of-Concept/Prototype on Continental/Global Scale”. This report will be accompanied by the Deliverable **D11.4: “P.41.2b – Data Sets of Time series-derived Indicators and Variables”**. This report serves as documentation for the prototype dataset.

In the ECoLaSS project a prototype is defined as a prototypic / thematic proof-of-concept implementation of an improved or newly defined potential future Copernicus Land layer, building on the methods and processing lines developed in Task 3. The consortium has selected representative demonstration sites both in Europe and Africa, covering various bio-geographic regions and biomes. All prototype products and services are being prototypically implemented in a selection of these sites in the frame of the Task 4 WPs. In ECoLaSS, proofs-of-concept / prototype demonstration are carried out with respect to five topics of relevance: (i) Time series derived indicators and variables, (ii) Incremental Updates of HR Layers, (iii) Improved permanent grassland identification, (iv) Crop area and crop status / parameters monitoring, and (v) New LC/LU products. This deliverable focusses on the prototype “Time series derived indicators and variables” as part of WP 41.

This report comprises a Chapter on the background to phenology requirements (Chapter 2); a description of the Demonstration Sites where the prototypes are implemented (Chapter 3); an overview of the methodologies carried over from the testing and benchmarking in Task 3 (Chapter 4); followed by a Chapter on the prototype implementation itself, the results and validation, including a description of the dataset (Chapter 5); and a summary and outlook (Chapter 6).

## 2 Background and Summary of Requirements

After first methods have been tested and assessed by the Task 3 WPs (Deliverables D31.1a, D32.1a, D33.1a, D34.1a, D35.1a) in various test sites and algorithms have been described, the demonstration activities of Task 4 will commence to set up the developed processing lines in demonstration sites and derive first prototype versions. This will comprise establishing prototypes for: (i) deriving indicators and variables both for Continental and Global Component products and services from high-volume time series data with high spatial resolution and temporal repeat frequency; (ii) improving one of the main pan-European Copernicus Land products, i.e. the current (2012) and future (2015, 2018) HRLs on Forest and Imperviousness by developing incremental update strategies and ensuring time series consistency; (iii) improved permanent grassland identification targeting the HRL Grassland 2015 improvement; (iv) crop area and crop status/parameters monitoring targeting a potential future Agricultural service; as well as (v) further novel LC/LU products, e.g. as tested in Task 3.

The project will base all its developments on regularly updated high-priority user requirements, and assess/benchmark all operational product candidates in view of their innovation potential and technical excellence, automation level, potential for roll-out to pan-European level and/or global scale, timeliness for operational implementation, costs versus benefits, etc. (further elaborations will be performed in Task 5).

As discussed in the Deliverable D3.2: “D21.1b – Service Evolution Requirements Report” of the WP 21 – Assessment of Service Evolution Requirements, the phenology and the agriculture services are two thematic gaps in the current Copernicus Land Service portfolio. As clearly expressed in this report, the most frequently voiced new service was a pan-European Agricultural Service, followed by a pan-European Phenology Layer. As expected, these two services are potentially interlinked as a key target is capturing the phenology of the different crop type also mapped by Sentinel data. There are already plans from EEA and in-house studies which might contain common phenology derivatives, such as start, duration and end of season. Furthermore, a Phenology layer appears also of key interest for the HRLs Grassland and Forest as well as for the Copernicus Global Component. Such a Phenology product would need to be harmonized to provide the same phenological parameters (e.g. start, duration, end of season, etc.).

The identification of phenological stages gives key information for, among others, primary production estimation and forecast, land management practices and/or a better discrimination of vegetation for land cover classification (Sakamoto et al., 2010; Chen et al., 2008). It also helps quantify and anticipate climate change spatio-temporal variations (Atzberger, 2013) and understand the seasonal carbon dioxide fluxes (Sakamoto et al., 2010; Chen et al., 2008). More specifically for agriculture, it could provide crop production statistics, crop rotation records, or precision farming timely and localized information (Vicente-Guijalba et al., 2014). Early warning systems, monitoring vegetation conditions at critical phenological stages, aim at improving food security especially in food-insecure regions (Sub-Saharan Africa, Eastern, Southern and South-East Asia, Central America, etc.) (Vintrou et al., 2014).

In essence, three main reasons to study phenological stages for agriculture can be underlined. Firstly, it helps detecting, quantifying and following agricultural practices or climate change at different scales (change monitoring purposes). Secondly, it allows for a better estimations of yields by integrating the phenological information into growth models (food-security and policy-making purposes). Thirdly, a large number of professional applications may rely on phenological stages information to improve agricultural practices, reduce cost, etc. (commercial purposes).

### 3 Demonstration Sites

All prototypes are implemented in selected representative demonstration sites, which cover various biogeographic regions and biomes. In particular, the north, central, west, south west and south east are respectively located in Sweden, Austria and Germany, Belgium and France, France and Bulgaria and Greece while the African sites are located in Mali and South Africa.

The Demonstration Site West (Belgium/France) was selected for the prototypes related to the phenological parameters retrieval and their use for detecting the HRL Grassland and Forest potential change. The Demonstration Sites West and South Africa were selected for the prototypes using time series analysis for agricultural purposes, i.e. relative crop conditions assessment and emergence date detection.

#### 3.1 ECoLaSS Demonstration Sites

The selected larger prototype sites (60,000/90,000 km<sup>2</sup> per prototype site) contain the 5 test sites from Task 3. These prototype sites are relevant in Task 4 for demonstrating the proposed candidates for a Copernicus Land Service Evolution roll-out on a larger scale. As shown in Figure 3-1, the pre-selected prototype sites cover the Atlantic and Continental zones (Source EEA: <http://www.eea.europa.eu/data-and-maps/data/biogeographical-regions-europe-3#tab-gis-data>) of the member and associated states of EEA-39. The selected prototype sites are located in the **North of Europe, in the Alpine/Central region, in the West, in the South-West and in the South-East of Europe**. All prototype products and services will be prototypically implemented in one or more prototype sites in project phase 1, and in three prototype sites in phase 2.

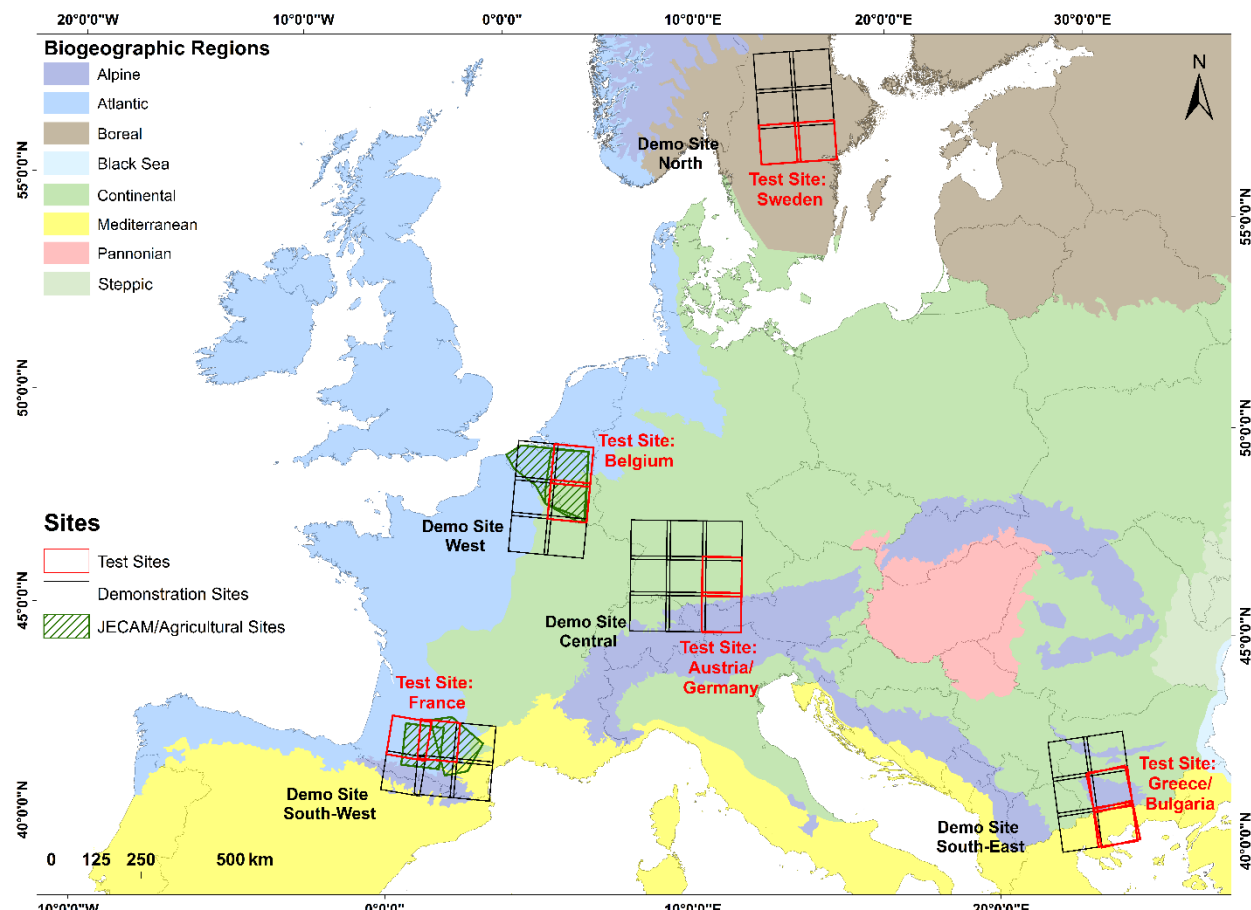


**Figure 3-1: European Demonstration Sites**  
 (Map: © European Environment Agency; administrative boundaries: ©EuroGeographics)

A short description of the different prototype sites is given in the following

Table 3-1:

**Table 3-1: Description of the selected Prototype Sites**

Location	Biogeographical region(s)	Countries	Distribution of CORINE land cover classes 2012 (Level 1) per prototype site *
Northern Europe	Boreal	Sweden, Norway	Artificial areas: 1.90%, Agricultural areas: 11.87%, Forest and semi-natural areas: 69.01%, Wetlands: 3.25%, Waterbodies: 13.94%
Alpine / Central Europe	Continental, Alpine	Germany, Austria, Switzerland, Italy and Czech Republic	Artificial areas: 9.03%, Agricultural areas: 44.55%, Forest and semi-natural areas: 44.65%, Wetlands: 0.23%, Waterbodies: 1.55%
West Europe	Atlantic, Continental	Belgium, France, Luxembourg	Artificial areas: 13.47%, Agricultural areas: 63.08%, Forest and semi-natural areas: 21.43%, Wetlands: 0.39%, Waterbodies: 1.61%
South-East Europe	Mediterranean, Continental, Alpine	Serbia, Macedonia, Greece, Bulgaria and Kosovo	Artificial areas: 3.34%, Agricultural areas: 34.87%, Forest and semi-natural areas: 56.67%, Wetlands: 0.17%, Waterbodies: 4.93%
South-West Europe	Atlantic, Mediterranean, Alpine	France, Spain	Artificial areas: 3.26%, Agricultural areas: 46.73%, Forest and semi-natural areas: 49.02%, Wetlands: 0.01%, Waterbodies: 0.40%

### **3.2 DEMO-SITE WEST for generic LC metrics, crop growth condition, emergence date, multiannual trends and potential changes**

The demonstration site “West” is the primary demonstration site for prototype developments of Task 4, related to the potential future Copernicus Land High Resolution Layer on Agricultural (AGRI), and as well for improvements of the HRL Grassland (GRA) and Forest (FOR). Phenological products, in particular “Phenological Start of Season” (PSS), “Phenological Peak of Season” (PPS), “Phenological End of Season” (PES), “Phenological Length of Season” (PLS) as well as “Maximal Phenological Activity” (MPA), have also been implemented on this site in the first phase only. However, due to the “artificial use” of Landsat-8 to simulate the full datasets brought by the twin satellites S-2 A and B, as well as the lack of validation, decision was made not to provide the prototype, that was deemed to experimental to meet the proper criteria required for operationability.

It contains the test site “Belgium” where methodological developments were studied in Task 3. This area has been also used for the prototype of local crop condition anomaly and crop emergence. A map of the selected demonstration site West is depicted in Figure 3-2. As summarized in Table 3-1, half of the surface of the demonstration site is used for agricultural purposes, a quarter is covered by water bodies, and the last quarter is divided between forests and semi-natural surfaces (13.15%), artificial areas (7.81%) and wetlands (0.25%).

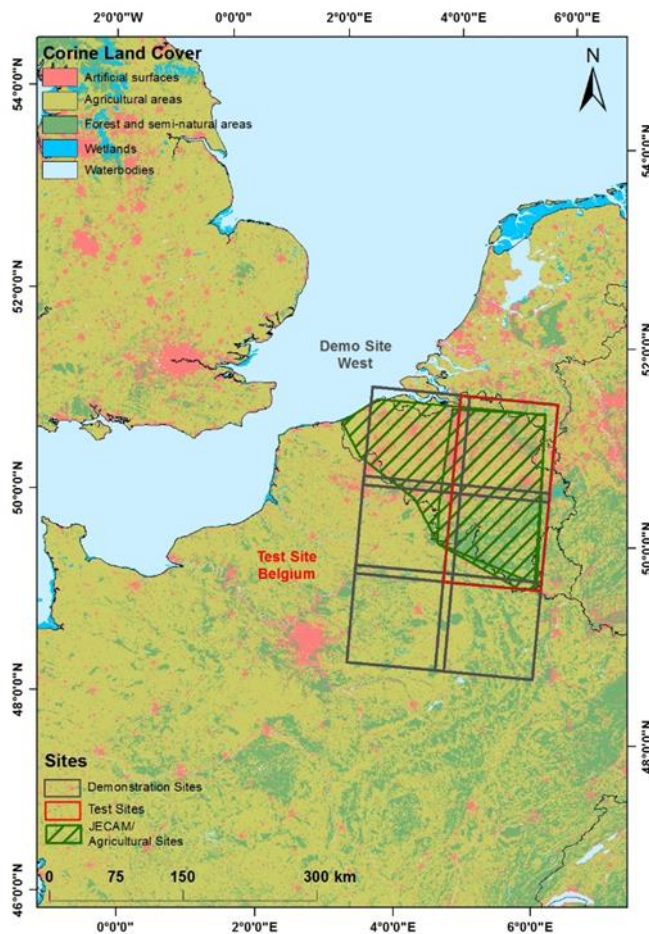


Figure 3-2: Overview of demonstration site West, draped over CLC dataset

### 3.3 DEMO-SITE SOUTH AFRICA for emergence date detection

The Southern African demo site refers to the third largest province in South Africa, named as the Free State and covering land area of approximately 129,825 km<sup>2</sup> (Figure 3-3). This province contributes significantly to the agricultural economy of the country, e.g. the provincial contribution (out of 9 provinces) of national maize production was 39% and 31% for the summer seasons 2014-2015 and 2015-2016 respectively. The main summer crops for the last decade in terms of area are: maize (69%), sunflower (17%), soybean (10%), sorghum (2%), drybeans (1%) and ground-beans (1%) (Department of Agriculture, 2017). Agriculture in the province depends greatly on rainfall, since only 4 to 8% of cultivated land is irrigated, with the exception of winter wheat (> 50% irrigation).

The Free State is included in South Africa's high-lying interior plateaux known as the *highveld* (Wiggs and Holmes, 2011). The province is divided into two parts of semi-arid and sub-humid climatic characteristics. Rainfall in the semi-arid part varies between 200 and 600 mm with a summer rainy season ranging from 100 to 180 days per year. The sub-humid part receive 400-800 mm rainfall per year and the corresponding rainy season spans from 180 to 240 days per year (Figure 3-3) (Jager et al., 1998). Frost occurs throughout the region usually from May to early September in the west and up to early October in the east. As much of South Africa, the Free State has low and erratic rainfall and water which are often a limiting factor for cultivation of food crops (Tsubo and Walker, 2007). Severe droughts affect the region. For instance, maize production dropped by 46% during the 2015-2016 growing season which was partially compensated by a 19% sunflower production increase (Department of Agriculture, 2017). Hence, annual maize production fluctuates significantly through the years with an average 127% inter-annual variation entirely explained by rainfall variability (Jager et al., 1998).

In this climatic context, agriculture in the western part of the Free State, is a more risky business because it is prone to more severe weather and environmental damages (drought, early frost, hail storms, etc.). Therefore, insurance companies propose specific multi-risk contracts and, thus, report field emergence at the field level to guarantee that the insured fields have correctly emerged. These field scale emergence reports together with an east-west transect capturing most of the agro-climatic gradient with three Sentinel-2 tiles (35JMK, 35JNK and 35JPK) (Figure 3-4) provide a complete demonstration of the Free State province.

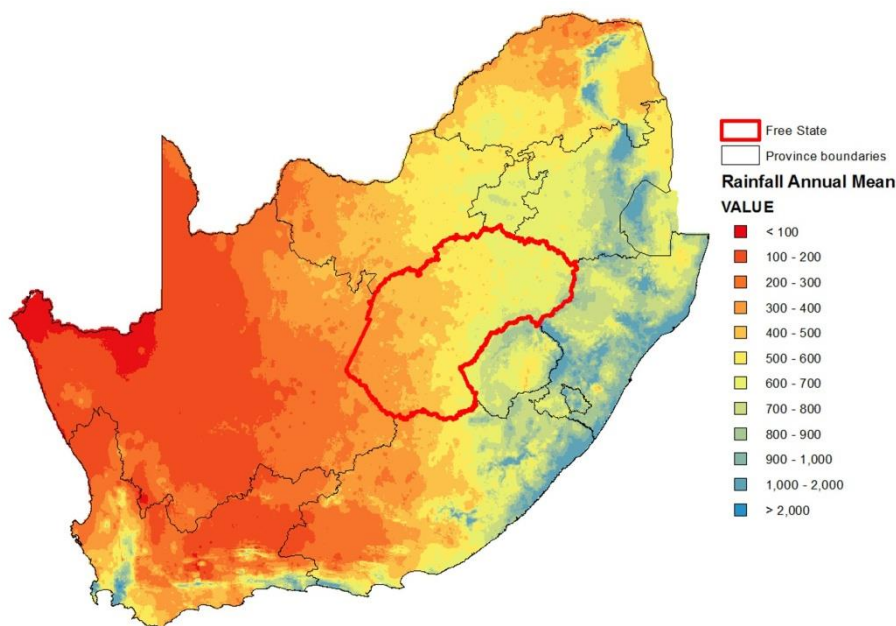


**Figure 3-3: Location of the Free State in South Africa and mean annual rainfall in mm in South Africa (1950-2000) (Schulze, 2007)**

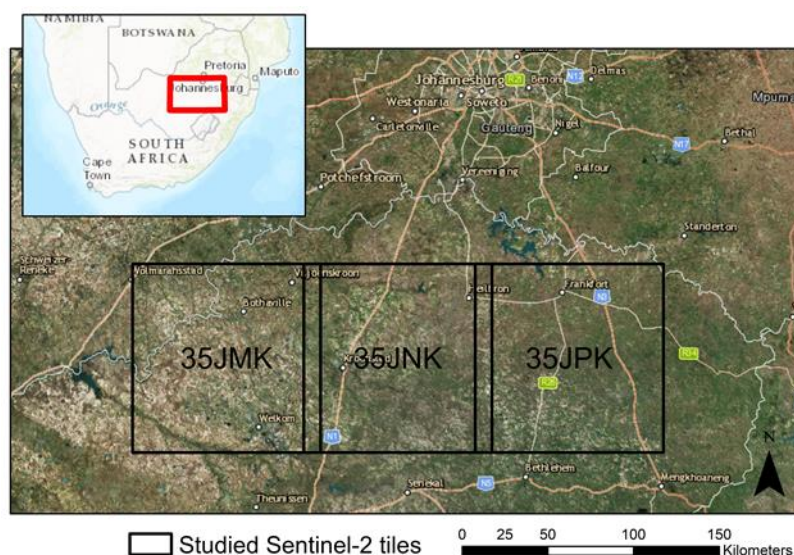


**Figure 3-4: Demonstration site in the Free State (South-Africa) corresponding to a 310x100 km east-west transect covered by three Sentinel-2 tiles**

### **3.4 DEMO-SITE SOUTH-WEST for generic LC metrics**

The demonstration site South-West (approx. 65,000 km<sup>2</sup>) is covering southern France and some parts of northern Spain, and includes the primary test site for the method developments in Task 3 related to the improvement of the HRL Imperviousness (IMP). It serves to demonstrate the implementation of the prototype of a potential future HRL Imperviousness, as part of WP 42, and the New Land Cover products, as part of WP45, in the first Reporting Period. In the second project phase, the demonstration sites Central and South-East have been added for the Imperviousness prototyping.

The landscape in the demonstration site South-West is composed of different biogeographic regions such as Mediterranean, Alpine and Atlantic. Three Sentinel-2 tiles are dominated by mountain landscapes, a mix of bare soils and natural grasslands, due to the presence of the Pyrenees. The 31TCJ tile is dominated by a strong proportion of impervious surfaces, because of Toulouse, a major French city. Toulouse is the 4<sup>th</sup> city in France in terms of urban and demographic expansions and is the most dynamic city of the South-West region. The presence of the city leads the region to be the second most attractive and dynamic region in France. The plains surrounding the city are mainly rurally dominated areas composed of croplands mixed with grassland and an increasing amount of forest with the proximity of the coastal region. But rurally dominated areas also show a dynamic increase of population and a dynamic situation of settlements due to the proximity of Toulouse. So the region shows a real tendency towards urban expansion in the surroundings of Toulouse and in the rural parts of the region with small cities like Montauban, Auch, Carcassonne, Tarbes, Castres or Albi. In general, the Mediterranean area in the East of the demonstration site is a patchwork of cropland, dry grassland and vineyards. There is also a small portion of the Landes forest in the North-West of the demonstration site. The unique situation of the region in terms of urban dynamic is the reason for the selection of this site for the Imperviousness prototype.

A more detailed map of the characteristics of the selected demonstration site South-West as used for the Imperviousness prototype is provided in Figure 3-5 below.

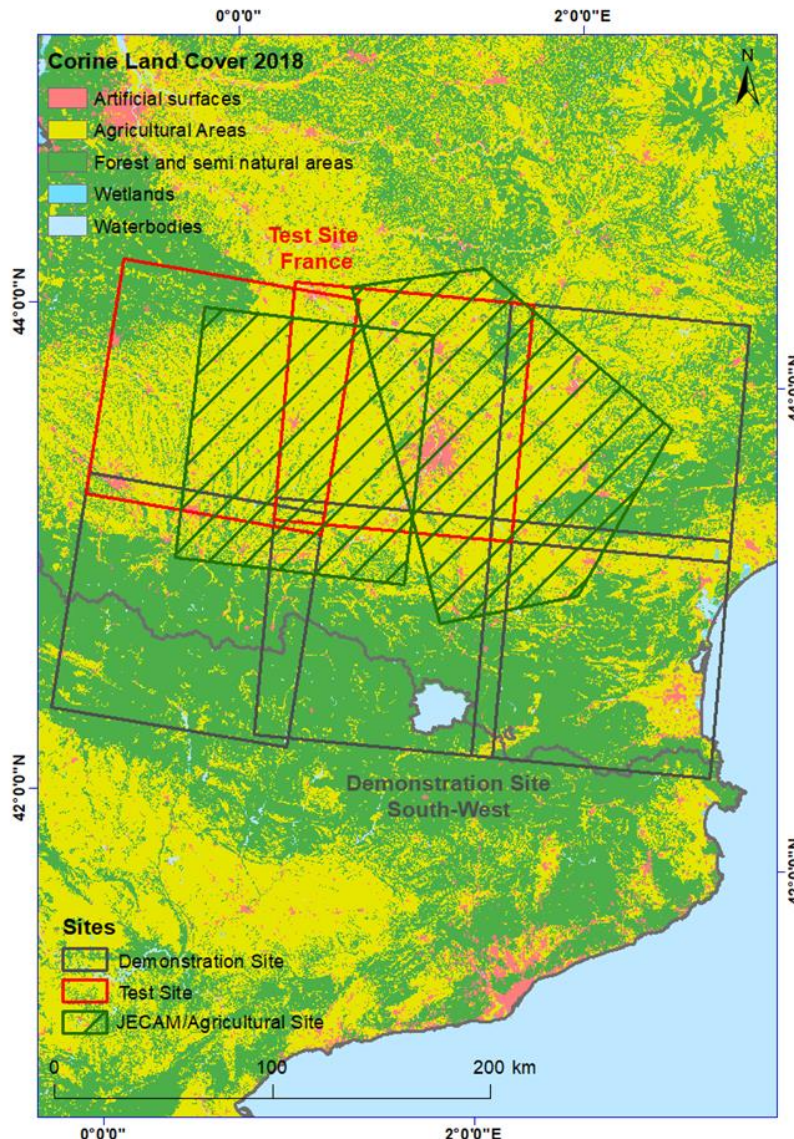


**Figure 3-5:: Demonstration site South-West, with CLC 2018 background layer**  
 (©European Environment Agency, © EuroGeographics for the administrative boundaries)

### 3.5 DEMO-SITE CENTRAL for generic LC metrics

The Demonstration Site Central covers the border region of Germany (mainly the provinces of Bayern and Baden-Wurttemberg), Austria (mainly the provinces of Tyrol and Vorarlberg), Switzerland as well as small areas of France, Italy, and Liechtenstein.

The Central demonstration site is characterized by cropland areas, mixed with permanent grassland (pastures). The adjoining part towards South, covering the foothills of the Bavarian Alps, is dominated (besides forest cover) by grasslands including specific grassland habitats and wetland types. Zones of alpine vegetation are included in the southern tiles, which contain also the Wetterstein mountain range as part of the Alps, stretching South down to the Inn valley. Lake Constance is also part of the Southern region as well as lower parts of Switzerland. Besides the Alps, the Black Forest area and the Vosges are regions at higher altitude, where forests and grassland predominate cropland.

The demo site has been chosen for crop mapping in order to test the classification approach under challenging but also realistic conditions:

- high diversity of crop categories

- heterogeneous regions (e.g. in Baden-Wurttemberg and Austria)
- strong topography (lowlands and high mountains).

Figure 3-6 shows the Central Demonstration site.

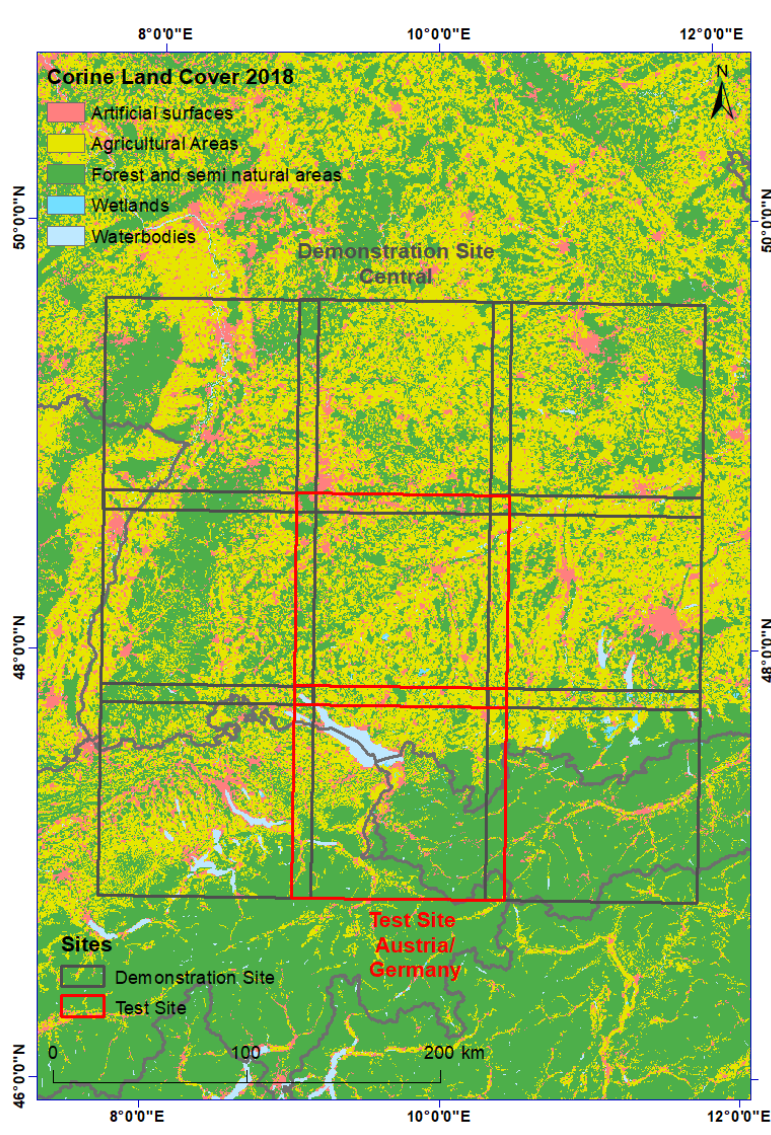


**Figure 3-6 - Overview of the demonstration-site Central draped over the CORINE Land Cover classes (2018).**

© European Union, Copernicus Land Monitoring Service 2012, European Environment Agency (EEA).

## 4 Overview of applied methods

This section presents methods developed and applied on the Demonstration site West for determining first generic land cover (LC) metrics (in the first phase only – the LC metrics were then applied over the Central and South-West demonstration sites), then crop growth conditions, and finally multiannual trends and potential changes for the specific changes of land covers, i.e. the HRL Grassland and Forest layers. The prototype dealing with the multiannual trends and potential change detection is based on S-1 time series. The method for the phenological prototype related to agriculture corresponds to the crop emergence date detection and is also described in this section. This will be applied on the Demonstration site South Africa and also implemented for the demo-site West.

### 4.1 Method for generic LC metrics

In this section, it is proposed to create experimental phenological products that includes several layers over the West demonstration site, that was produced only in the first phase, then over the Central and South-West sites for the second phase. This approach seeks to determine phenological parameters, such as “Phenological Start of Season” (PSS) or a “Maximal Monthly Activity” (MMA), based on robust series of dense multi-temporal images and derived phenological parameters, such as the spectral optical index NDVI. Based on the maximal monthly value of the NDVI, an unsupervised classification with an arbitrary number of classes is launched, in order to regroup pixels exhibiting the same phenological behavior. Parameters such as “Phenological Start of Season” (PSS), “Phenological Peak of Season” (PPS), “Phenological Length of Season” (PLS), are manually detected for each of those classes and the resulting images of the unsupervised classification is reclassified for each of those parameters.

#### Normalized Difference Vegetation Index or NDVI

The “Normalized Difference Vegetation Index” (Rouse 6r. et al., 1974; Tucker, 1979) is used as an indicator to monitor vegetation health and can be used as a proxy for photosynthetic activity, as detailed in WP31. It is calculated as:

$$\frac{\rho_{NIR} - \rho_{Red}}{\rho_{NIR} + \rho_{Red}}$$

By design, the NDVI varies between -1 and 1, where:

- dense vegetation exhibits values between 0.9 and 0.6;
- grasslands or senescent crops give values between 0.5 and 0.2
- soils are characterized by small positive values usually between 0.1 and 0.2;
- deep water and clouds yield negative values.

The NDVI is widely used to qualitatively detect the presence of vegetation and monitor qualitatively its growth without requiring any further in-situ data.

#### Temporal feature

In the first phase, for a given pixel of the demonstration site, the maximum value of the NDVI was determined for a selected month, for all the considered years, from 2013 to 2017. When clouds were too present, a fusion of several months has been applied: the winter maximal NDVI has been computed using images from November, December, January and February – and the resulting image has been labeled as ‘months of winter’.

The maximum value of NDVI are then stacked into a multiband image used for the classification.

#### K-means

The K-mean clustering algorithm is a classifier which assumes that features associated with each class are distributed according to a Gaussian distribution. However, this can lead to spurious results if the data is

not normally distributed. This method is a pixel-based unsupervised and iterative classification algorithm based on spectral information and similarity. The algorithm performs two steps iteratively in order to reduce the variability within each cluster:

- Reassign data points to the cluster whose centroid is closest;
- Calculate the new centroid for each cluster.

The classes identified by the K-means classification, based solely on the spectral signature of their pixels, can then be associated with a type of LU to produce the map. For the K-means to deliver those classes, a given amount of them has to be given as a parameter.

For the second phase, in order to remove the gaps in data left by clouds, the (WAC) methodology described in the deliverable of WP33 [AD05], was used to produce two dates every month. The NDVI of those dates were then stacked for the whole year and fed to the K-Means algorithm, which this time uses spectral separability in order to classify the various LC present in the landscape.

As explained in this report [AD05], “this method averages all cloud-free reflectance values acquired during the compositing period giving more weight to the images closer to the middle of the compositing period in order to enhance the fidelity to the central date (Hagolle & Morin, 2015)”.

In order to remove most of the manual labelling that took place in the first phase, the TIMESAT software package has been used for analysing time-series of satellite sensor data. TIMESAT is able to investigate the seasonality of satellite time-series data and their relationship with dynamic properties of vegetation, such as phenology and temporal development (Jonsson & Eklundh, 2002). The temporal domain holds important information about short- and long-term vegetation changes.

However, the parameters produced by TIMESAT are far more complete than the parameters provided in the first phase by the manual extraction and the envisioned validation by computer assisted photo-interpretation (CAPI) was not accurate enough. The idea was to look at each point randomly drawn over a stratified grid in the raw S-2 time series and note the exact date for emergence, vegetation peak and end of season.

There remains the need of an ancillary datasets at pan-European scale that could provide information on the vegetation state. The recent invitation to tender (ITT) related to phenology (EEA, 2019) will potentially be the first milestone to create map of vegetation indices such as NDVI, FAPAR and LAI, complemented by the seasonal trajectories and their key parameters, such as presented in this prototype.

It should be noted that this map of phenological activities has been converted to a vector layer and used in the second phase as a segmentation for the New land Cover (NLC) products, as described in the deliverable of WP45 [AD06]. Due to the reproducibility of such methodology, it has been selected over more traditional way to segment satellite images, as benchmarked in deliverable of WP33 [AD05], solving one of the issue raised in the matching ITT for Corine Land Cover+ (CLC+).

## 4.2 Method for crop growth condition

The growing condition of any crop can be assessed by the trajectory of the Leaf Area Index (LAI) when the LAI can be observed on a regular basis. Unlike the NDVI, the LAI is a biophysical variable which can be retrieved by various sensors. The LAI is here not only defined by the half of the leaves area as commonly accepted but rather by the Green Area Index (GAI). The GAI is indeed a more appropriate term when working with cereals because the main aerial organs (leaves, ears and stems) are photosynthetically active (Hoefsloot et al., 2012; Duveiller et al., 2011b). For the sake of clarity, the LAI acronym will however be used while this means GAI. The LAI retrieval is based on the BVnet algorithm using artificial neuronal network trained on simulated LAI and reflectance values. The reflectance values are simulated using the ProSail radiative transfer model for the Sentinel-2 bands at 10 m and 20 m-

resolution except the blue band (B2) and the B8 due to its overlap with B7 and B8a. Delloye et al. (2018) validated the LAI retrieval performance from Sentinel-2 bands in the demo site West for the wheat.

The retrieved LAI values are averaged over the entire field minus an inner buffer of 2 pixels from the field boundaries to avoid any pixel effect.

Based on the crop type provided by the Land Parcel Identification System or from the crop map obtained as in the WP4.4, the LAI values of all the fields of the same crop located within a radius of 3 km far from the field border are averaged along the season. That is mainly to compare the crop growth condition for any given field of interest. The average does not include the field of interest and is not available when no field of the crop of interest are grown within the 3 km radius. The 3 km radius was found relevant because of the similarity of external factors, typically the meteorological conditions and the agro-climatic zone. The average LAI profile of the crop of interest and the LAI profile of the field of interest can then be visually compared in terms of crop development (earliness, maximum, maturity, etc.). Both profiles are also quantitatively assessed through a simple metric corresponding to area under the curve for three different crops.

## **4.3 Method for multiannual trends and potential changes based on SAR data from S-1**

In this section, an approach to describe multiannual trends and potential changes for the specific HRL layers forest and grassland is explained into detail. The approach relies on the idea that based on a series of multi-temporal images for a given study area, the remotely sensed temporal dynamics of a specific HRL class are sensibly different to those of all other classes. For instance, in the case of radar data the backscattering temporal mean of urban areas (due to double bounce reflection) is higher than that of forest areas (which might result in high backscattering in one/few acquisitions due to specific conditions, but in general exhibit lower values). Further general assumptions of this approach are that (1) a specific class of the HRLs might change from one year to another and (2) that the classes within the HRL are homogenous at the local to regional scale of the test sites despite having different characteristics at the pan-European scale. Considering these assumptions, the following method is based on calculating statistical distributions for different seasonal and annual metrics derived from Sentinel-1 time series data (see section 4.3.1) for each class of the HRL Forest (two classes: broadleaved and coniferous) and HRL Grassland (one class: grassland (GRA)) within the demo site. In the next step, potential changes within the HRL are detected at pixel-level, based on these seasonal and annual metrics. Here, a statistical test is applied describing if a specific pixel belongs to the considered class at a certain significance level. Pixels identified as not belonging to the class are labelled as candidates for a HRL update. Therefore, pixels within a certain HRL are assumed to have similar backscatter values over time and space. This might become more critical when the considered spatial extent covers larger areas and different biogeographical zones.

The approach comprises two steps, which are described into detail by the followings.

### **4.3.1 Pre-processing on the input data**

This section describes the pre-processing and preparation of the input data.

#### **Creating the master HRL**

Primarily, the HRLs require pre-processing and harmonization with respect to a) their original spatial resolution of 20m to the resolution of the Sentinel data (i.e., 10m) and b) their spatial coverage (adaptation to the Sentinel-2 tile system). Figure 4-1 shows the harmonized HRL Grassland of 2015 for the Belgium test site. The harmonized HRL Grassland describes the situation at time  $t_0$  (in this case 2015).

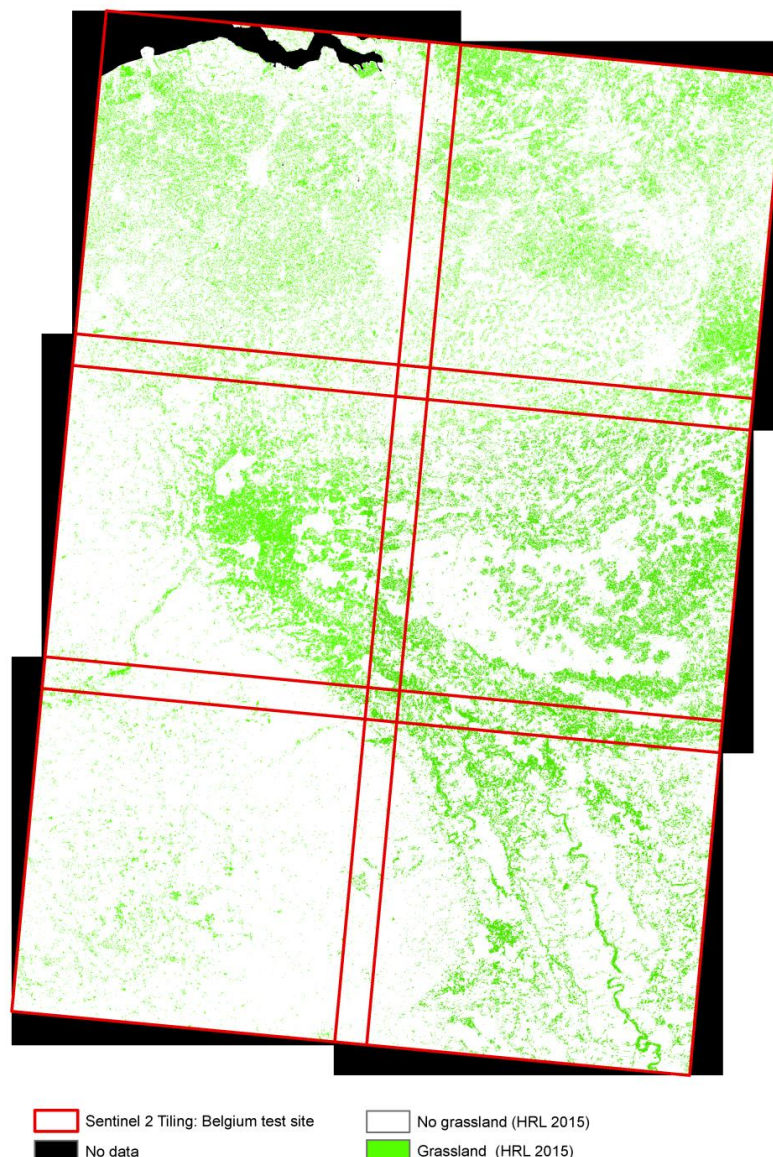


**Figure 4-1: Sentinel-2 tiles for Belgium test site and harmonized grassland HRL of 2015**

## S-1 preprocessing and feature extraction

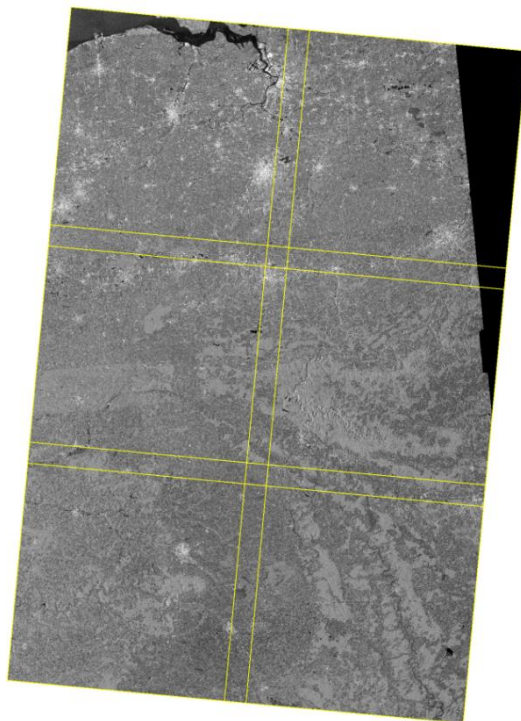
S1 IW GRDH data acquired both in ascending and descending pass in 2015, 2016 as well as 2017 and intersecting the given AOI are first downloaded. Each of them is then pre-processed by means of the S1TBX/SNAP software. Specifically, this task includes:

- orbit correction (using restituted orbits);
- thermal noise removal (for removing dark strips near scene edges with invalid data);
- radiometric calibration (for computing backscattering intensity using sensor calibration parameters in the GRD metadata);
- Range-Doppler terrain correction (SRTM 30m DEM is used where available, for latitudes lower than -60° and greater than +60° the ASTER DEM is employed);
- Conversion to dB values.

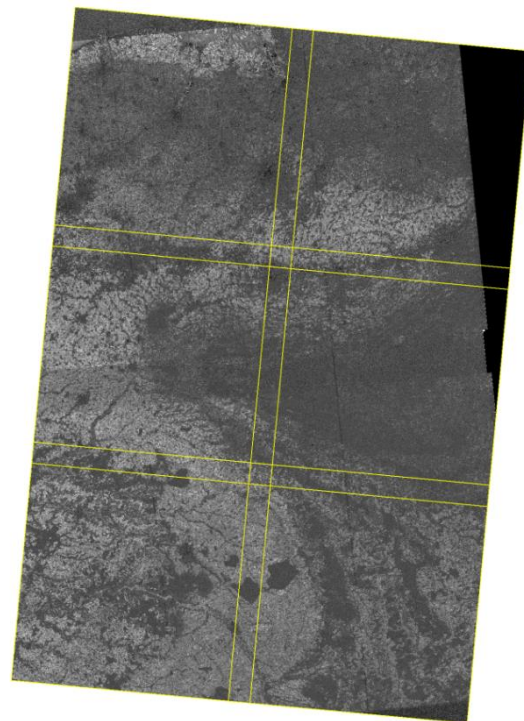
Accordingly, after pre-processing all the available data of 2015, 2016 and 2017 for the given region, for each pixel nine key temporal statistics have been extracted for the seasons a) March, April, May (MAM), b) June, July, August (JJA), c) September, October, November (SON) as well as separately for the complete years 2015, 2016, and 2017, namely:

- backscattering temporal maximum;
- backscattering temporal minimum;
- backscattering temporal mean;
- backscattering temporal median;
- backscattering temporal standard deviation;
- backscattering temporal 5% percentile;
- backscattering temporal 10% percentile;
- backscattering temporal 90% percentile;
- backscattering temporal 95% percentile.

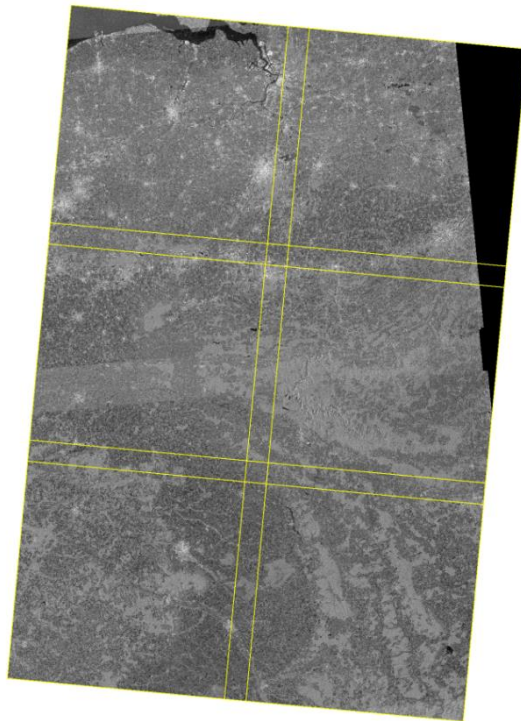
Furthermore, scenes acquired with ascending and descending pass have to be processed separately due to the strong influence of the viewing angle in the backscattering e.g., of urban areas. Each of the relative orbits 161 in ascending and 37 in descending pass cover almost the whole demo site and have been therefore selected for this analysis. Figure 4-2 shows examples of the backscattering temporal statistics of 2015 over the Belgium demo site.



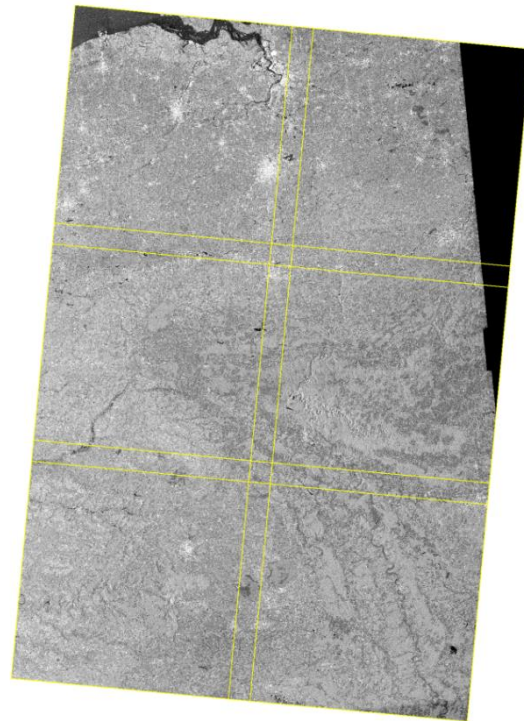
(a) backscattering temporal mean



(b) backscattering temporal standard deviation



(c) backscattering temporal minimum



(d) backscattering temporal maximum

**Figure 4-2: Examples of temporal S-1 metrics: Backscattering temporal statistics of 2015 of the S-1 relative orbit 161 in ascending pass over the BELGIUM demo site: (a) backscattering temporal mean, (b) backscattering temporal standard deviation, (c) backscattering temporal minimum, (d) backscattering temporal maximum (outlines of S-2 granules in yellow)**

Reducing time series data to seasonal and annual metrics has the advantage of enabling a fast and effective processing without noise influence. The preference of using metrics instead of single observations for land classifications is widely applied because of its ability of characterizing certain land cover classes with such features (Esch et al., 2018; Gessner et al., 2015; Huettich et al., 2009; Klein et al., 2012; Wohlfart et al., 2016).

### **4.3.2 Statistical analysis of seasonal and annual metrics within the HRL classes to identify potential change**

In this section, the statistical approach behind the update of the HRL based on seasonal and annual metrics is presented.

The concept of the approach relies on the basic assumption that all pixels of the considered class of the HRL layer have similar characteristics in the feature space (described in section 4.3.1) which considerably differ from all other classes. Differences between the feature values of a pixel and their distribution for a certain class can be used as an indicator for change. Therefore, three steps have been implemented to identify pixels which might need an update.

1. Firstly, the statistical mean and standard deviation of all available S-1 backscatter metrics are being calculated for each HRL within the demo site to derive the general behaviour of that specific land cover class. These statistics are the basis for further comparison and decision if a pixel has to be added or removed from the HRL.

2. Based on these statistics, the distance in the feature space between each pixel and the characteristic class mean is being obtained. For the calculated distances three categories have been defined:

- a. The 1<sup>st</sup> category suggests that the corresponding pixel does not differ from the class mean and thus is considered as stable with no change:

$$Distance_{stable} : \text{for pixel } < Class_{mean} \pm Class_{stddev}$$

- b. The 2<sup>nd</sup> category implicates that the pixel is placed between  $\pm$  two standard deviations:

$$Distance_{1stddev} : \text{for pixel } < Class_{mean} \pm 2 * Class_{stddev} \text{ AND } > Class_{mean} \pm Class_{stddev}$$

- c. The 3<sup>rd</sup> category implicates that the pixel is out of the range of  $\pm$  two standard deviations

$$Distance_{2stddev} : \text{for pixel } > Class_{mean} \pm 2 * Class_{stddev}$$

These distance indicators have been derived for each of the S-1 backscatter metrics and for the discrete HRL Forest and HRL Grassland.

3. In a third step, the results for each feature have been combined to enable a rather valid and stable output which is not based only on few outliers. Therefore, the approach considers the differences throughout all features of one year and calculates the frequency of one pixel belonging to one of the three categories defined in the second step. Again, this additional step is required as otherwise disturbances or irregularities within one metric would lead to misinterpretation. By using all metrics and making a decision based on the cumulative analysis of each pixel's statistical distances rather stable results are expected. In the third step two empirically tested thresholds are applied at pixel level:

$Th_1$ : less than 50% of considered metrics belong to category  $Distance_{stable}$

$Th_2$  : more than 33% of considered metrics belong to category  $Distance_{2stddev}$

By applying these two thresholds, all pixels featuring a higher distance to the statistical mean of one particular HRL class are labelled as a potential pixel for update either in category two or category three. Further, statistical tests can be applied to determine the significance level that a pixel does not belong to a certain class. The entire workflow is presented in Figure 4-3.

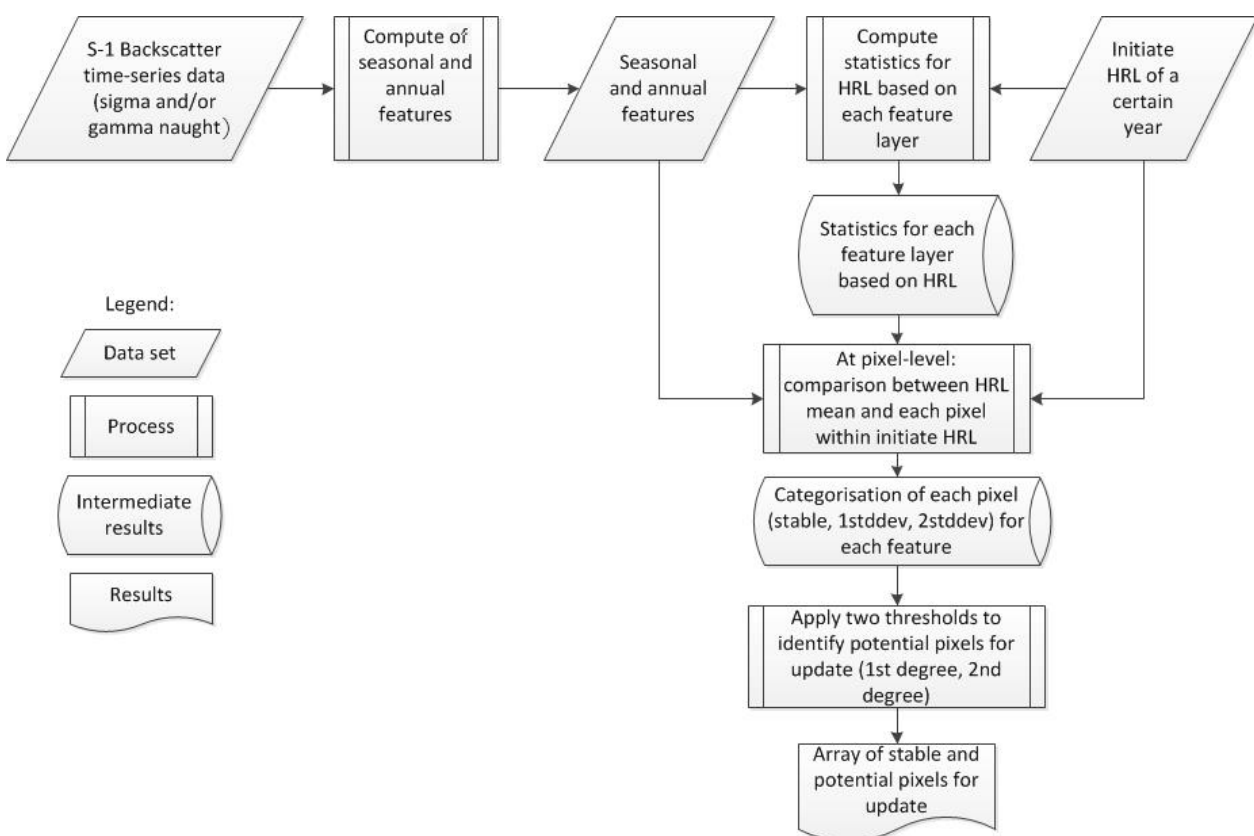


Figure 4-3: Workflow for identification of potential pixels for update within a certain HRL

#### 4.4 Methods for emergence date detection

The crop emergence date is a prototype which requires method developments which are specifically targeted to this phenological parameter. Therefore several methods were described and benchmarked as documented in the report of the WP34. The challenge of the emergence date detection in an agriculture context is to deliver the information as early as possible in the season. Unlike most methods for phenological parameters retrieval, this means that the phenological analysis take place much before the completion of the full growing cycle. This requirement discards many methods designed to work on complete profile.

The estimation of the emergence date is based on the detection of the first phenological stages (crop emergence, first leaf development) from satellite remote sensing (i.e. Sentinel-2) time-series. The aim is to provide early-season information, to allow an easy operational implementation and further generalization of the method. The detection is performed at the field level on early-season satellite

images which presents a clear advantage against detection methods requiring full season images to provide initial results.

#### 4.4.1 Emergence date as phenological parameter

The estimation of the emergence date is based on the detection of the first phenological stages (crop emergence, first leaf development) from satellite remote sensing (i.e. Sentinel-2) time-series. The aim is to provide early-season information, to allow an easy operational implementation and further generalization of the method. The detection is performed at the field level on early-season satellite images which presents a clear advantage against detection methods requiring full season images to provide initial results.

The phenological stages are commonly defined according various classification systems such as the Biologische Bundesanstalt und Bundesortenamt und Chemische Industrie (BBCH) scale. The standard stages are selected to provide a continuous scale ranging from 0 to 100 (De Bernardis et al., 2016) which is relevant to any crop and location.

In particular, a specific BBCH stage is reached when at least 50% of the plants are within the definition of that stage (Lopez-Sanchez et al., 2012). The onset date of the stages presents an important inter-annual variation. It can be explained by environmental and climatic factors as well as farm-level management decisions (crop variety, crop rotation, input availability, etc.) (Sakamoto et al., 2010). Generally, temperature and water are the main climatic factors impacting the development of the majority of species. A large number of species is also impacted by the length of the photoperiod. In temperate climates, light is generally the primary limiting growth factor. In humid climates, light and nutrients are both limiting. In tropical or dry subtropical climates, water is the main constraint but the absorption of nutrient is also reduced.

#### 4.4.2 VIs and hue time series as candidate data sources

Vegetation Indices (VIs) can be seen as a proxy of the Fraction of Absorbed Photosynthetically Active Radiation (FAPAR) as they relate "greenness" with the measure of the absorption characteristics of the vegetation in the red and NIR spectral bands (Pinty et al., 2009). NDVI first relates to total green biomass and is sensitive to low to moderate LAI values but saturates at high values (Nguy-Robertson et al., 2014). VIs do not present a straightforward biophysical interpretation, although they are strongly correlated with biophysical variables (White et al., 1997; Eklundh et al., 2003; Pinty et al., 2009). LAI retrieval algorithm can also be considered but the underlying assumption and the higher computing cost of such an algorithm prevent considering it at this stage.

Studies showed that the NDVI gives good estimates of the vegetation dynamics when the vegetation is photosynthetically active (Palacios-Orueta et al., 2012). Other VIs based on the Short-Wavelength Infrared (SWIR) are better for assessing low vegetation density zones. In semi-arid areas, the information contained in both the Mid-Infrared (MIR) and blue regions relates to soil properties which helps in distinguishing vegetation type classes (Hüttich et al., 2009).

Pekel et al. (2011) studied the detection of green vegetation in semi-dry and dry areas. The image color is transformed from a Red-Green-Blue (RGB) to a Hue-Saturation-Value (HSV) representation. As the MIR and NIR regions present several advantages for soil discrimination, the three MIR-NIR-Red bands are used instead of RGB. The Hue component is the only parameter conserved because it is able to discriminate land cover type where Saturation and Value fail. Marinho et al. (2014) applied the method developed by Pekel et al. (2011) and tested it for sowing date estimation which had not been investigated yet. The study aimed at estimating green-up onset dates in arid and semi-arid regions (i.e. the Sahel region) from MODIS 250 m resolution images and RFE 8 km resolution rainfall estimate and, then, comparing it with ground-truth data.

To reduce the noise and fill the gap in the time series, two interpolation methods are tested. First, a simple linear interpolation method is applied between all the successive observations, between October and the end of April. Alternatively, a logistic interpolation method commonly used to reduce noise in the vegetation profiles is also selected to interpolate the satellite observations during plant growth (i.e., between minimum and maximum index values): a four-parameter logistic function.

#### 4.4.3 Candidate detection methods

The candidate methods for phenology studies are often grouped into four main categories: threshold, moving window, function fitting and model fitting methods (Zeng et al., 2016; de Beurs and Henebry, 2010).

(1) The threshold method (Figure 4-4a) is based on linking a phenological event with the crossing of a certain value of the VI curve. The threshold can either be fixed or dynamic and varies with land cover, soil background, view and solar angle (Reed et al., 1994). However, they do not rely on an underlying biophysical meaning. For example, White et al. (1997) identified the onset and end of greenness when the NDVI ratio of the smoothed curve exceeds or falls below 0.5 respectively. Lobell et al. (2013) defined the green up phase as the date when the double-logistic fitted function exceeds 10% of the year's maximum amplitude. The main drawback of the fixed threshold is the disability for reflecting the spatial changes of larger study area and inconsistency for a wide variety of land covers (de Beurs and Henebry, 2010; Reed et al., 1994). Plethora of thresholds have been used based on the long-term VIs mean, yearly VIs, NDVI ratios, Normalized Difference Water Index (NDWI), etc. The ratio approach has the advantage of being independent from the geographic location and land cover of the area. As such, the NDWI is particularly indicated for heavily snowed areas.

(2) The moving window method can be derivative or backward-looking moving average. The derivative method (Figure 4-4b) is founded on the assumption that the fastest green-up or greatest leaf expansion corresponds to the most ecologically relevant SOS (White et al., 1997). In other words, the maximal increase and decrease of NDVI tally with SOS and EOS (de Beurs and Henebry, 2010). Moving windows of a certain temporal extension are applied on each pixel and the slope (or derivative) is calculated. The highest positive and lowest negative derivatives are then easily extracted.

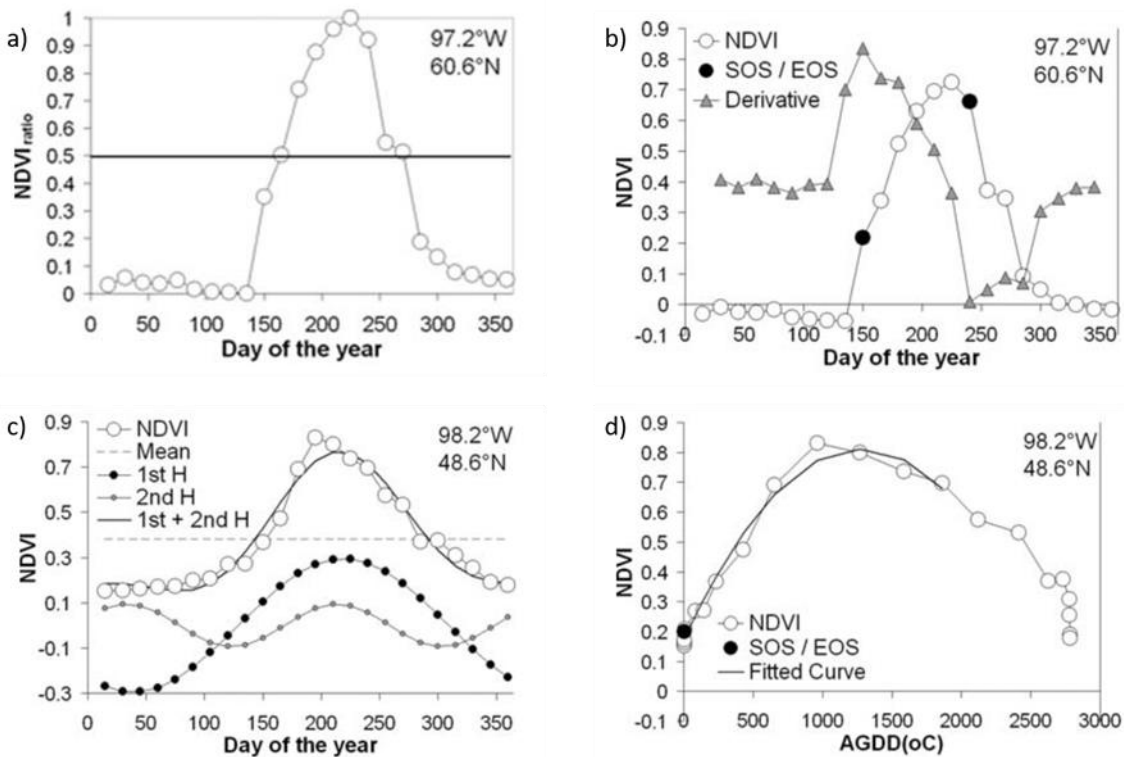


**Figure 4-4: Four methods based on the NDVI to detect start and end of the season. a) fixed threshold, b) derivative, c) Fourier transform, d) quadratic fitting based on AGDD (de Beurs and Henebry, 2010)**

Some methods retrieve the second derivative and determine the SOS as the time point combining a positive slope and a local maximum (Balzter et al., 2007). Cong et al. (2013) defined green-up onset date as the highest positive relative change of the average NDVI time-serie for a 15-day moving window. Moulin et al. (1997) identified the beginning of the vegetation cycle (*b\_date*) on three conditions: (i) NDVI value at *b\_date* is close to a bare soil value, (ii) left derivative (before *b\_date*) should be equal to zero because NDVI is assumed constant before the growth season, (iii) right derivative (after *b\_date*) should be positive on two weeks' time window. de Beurs and Henebry (2010) reported that this method gives good results where the NDVI curve displays a sharp increase and a steep decrease.

The backward-looking moving average method identifies the onset of greenness as the date when the VI curve crosses the moving average function which represents a significant change in the growth trend. The moving average is built as the average of the last *i* observations. The choice of the temporal window (i.e. number of *i* observations) is crucial and arbitrary as it introduces a time lag: a large time interval is less sensitive whereas a small interval may take insignificant variations into account (Reed et al., 1994; de Beurs and Henebry, 2010).

These two first methods present the advantage of being able to retrieve multiple growing seasons (Verhegghen, 2013). However, they are not good at distinguishing the basic temporal variations of the vegetation reflectance (noise) from the relevant seasonal changes. That, the date retrievals based on local minima, maxima, or fixed thresholds can be completely shifted if observation errors contaminate the original dataset. For instance, atmospheric constituents, bi-directional reflectance distribution function, cloud coverage, and the mixed-pixel effect often influence MODIS images (Sakamoto et al., 2010).

(3) The function fitting method (Figure 4-4c) applies a mathematical function to a given VI curve to smooth or filter the data and extract the main information. Different functions have proved to be useful: Fourier analysis, wavelet transformation, Principal Component Analysis (PCA), Canopy Structure Dynamic Model (CSDM), etc. The Fourier analysis which decomposes a complicated curve into a sum of sinusoidal

waves, is able to approximate a VI (de Beurs and Henebry, 2010). This segmentation is sensitive to systematic changes and reduces the non-systematic data noise. To interpret the new curve, the first Fourier harmonic is considered to represent the mean NDVI. The wavelet transform also decomposes the VI time-series into a set of small local waves (named wavelets) assuming the fact that the noise components have higher frequencies than the main seasonal changes (Sakamoto et al., 2010). An important aspect is that this type of frequency decomposition performs better on long time-series showing periodic changes. Consequently, the source observations should be measured at a regular time interval or require gap filling to be adequately processed (de Beurs and Henebry, 2010).

To retrieve phenological events from a fitted curve, the procedure of Sakamoto et al. (2005) can be used: the minimal or inflection point earlier than 60 days before the maximum value (defined as heading date) is selected, then, the later of the two points is identified as planting date. However, the Root Mean Square Error (RMSE) of 12.1 days for planting date estimate is not satisfactory. Another way to account for key information lies on the PCA. Through a linear combination of the original observations, the primary factors explaining the main variance of the dataset are kept. Again, the interpretation of the resulted parameters (eigenvectors) is not self-evident and does not remain consistent over the years limiting the comparative power of the method (de Beurs and Henebry, 2010). The advantage of those fitting methods is to reduce noise and adjacency pixel problem (between pixel effects) and their ability to derive phenological metrics in a consistent way (Palacios-Orueta et al., 2012).

The model fitting method fits a model to the remote sensed observations. These models can be simple (logistic models, etc.) or more complex (Gaussian Local Functions, etc.) and are previously defined or dynamically built with input data (de Beurs and Henebry, 2010; Zeng et al., 2016). The number of input parameters compared to the amount of observations available for their identification and the need of large-scale ground-truth data is crucial when assessing the scope and implementation of these model fitting (Duchemin et al., 2008).

Accumulated Growing Degree Days (AGDD) can be interpreted as a measure of the accumulated heat above a specified base temperature from the beginning of the season: maize base temperature is estimated around 10° C. Modelling vegetation growth under AGDD instead of anthropocentric calendar time (Figure 4-4d) is more relevant especially during the first half of the growing season when day length and water stress are not the main contributors yet (de Beurs and Henebry, 2010).

These four methods can be combined. Threshold methods are generally applied on smoothed function to reduce data noise (Che et al., 2014).

Then, a logistic function was applied to each identified increasing or decreasing period and key phenological dates were then retrieved from the fitted curve. For a single growth cycle, the following logistic function modelled the curve:

$$y(t) = \frac{c}{1 + e^{a+bt}} + d$$

Where  $t$  is time in days,  $y(t)$  is the VI value at time  $t$ ,  $a$  and  $b$  are fitting parameters,  $c + d$  is the maximum VI value, and  $d$  is the initial background VI value.

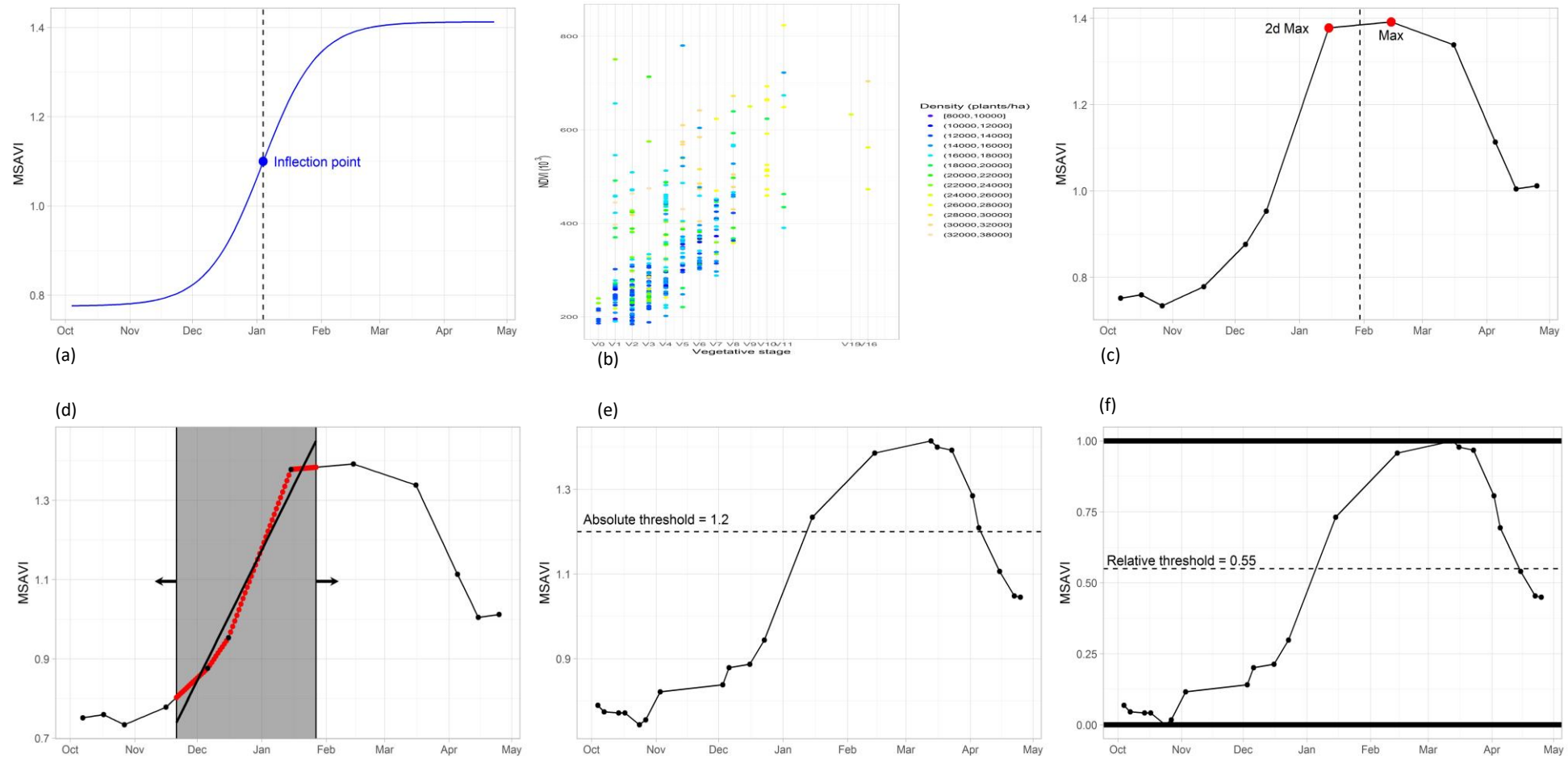


**Figure 4-5: Overview of the six emergence estimation methods. Methods without parameterization: (a) inflection point, (b) base logistic (c) maximum value. Methods with parameterization: (d) highest slope, (e) absolute threshold, (f) relative threshold. The threshold methods are both tested on the linear and logistic interpolated observations. Presented vegetation profiles are examples from the maize calibration sample**

#### 4.4.4 Performance indicators

Furthermore, the comparison of the results of a systematic combination of detection methods and vegetation proxies was necessary for detecting the best combination. The systematic analysis of three approaches (i.e. threshold, derivative method and model fitting) and three vegetation proxies (NDVI, soil-adjusted MSAVI and Hue index (MIR-NIR-Red)) interpolated using two functions (linear, logistic), and the assessment of their relative performances against ground-truth measurements are achieved.

It is important to notice that each tested method aim to detect different time metrics (threshold intersection, highest slope, inflection point, maximum value and base logistic value) to estimate emergence date. Obviously the emergence date is then estimated by using a correction coefficient. The correction coefficient is named the time-lag which corresponds to the interval between the emergence date and the temporal metric specific for each method. Hence, the estimated emergence date from each profile corresponds to the temporal metric date minus the mean time-lag for this method. Subsequently time-lag stability (between the profiles) is the criteria to assess the performance between methods and VIs profiles.

Given that stable time-lag reducing the spread around its value is targeted, two statistical indicators are used to discriminate the different methods and VIs: Standard deviation (SD) and median absolute deviation from the median (MAD). In particular, SD is used for measuring the dispersion of the emergence date estimations around the mean time-lag but it is very sensitive to outliers. Therefore, MAD is incorporated as addressed by Varmuza and Filzmoser (2016).

$$MAD = b \times \text{median}(|(x_i - \text{median}(x_n))|)$$

with,  $x_n$ , the  $n$  original observations and  $b$ , a multiplicative parameter of 1.4826, assuming the normality of the data and disregarding the abnormality induced by outliers.

Although, utilizing both SD and MAD avoid the outliers affect and treat the data as it has Gaussian distribution, significant difference are shown by the two indicators (Leys et al., 2013).

## 5 Prototype Implementation

This chapter shows the prototypical implementation of the phenological products. Firstly, the integrated EO and ancillary data is described (section 5.1), followed by explaining the pre-processing steps, the demonstration of the results of the actual prototype in the demonstration site (section 5.2), and lastly, the description of the dataset properties and its metadata, referring to *P41.2a - Data Sets of Time Series Derived Indicators and Variables Products* (section 5.3).

### 5.1 Input Data, pre-processing and Data Integration

This section will focus on the used input data, their pre-processing, and the integration. Firstly, the focus is laid on to the prototype based on generic LC metrics (section 5.1.1). Afterwards the data use for the prototype for the estimation of the emergence date will be described (section 5.1.3).

#### 5.1.1 Generic LC metrics

In the first phase, the objective of this prototype was to estimate phenological parameters based on the maximal NDVI per month. The year 2017 dataset of S-2 is very cloudy, while the year 2016 did not fully integrate both satellite of the S-2 constellation, and too few images over the demonstration site could be used to fully derive an image of the maximum NDVI value per month. It has then been decided to use the Landsat archive instead, to simulate the normal temporal rate of incoming S-2 data, at an observation every 5 to 6 days, on a less cloudy year.

The archive of Landsat-8 data, at a 30m resolution, have been downloaded, dated from 2013 to 2017 over the demonstration, if clouds were covering less than 30% of the considered scene. In total, around 50 images per year were retrieved – while the demonstration site was covered by more than a dozen of Landsat-8 footprints. The number of Landsat-8 images per month were then close to the temporal resolution offered by the two S-2 satellites, at approximately 5 images per month. The dataset has been selected among the products of the L1T Collection (L1TP), which are radiometrically calibrated and orthorectified using ground control points and DEM datasets to correct relief deformations. Only products of the Tier 1, which guarantees that geometric and radiometric quality criteria have been met, have been considered in this study, since those constitute the highest quality products available for pixel-level time series analysis that can be downloaded in a semi-automatic manner. The Landsat-8 Operational Land Imager (OLI) offers 11 optical bands, that are detailed in

Table 5-1. Only the fourth and fifth band are required for the computation of the NDVI.

**Table 5-1: List of the optical and thermal bands of Landsat-8**

Landsat- 8 OLI bands		
Bands	Wavelength in $\mu\text{m}$	Resolution in m
<b>Band 1 – ultra blue</b>	0.435 - 0.451	30
<b>Band 2 - Blue</b>	0.452 - 0.512	30
<b>Band 3 - Green</b>	0.533 - 0.590	30
<b>Band 4 - Red</b>	0.636 - 0.673	30
<b>Band 5 - Near Infrared (NIR)</b>	0.851 - 0.879	30
<b>Band 6 - Shortwave Infrared (SWIR) 1</b>	1.566 - 1.651	30
<b>Band 7 - Shortwave Infrared (SWIR) 2</b>	2.107 - 2.294	30
<b>Band 8 - Panchromatic</b>	0.503 - 0.676	15
<b>Band 9 - Cirrus</b>	1.363 - 1.384	30
<b>Band 10 - Thermal Infrared (TIRS) 1</b>	10.60 - 11.19	100 * (30)
<b>Band 11 - Thermal Infrared (TIRS) 2</b>	11.50 - 12.51	100 * (30)

The QA (quality assessment) file, which is created using the fmask algorithm, has been read for each image, and provides the opaque cloud presence confidence, as well as the cloud confidence for cloud shadow, and cirrus, snow and ice presence.

The given digital counts of each band have been converted into top of Atmosphere (TOA) reflectances using the calibration file and no further pre-processing has been applied.

In the second phase, datasets of S-2 images kindly provided by the Johanneum Research has not been deemed unusable for the reworked methodology regarding input data. Indeed, data provided over the test sites (based on S-2 L2A re-processed using Sen2Cor but improved by the use of cloud detection algorithm specifically designed by the Johanneum Research) were of better quality than the data provided over the rest of the demonstration site, which were raw S-2 L2A re-processed using Sen2Cor. This is a simple consequence of the use of CREODIAS by the Johanneum Research. Particular pre-processing of datasets over the DIAS can be extremely resource- and time-consuming.

The discrepancy between those two datasets however, was resulting into blatant delineation of the geometry of the test site tiles, and leading the K-Means algorithm to classify the same LC over the test site and the rest of the demonstration site into different classes of phenological activities. The WAC methodology was not sufficiently robust to adjust the difference in cloud mask quality.

Since the phenological layers was also produced over the South-West for the NLC products, based on uniformed MAJA datasets for the S-2 interpolation, it has been decided to provide this prototype in lieu of the West prototype. The same was done over the Central demonstration site.

### **5.1.2 Crop growth condition anomaly**

The Sentinel-2 full archive have been processed for the three tiles of the demo-site West. Based on the benchmarking documented in the report of WP32. The LPIS for the 2018 season have been made available for Flanders and for Wallonia. Therefore a radius of 3 km around each parcel of maize was computed to identify what will be the local average of all maize fields.

### **5.1.3 Emergence date detection**

The objective of this prototype is to estimate emergence date based on the detection of the first phenological stages of maize (crop emergence, first leaf development) from satellite remote sensing (i.e. Sentinel-2) time-series for 2016-2017 and then for 2015-2016 in the Free State province, South Africa.

#### **5.1.3.1 EO data and pre-processing**

The Sentinel-2 time series for the 2016-2017 crop season spans from the start of the growing season (1<sup>st</sup> of October) until end of April. Unfortunately only Sentinel-2a images was available for this demonstration because of the late launch of Sentinel-2b. In addition two images on the 13<sup>th</sup> and 26<sup>th</sup> of November were discarded because aberrant values probably due to undetected cloud cirrus or cirrostratus (Figure 5-1).

The Sentinel-2 data were pre-processed to bottom of atmosphere reflectance according to the standards of the WP32. However, because of the poor quality of the cloud screening embedded in the Sen2Cor algorithm, the MACCS algorithm was selected as implemented in the open-source Sen2-Agri operational system. The NDVI product was computed at 10 m resolution using the Sentinel-2 red (B4) and vegetation NIR (B8a) bands. Clouds, cloud shadows, water, snow, and other zones were masked.

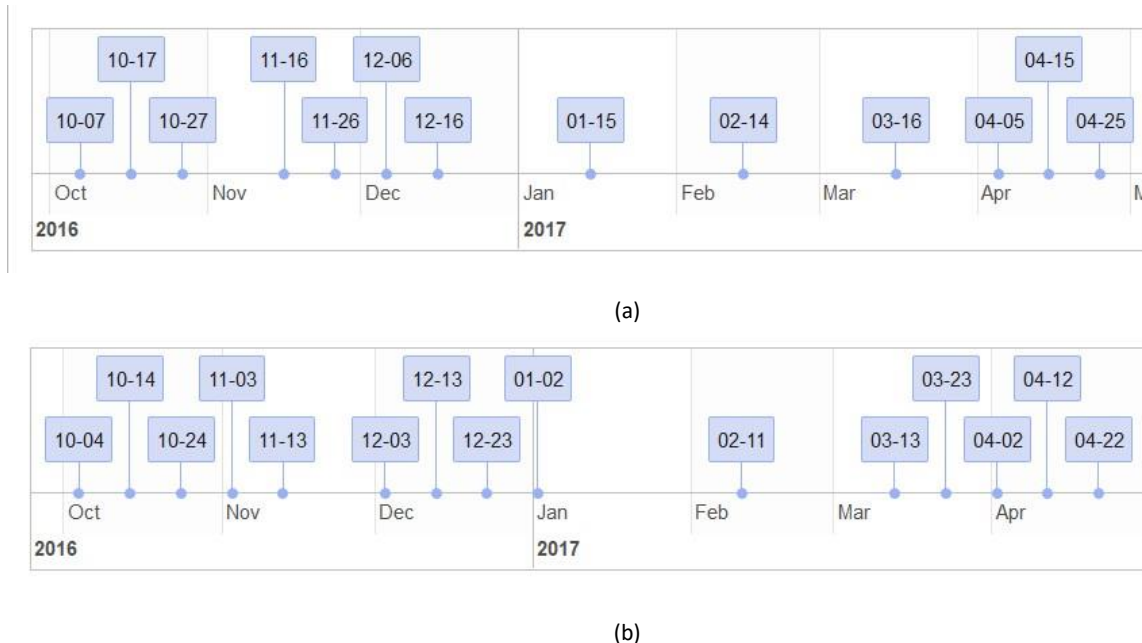


**Figure 5-1: Available satellite images (not fully clouded): (a) 35JMK and 35JNK (left) tiles; (b) 35JNK (right) and 35JPK**

### 5.1.3.2 Ancillary datasets

Thanks to a long-term partnership between the UCL and the Institute for Soil, Climate and Water of the Agricultural Research Council in Pretoria, several very valuable datasets were made available to UCL in the framework of the Memorandum of Understanding. Indeed this demonstration was carried out in collaboration of the ARC team providing better insight into the agriculture realities of the Free State and understand its dynamics.

The Producer Independent Crop Estimate System (PICES) was provided by ARC to UCL in the framework of this close collaboration. This system has been developed by ARC and its partners; SiQ and GeoTerralimage; since 2005 to improve grain crop area estimates combining digitization of the field boundaries from satellite imagery and point frame sampling. It was also created in light of a raising tendency of the farmers to refuse to give the necessary information for accurate area estimates. Spot 5 satellite imagery at a 2.5-meter resolution was used for digitizing. This dataset is updated on a regular basis, approximately every 3 years. The field boundary layer of the Free State used in this work is still globally up to date (Figure 5-2). Some fields however were divided or merged in the meantime. Another particularity of the fields is that grass strips often separate field parcels without being excluded from the field boundary.



**Figure 5-2: Illustration of the PICES field boundary layer, in the Free State. Background image are the NDVI pixel value on the 15th of January 2017. NDVI values are multiplied by 1000**

Similarly, the temperature data used for the demonstration, i.e. minimal and maximal 10-day mean temperatures at 1 km-resolution, were provided by ARC. The rasters are built by interpolating weather station measurements and then aggregated on a 10-day basis. In particular, 17 stations located in or nearby the demonstration site were used.

### 5.1.3.3 In situ observation of the emergence date

Thanks to the colleagues of the Institute for Soil, Climate and Water of the Agricultural Research Council, an insurance company accepted to share its emergence reports at field level. The company carries out assessment at the field level for its specific multi-risk insurance contracts. In particular, the fields were first evaluated and an emergence reports were drawn up to check for crop type, crop density, agricultural practice, weed management and plant sowing within the appropriate planting window. For these reasons, the visit takes place around the V4 vegetative stage, particularly, to assess weed control by the farmer.

A dataset of 763 point observations for the 2016-2017 agricultural season gives information about crop type and cultivar, client and farm name, insured area, district, density (plants/hectare), row width, report date, phenological stage at the time of observation (using a vegetative and reproductive growth stages scale), estimated emergence date, longitude, latitude and additional comments. Observation was expected to be valid for the whole field. Emergence date was extrapolated from the observed growth stage and the report date based on scientific, field and technical knowledge. The emergence date error was estimated less than 3 to 4 days.

### 5.1.3.4 Calibration and validation datasets

The emergence reports are point observation characterizing a whole field. These observations are attributed to each adjacent field delineated by the PICES field boundaries. To avoid wrong attributions, the assignments are based on the comparison of the insured area with the field area, on the crop type, on the emergence date and considering a coherent observation and reporting strategy. Dubious attributions are discarded. Fields are divided or merged in order to account for yearly field boundaries changes. In order to take into account the within field heterogeneity, a 20-meter inner buffer based on the field boundaries discarded the border pixels and then a second buffer of 120-meter radius centered on the in situ observation point allowed averaging only the pixels close to the field observation. The intersection of these two buffers results in multi-shaped (generally half circular) pixel extraction zones (Figure 5-3).

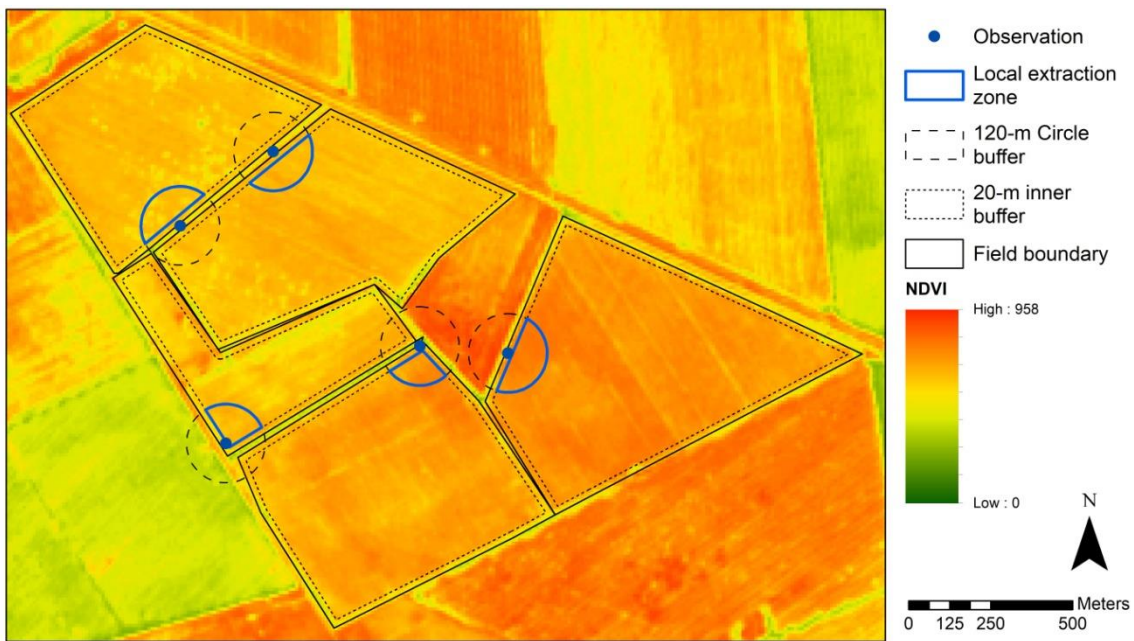


**Figure 5-3: Linking field observation and field delineation by the intersection of a 20-m inner field border buffer with a 120-m circle buffer around each observation. Background image shows the NDVI pixel value on the 15th of January 2017. NDVI values are multiplied by 1000**

From the 763 emergence reports, 497 points correspond to the extracted field and the Sentinel-2 data. These points are 359 and 114 for maize and sunflower fields respectively. For each crop type, the observations are randomly divided into a calibration sample (70%) and a validation sample (30%). Maize samples are distributed as 251 observations for calibration and 108 for validation and Sunflower samples as 80 observations for calibration and 34 for validation. As the cloud coverage combined with a single Sentinel-2 satellite, a third so called monthly sample is compiled to include all the fields having at least one cloud free image per month: 133 fields for maize and 27 for sunflower.

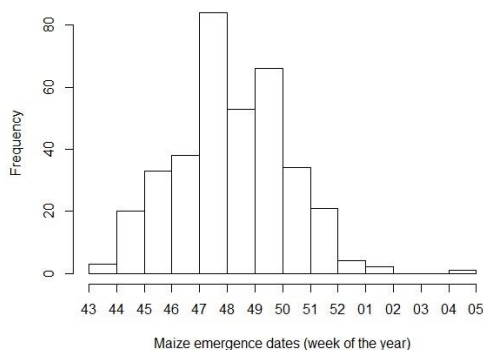


**Figure 5-4: Histogram of emergence dates, aggregated per week of the year for the planting window for maize in 2016-2017**

#### 5.1.4 Multiannual trends and potential changes

The class-specific multiannual backscatter TSI prototypes were derived for the demonstration sites West and Central. For each site the CLMS HRLs of the reference year 2015 of forest dominant leaf type (DLT) and permanent grasslands (GRA) were used as reference classes. For the former the classes deciduous and coniferous were treated separately, as each one has very distinct difference in particular in the

winter season. Since the HRLs are provided at a spatial resolution of 20m, this resolution was also used for the prototype production.

For the TSI derivation, the complete S-1 time series of 2015 to 2019 had to be pre-processed, because within WP32 only the time series of 2017 and 2018 had been processed by the consortium. The input S-1 data were processed from ground range detected processing level to sigma naught by means of the ESA Snap software. The standard pre-processing steps were applied, namely: orbit assembly, precise orbit correction, thermal noise removal, border noise removal, calibration, and range-doppler terrain correction. The ground resolution was set to match the 20m of the HRLs.

Based on these VV and VH backscatter coefficients, the temporal statistics described in Section 4.3. were derived, and summarized for the years 2017 to 2019 in order to obtain a final TSI relative to a given HRL class with three classes: a) no change likely 2) potential change 1<sup>st</sup> degree and c) potential change 2<sup>nd</sup> degree. In order to deal with incomplete acquisitions in the year 2015, the reference characteristics of each HRL class were derived over the time period 2015 to 2016.

Given the nature of the TSI multiannual backscatter trends as a summary of feature space characteristics, no further training data was utilized.

In total four TSI layers were produced per HRL, both for the West demosite and the Central demosite, for the target years 2017, 2018, 2019 as the summary calculated as over the entire time period. Table 5-2 lists all produced prototypes.

**Table 5-2: Calculated TSI prototypes**

<b>TSI Year</b>	<b>Target HRL</b>	<b>Demonstration Site</b>
<b>TSI 2017</b>	Grassland	West
<b>TSI 2018</b>	Grassland	West
<b>TSI 2019</b>	Grassland	West
<b>TSI 2016-2019</b>	Grassland	West
<b>TSI 2017</b>	Grassland	Central
<b>TSI 2018</b>	Grassland	Central
<b>TSI 2019</b>	Grassland	Central
<b>TSI 2016-2019</b>	Grassland	Central
<b>TSI 2017</b>	DLT Coniferous	West
<b>TSI 2018</b>	DLT Coniferous	West
<b>TSI 2019</b>	DLT Coniferous	West
<b>TSI 2016-</b>	<b>Coniferous</b>	<b>West</b>

<b>2019</b>		
<b>TSI</b>	DLT	Central
<b>2017</b>	Coniferous	
<b>TSI</b>	DLT	Central
<b>2018</b>	Coniferous	
<b>TSI</b>	DLT	Central
<b>2019</b>	Coniferous	
<b>TSI</b>	DLT	Central
<b>2016-</b>	Coniferous	
<b>2019</b>		
<b>TSI</b>	DLT	West
<b>2017</b>	Deciduous	
<b>TSI</b>	DLT	West
<b>2018</b>	Deciduous	
<b>TSI</b>	DLT	West
<b>2019</b>	Deciduous	
<b>TSI</b>	DLT	West
<b>2016-</b>	Deciduous	
<b>2019</b>		
<b>TSI</b>	DLT	Central
<b>2017</b>	Deciduous	
<b>TSI</b>	DLT	Central
<b>2018</b>	Deciduous	
<b>TSI</b>	DLT	Central
<b>2019</b>	Deciduous	
<b>TSI</b>	DLT	Central
<b>2016-</b>	Deciduous	
<b>2019</b>		

## 5.2 Results and Validation

This section reports all the main results for the different prototypes and the associated accuracy assessment of the results.

### 5.2.1 Generic LC metrics

As detailed in section 4.1, for the first phase, the maximal value of the NDVI for each month is computed based on different years (2013 to 2017) in order to simulate the temporal rate of S-2 data input.

The resulting multiband images, covering each month from March to October, with an aggregation of wintery months – November, December, January and February – is fed to a slightly modified K-means algorithm. The spectral signature of 30 classes, and their statistics, are computed before a clustering algorithm using the maximum likelihood aggregates pixels based on those statistics and the assumption of a Gaussian distribution, with a convergence threshold of 98%. The resulting layer, called MPA, for Maximal Phenological Activity, can be seen in Figure 5-5, around the region of Antwerp.

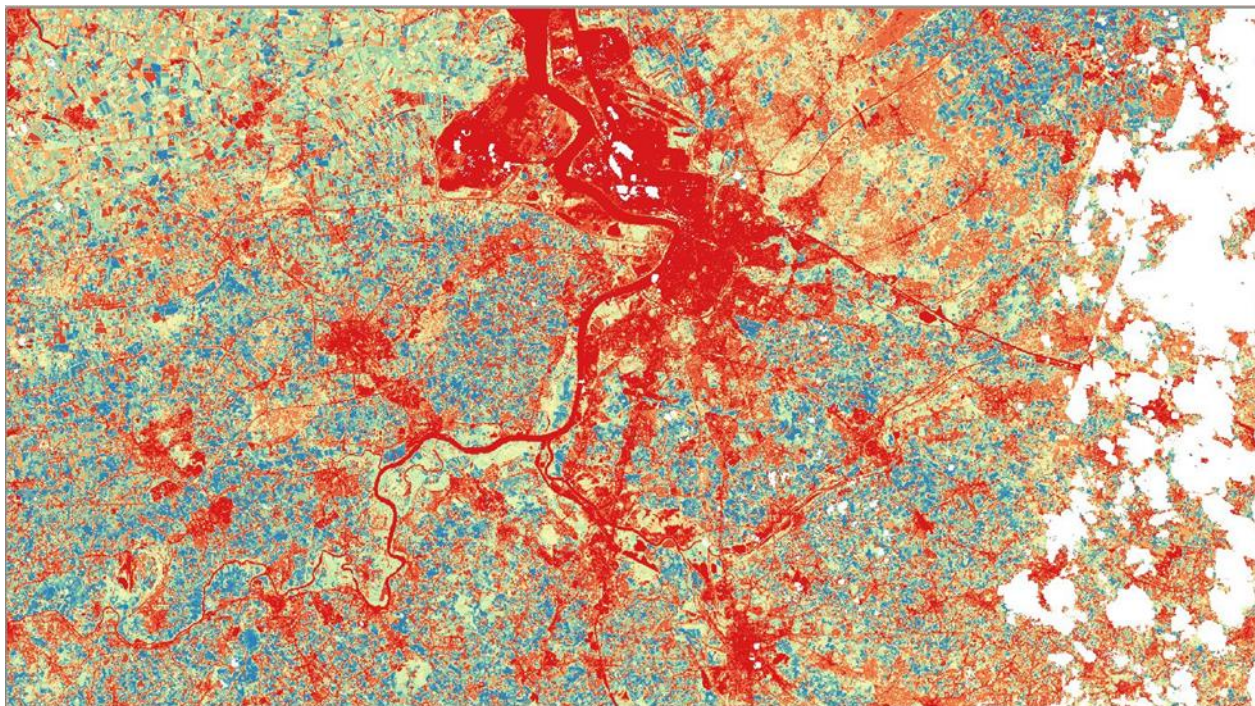


**Figure 5-5: K-Means resulting image, with 30 classes, based on the maximal NDVI values for a year. The white dots being no data due to the presence of clouds**

Each phenological parameter listed in Table 5-3 are then manually determined by plotting the monthly maximal values of the NDVI, averaged for each class – as depicted in Figure 5-6 to Figure 5-9.

**Table 5-3: Phenological parameters (start, peak, end and length of season) manually determined for each of the 30 classes, as well as mowing event appearances**

Class	Start of	Peak of	Length of Season (in)	End of	Mowing	Mowing
1			No season			
2			No season			
3			No season			
4	May	July	6	October	-	-
5	April	June	6	September	-	-
6	April	July	7	October	-	-
7	March	June	7	September	-	-
8	April	June	7	October	-	-
9	March	July	8	October	May	-
10	March	July	8	October	April	August
11	March	May	6	August	-	-
12	March	June	8	October	-	-
13	March	May	9	Winter	August	October
14	March	May	9	Winter	August	September
15	April	June	8	Winter	-	-
16	March	May	7	September	-	-
17	March	May	7	September	-	-
18	March	July	9	Winter	August	-
19	March	June	9	Winter	-	-
20	March	June	8	October	-	-
21	March	July	9	Winter	-	-
22	April	June	9	Winter	-	-
23	March	August	9	Winter	June	-
24	April	July	8	Winter	-	-
25	March	May	9	Winter	-	-
26	March	May	8	October	-	-
27	March	May	9	Winter	June	-
28	March	May	9	Winter	-	-
29	March	May	8	October	August	-
30	March	May	8	October	-	-

Once those parameters are determined for each class, a reclassification is undergone to separate classes by:

- the month of starting season growth;
- the month for the seasonal peak;
- the month for the end of season;
- the length of growth season.

Mowing events – that appear to take place once or twice per year, when looking at a monthly NDVI – have not been used as reclassification basis to produce one or several prototype rasters, since those kinds of particular phenological event are strongly dependent of the NDVI frequency used in the analysis. They are listed here as a way to justify the number of classes selected for the K-means algorithm. Fewer classes, around 15 for example, would have led to the fusion of classes that still display strongly different behaviour from a phenological point of view. More classes, such as 40 to 50 classes – lead to a fragmentation of the landscape at a sub-field level, which would have required another step to regroup classes exhibiting the same behaviour. The qualitative assessment of the classification at 30 classes shows a spatial consistency at field scale.

The 3 first classes exhibiting no seasonal variations over the year, seen in Figure 5-6, can be linked to water bodies presence, sealed areas and bare soils, using the CLC dataset for 2012 as well as the 2015 HRLs for comparison. The following Figure 5-7, Figure 5-8 and Figure 5-9, show the 27 other classes – as well as the classes exhibiting mowing events, isolated on Figure 5-10.

The PSS layer shows that the start of season usually takes place between March and May, while the peak of season appears between May and August, as the PPS layer displays it.

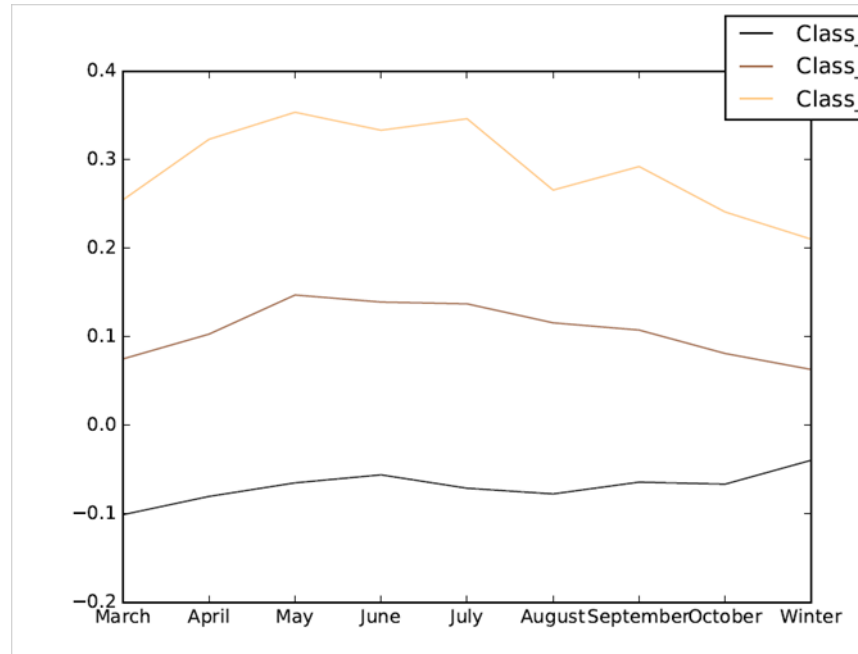
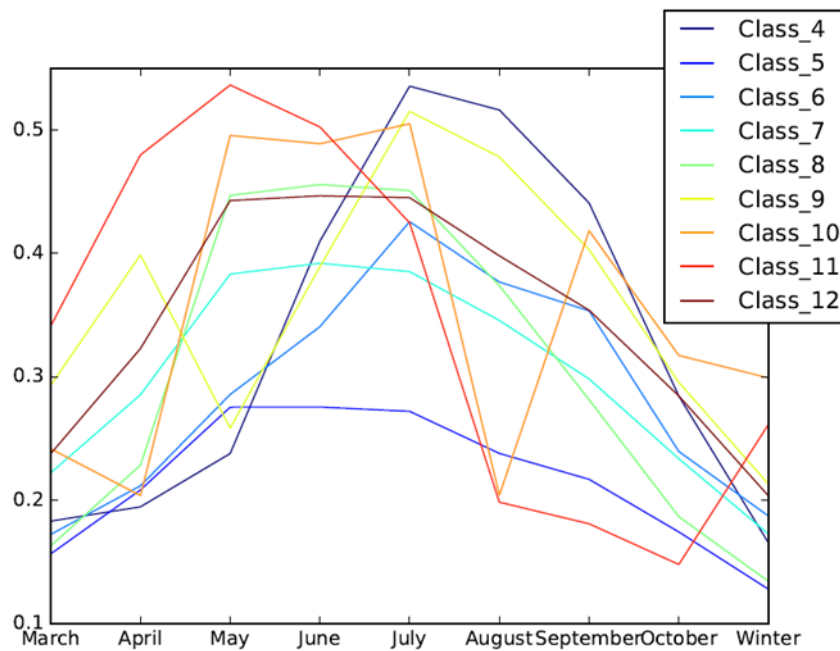
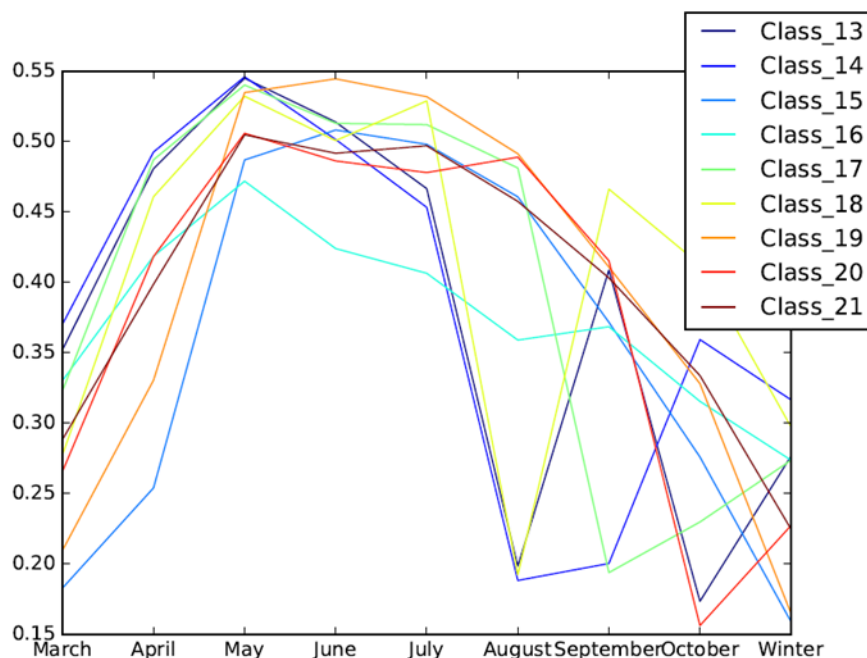


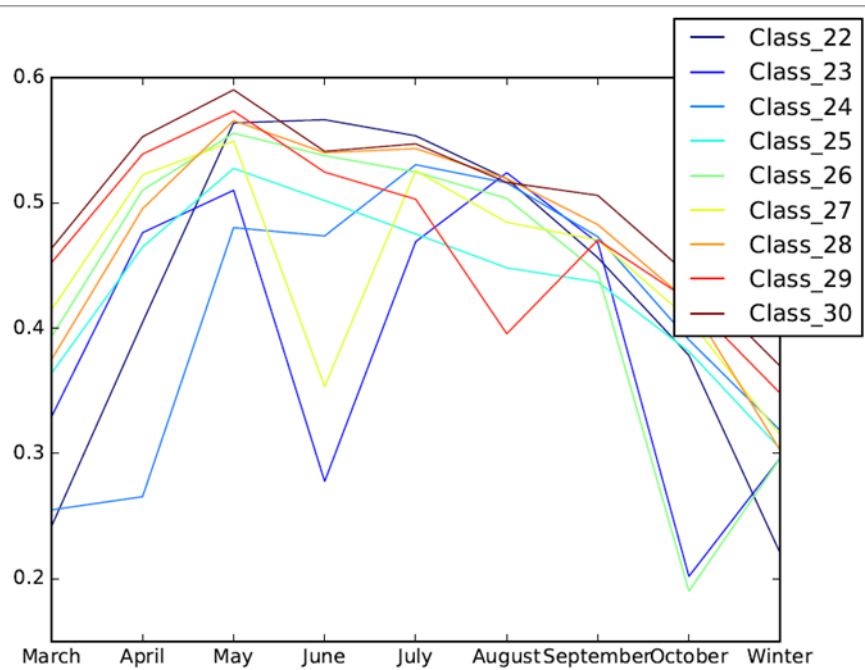
Figure 5-6: 3 classes exhibiting no seasonal variations during the year



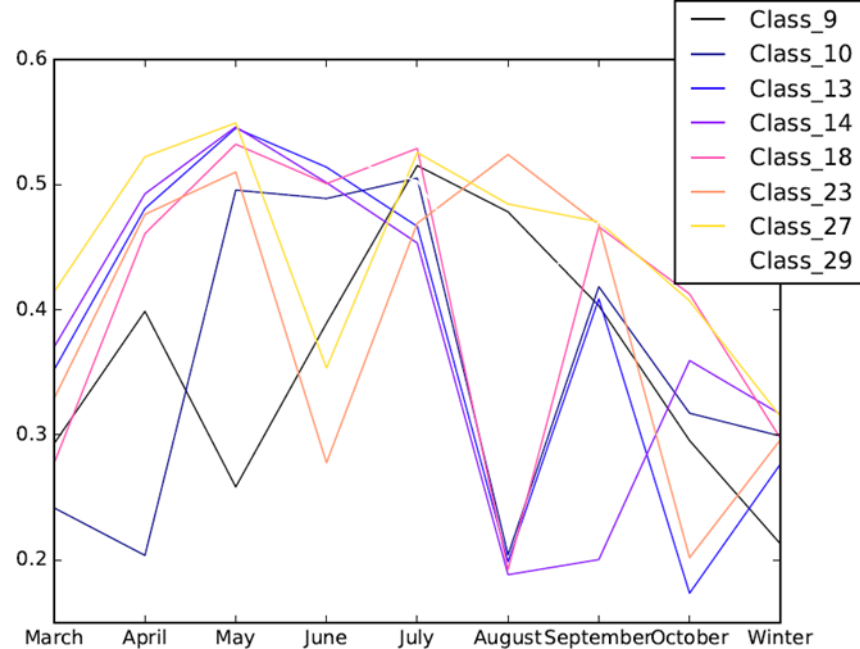
**Figure 5-7: 9 first following classes as listed by the clustering algorithm - the NDVI is much higher and variable than for the 'no-season' classes**



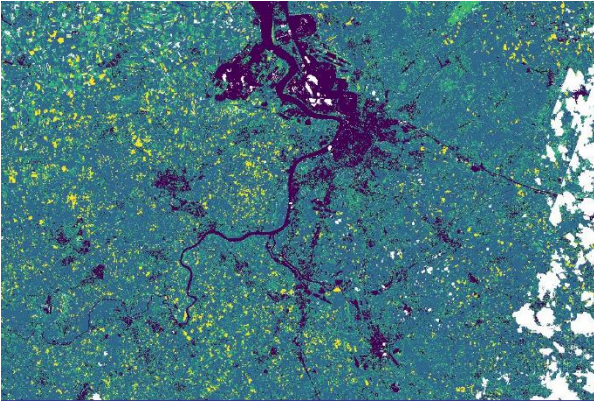
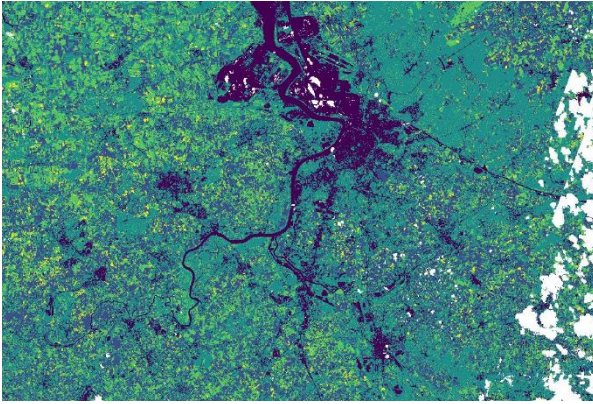
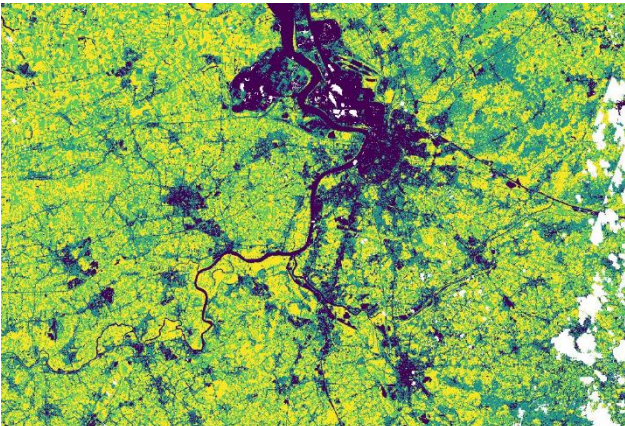
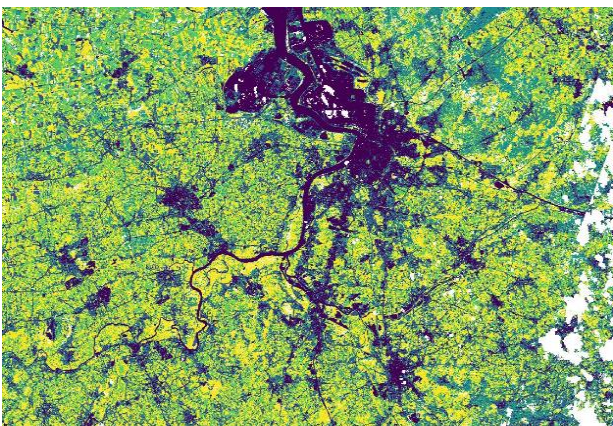
**Figure 5-8: 9 second following classes as listed by the clustering algorithm - the NDVI is much higher and variable than for the 'no-season' classes**



**Figure 5-9: 9 last following classes as listed by the clustering algorithm - the NDVI is much higher and variable than for the 'no-season' classes**



**Figure 5-10: Classes displaying mowing events at various months of the year**

	
PSS layer (March, April, May, no season and no data)	PPS layer (May June, July, August, no season and no data)
	
PES layer (August, September, October, Winter, no season and no data)	PLS layer (6, 7, 8, 9 months, no season and no data)

**Figure 5-11: Layers generated by the reclassification: PSS (phenological start of season), PPS (phenological peak of season), PES (phenological end of season) and PLS (phenological length of season)**

The end of season can sometimes be difficult to determine with the presence of mowing events, this is why only the PES layer has been created. The PLS layer, regarding the length of the season, has been derived from the PSS and the PES layers. A zoom, located in the region of Antwerp, on those different layers can be seen in Figure 5-11.

It should be noted that:

- The peak of season can sometimes be difficult to determine due to the design of the NDVI, which is known to compress high ratio values, leading to a saturation for dense canopies and an underestimation of the green biomass for strong foliage density (Wang et al., 2005). The introduction of other spectral indices could result in a better discrimination between dense vegetation types.
- The temporal frequency of a month to perform the NDVI statistics sometimes seems to be slightly too large to fully account for the difference in phenological behaviours, even more with the fusion of winter months due to the persistent cloud cover. A bi-monthly or twice a month frequency to compute the maximum value of the NDVI could be interesting to explore, it but would need a denser time series – the addition of S-3 datasets resampled at the S-2 resolution could improve the study, as well as the fusion with S-1 inputs.

Finally, it should be noted that Phenological layer validation is still an open subject as it requires in-situ data or very high spatial resolution image time series. In both case, amount of data to process for validation purpose is still challenging and no solution has been found yet.

In the second phase, the results provided by the algorithm TIMESAT is indeed based on a bi-monthly interpolated S-2 images, and leads to more precise parameters determination.

This time, the key parameters of the NDVI seasonality are provided into the attribute table of each prototype, and not in different raster layers. An illustration over the T32TNT tile can be seen in Figure 5-12.

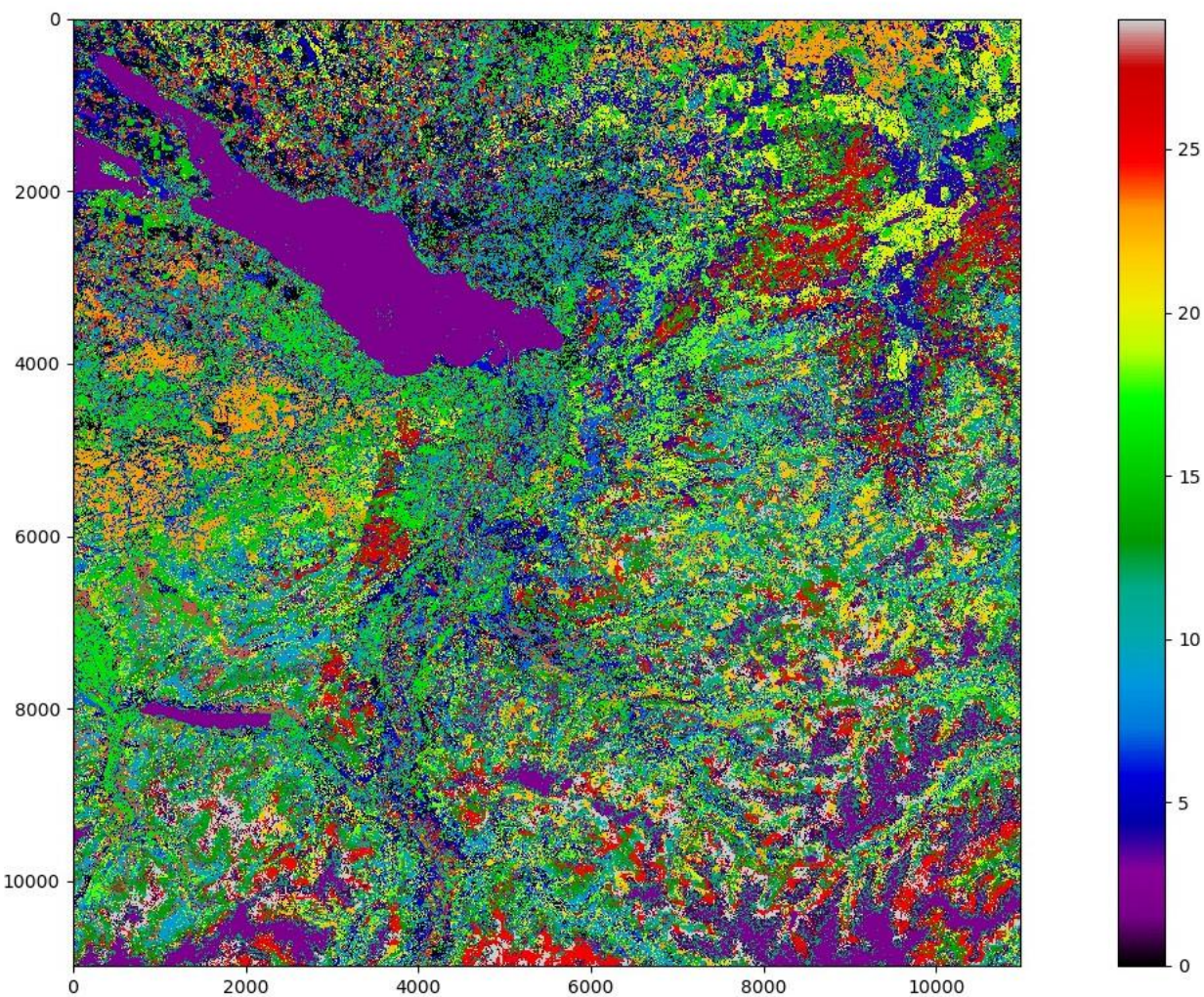


**Figure 5-12 - Various classes of phenological activity over the T32TNT tile from the Central demsonstration site.  
The coherence of the landscape can clearly be seen.**

## 5.2.2 Crop growth condition

The crop growth condition at field level have been computed in relative terms for three main crops with regards to its local neighborhood, i.e. the average of all the fields belonging to the same crop within a 3 km radius from the field of interest. The LAI values for each field belonging to one of the crops of interest in Southern Belgium (winter wheat, winter barley, and maize) have been retrieved using all the available observations from the Sentinel-2 time series. It was found very important to define appropriate periods

corresponding to the growth cycle of each crop. These are for winter wheat and winter barley from week 9 to week 31 (27/02/2017 - 06/08/2017) and for maize from week 18 to week 43 (17/04/2017 - 29/10/2017).

From the LPIS for 2017, 28,017 fields of winter wheat were characterized at parcel level by their LAI profile fitted to the available Sentinel-2 observations. Crop growth condition was also described for 22,898 fields of maize and 9158 fields of winter barley. The profile of any field of interest is plotted against the local average profile to assess the crop growth condition in relative terms. Six different fields are illustrated here for the three different crops (Figure 5-13, Figure 5-14, Figure 5-15) highlighting the diversity of situations between the field of interest and the local average: earliness, better status at the end of the winter, higher maximum, late maturity, etc. The observed difference between the field profile and the local average can be due to a late sowing just shifting the whole growing cycle for 2 to 3 weeks (Figure 5-13). The early planting does not always translate into a higher LAI peak nor an earlier harvest depending to each field. Some very synchronized fields with their neighborhood still outperforms the local average by their LAI peak probably due to better soil management or to high potential variety.

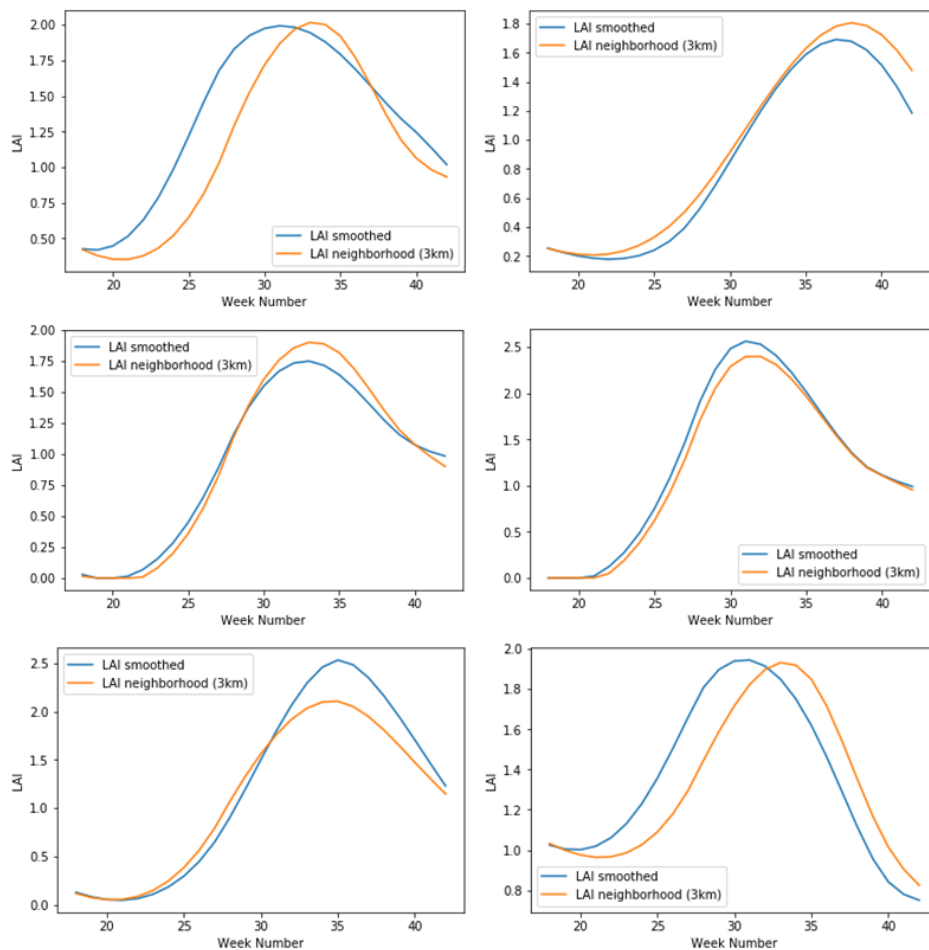


**Figure 5-13: Characterisation of the crop growth condition of six different maize parcels for 2017. The orange LAI profile corresponds to the local average of all the maize fields within a radius of 3 km, excluding the field of interest plotted here in blue**

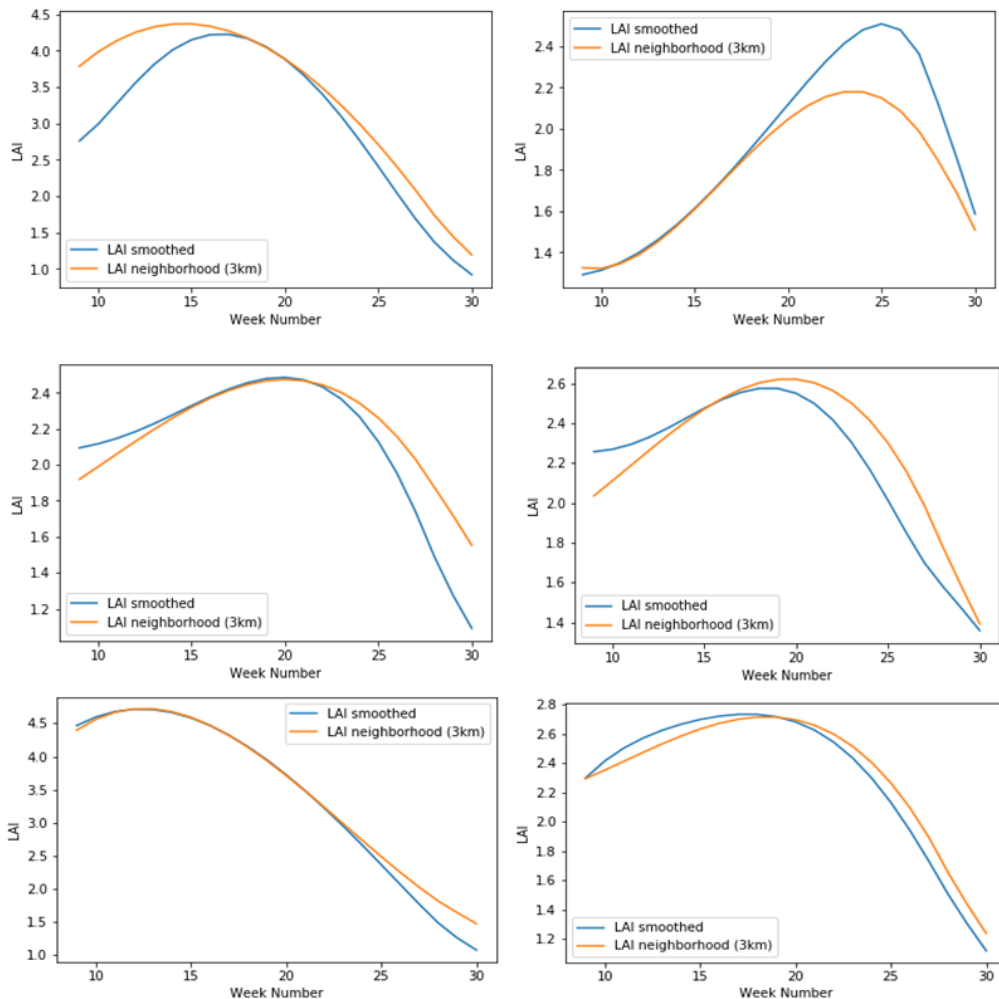


**Figure 5-14: Characterisation of the crop growth condition of six different winter wheat parcels for 2017. The orange LAI profile corresponds to the local average of all the maize fields within a radius of 3 km, excluding the field of interest plotted here in blue**

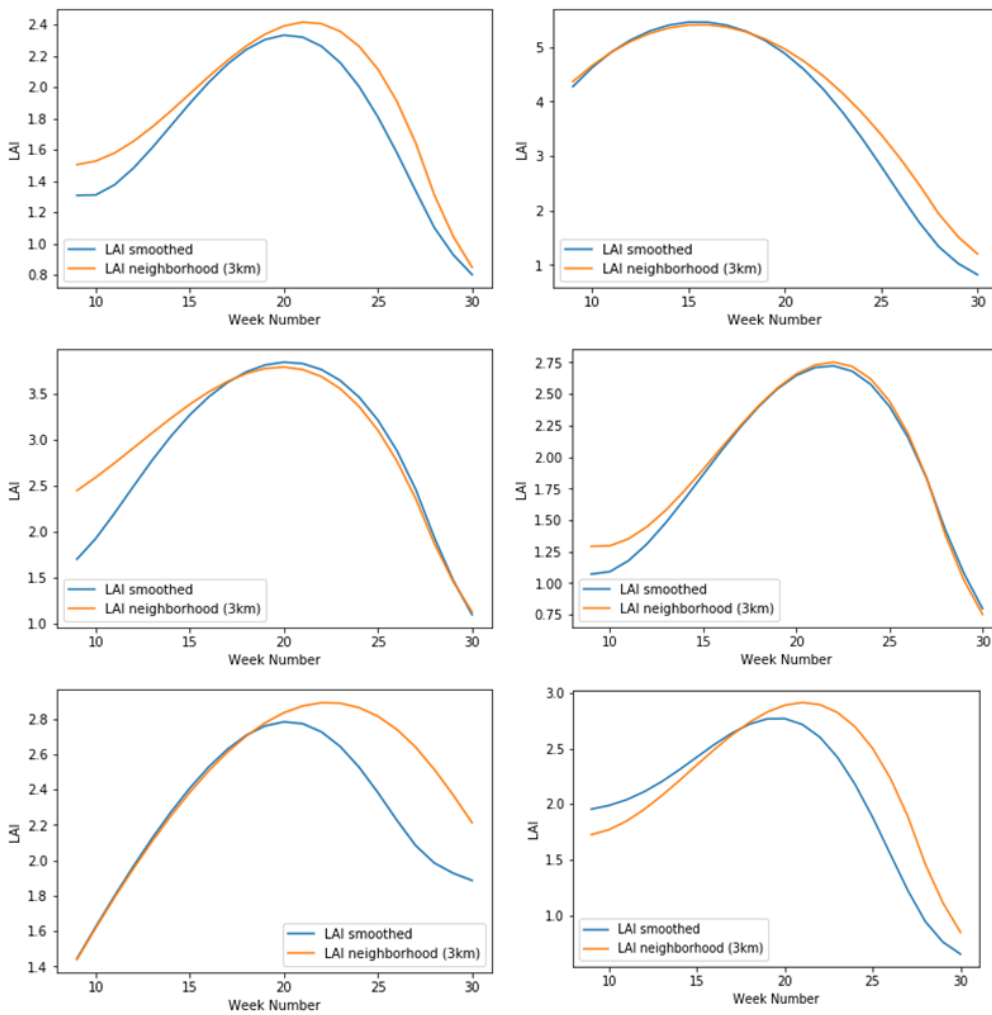


**Figure 5-15: Characterisation of the crop growth condition of six different winter barley parcels for 2017. The orange LAI profile corresponds to the local average of all the maize fields within a radius of 3 km, excluding the field of interest plotted here in blue**

A more quantitative assessment of the difference between any field and its local average is defined by the LAI anomaly. This local LAI anomaly is defined by the difference between the area under LAI curve for the field of interest and the one for the local average. The overall distribution of the LAI anomalies for each crop is presented at Figure 5-16. The winter wheat distribution is rather narrow and centred to the null values illustrating a rather homogeneous crop growth condition. The distribution is even narrower for the winter barley while a bit skewed towards negative anomaly. The maize distribution illustrates much more heterogeneous crop growing conditions because maize is spring crop planted the last in most cases. Indeed maize is mainly a forage crops sowed after sugar beet and potato and harvested at various stages depending on the final use.

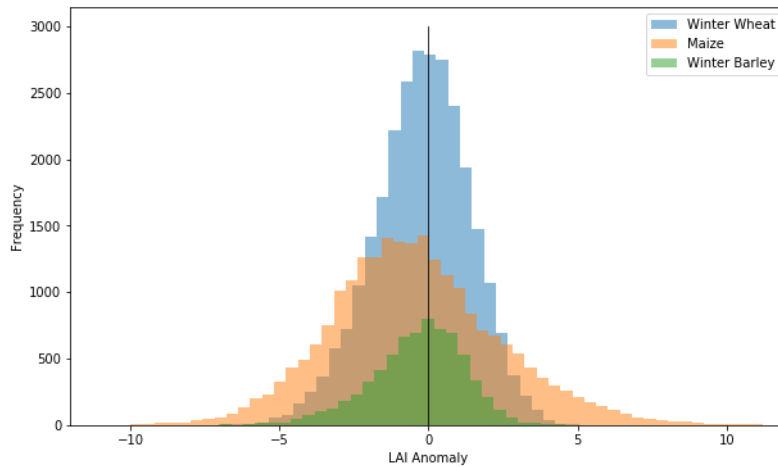


**Figure 5-16: Distribution of the local LAI anomalies for the three main crops in 2017. The anomaly corresponds to the difference between the area under LAI curve for the field of interest and the one for the local average**

The local LAI anomalies computed for each parcel have been mapped for the entire data set. Various zooms illustrated the various patterns of the local growing conditions for the three crops are reported for illustration in the figures Figure 5-17 to Figure 5-19.

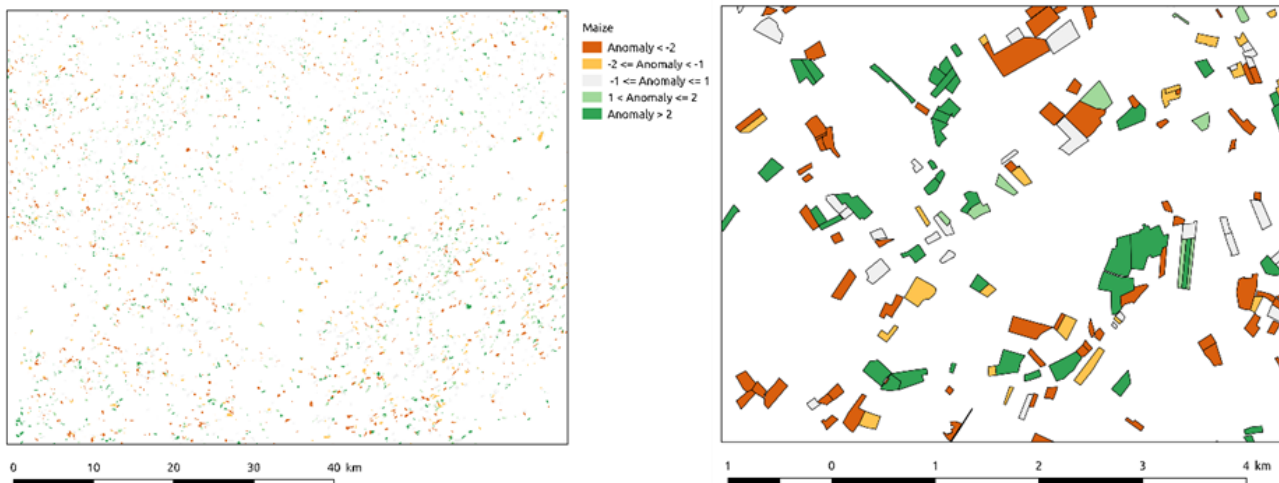


**Figure 5-17: Map zooms of the maize anomalies for 2017**

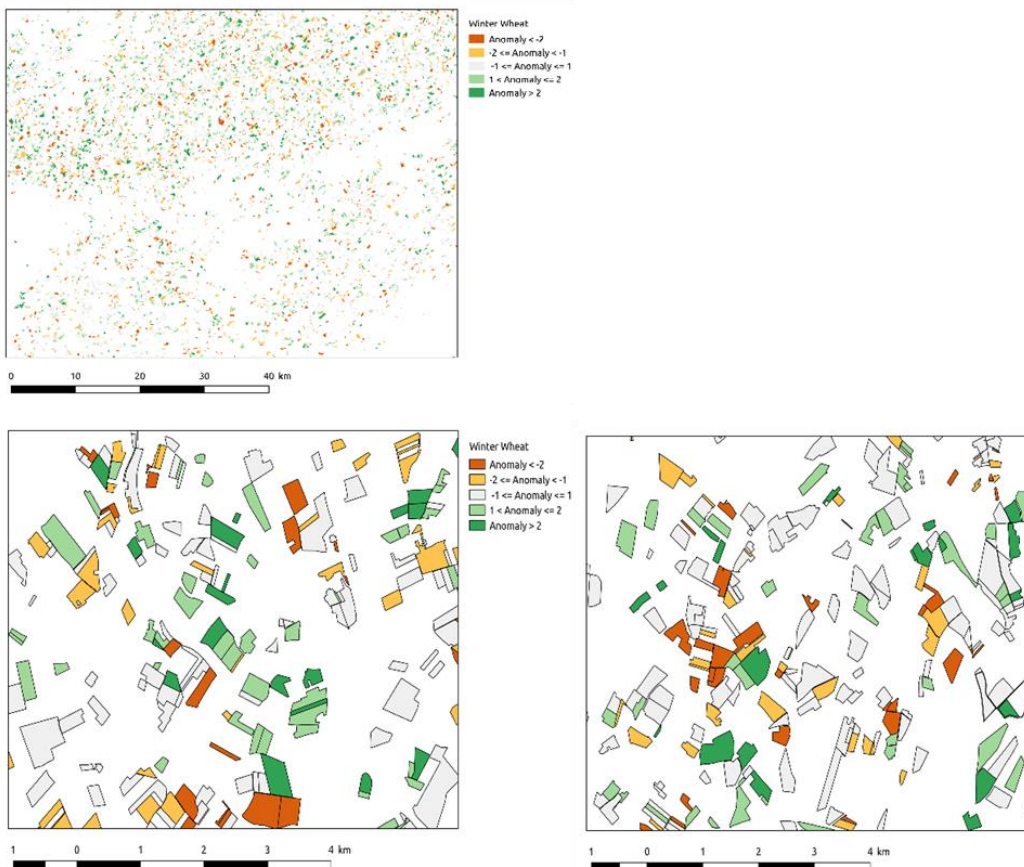


Figure 5-18: Map zooms of the winter wheat anomalies for 2017

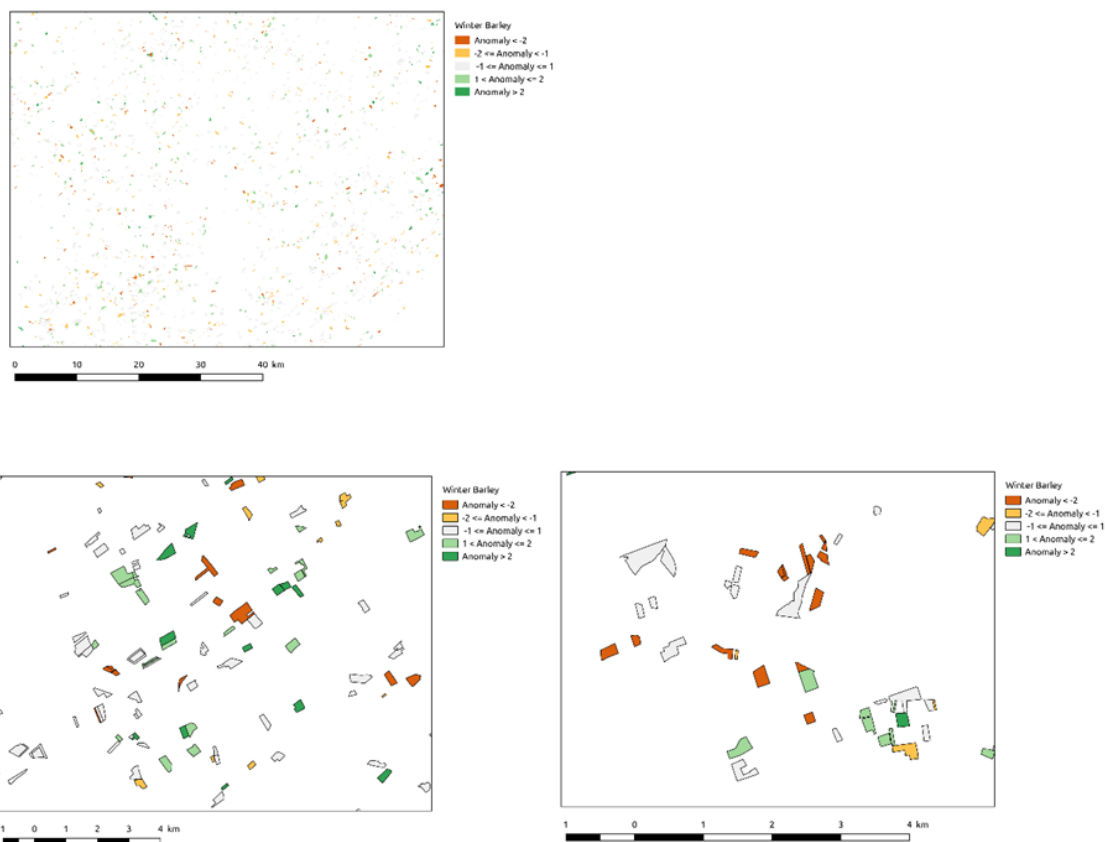
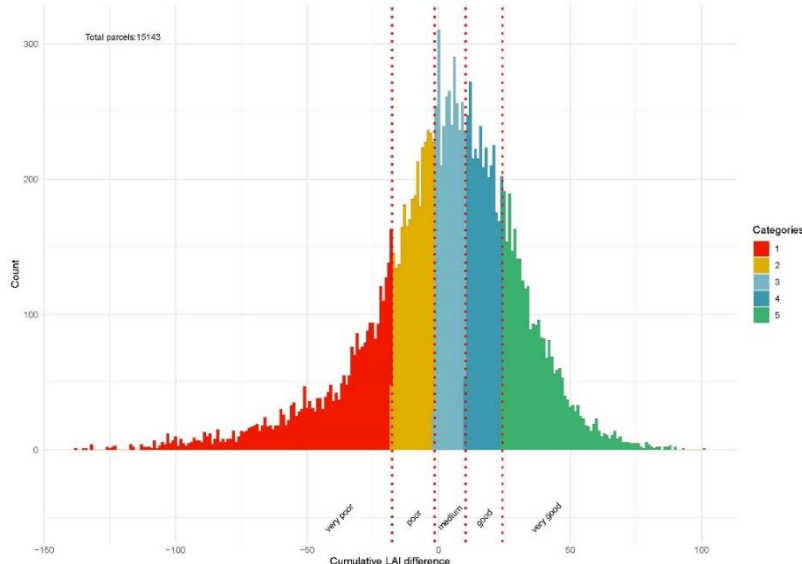


Figure 5-19: Map zooms of the winter barley anomalies for 2017.

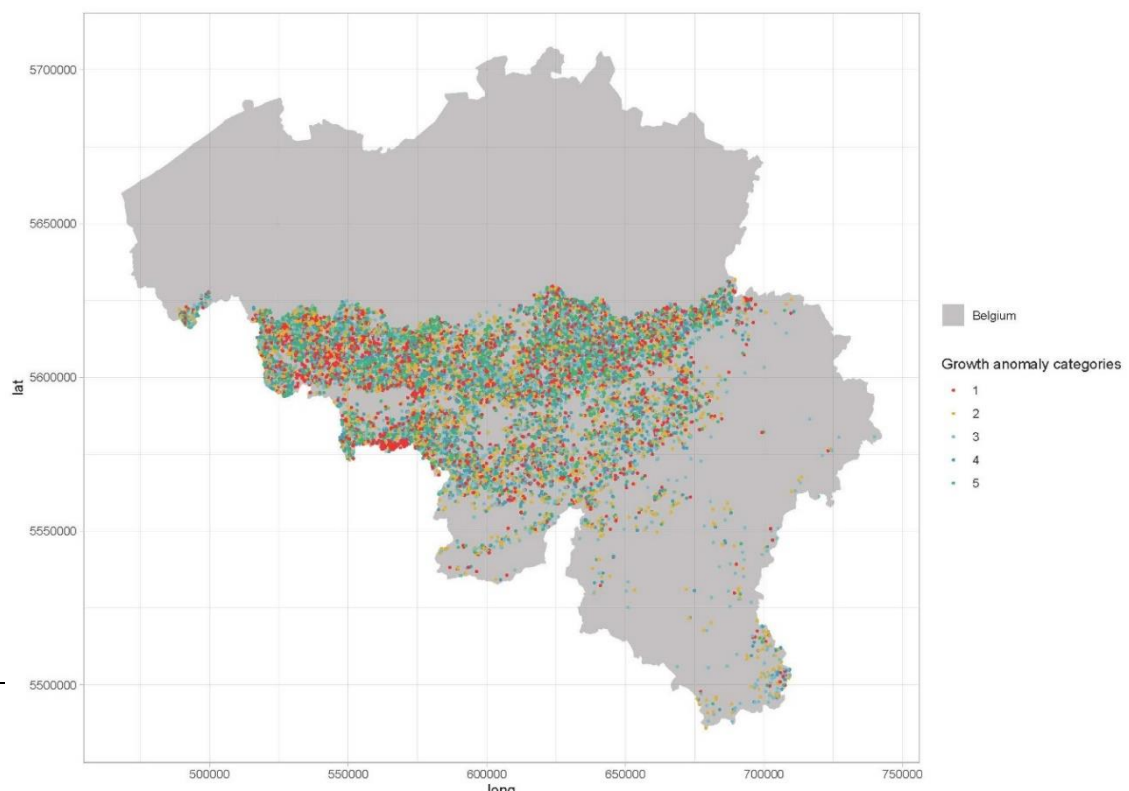
In the phase 2, the demonstration prototype was implemented for the 15,143 parcels of wheat for 2018 growing season. The crop growth anomaly focus on a specific period corresponding to the vegetative phase of the crop, i.e. from the LAI minimum at the early stage to the LAI maximum. Indeed this is a period when the diversity of agriculture practices impacts most the vegetation growth. Another improvement with regards to the 2017 prototype consists in a more informative threshold separating the categories according to the cumulative distribution (Figure 5-20). The thresholds are set to different quantiles of the distribution (<20%, 20- 40%, 40-60%, 60\_80%, >80%) to define 5 classes (1-5) respectively corresponding to very poor , poor, medium, good, very good. The local heterogeneity of the crop growth condition (high local LAI anomalies) appears much higher in the Western part of the map



(Figure 5-21).

**Figure 5-20: Distribution of the 2018 local LAI anomalies in the demo-site West (Wallonia) expressed as the cumulative LAI difference for the vegetative period (min LAI to max LAI) between the field of interest and the local LAI average of the wheat fields within 3km radius around the given field.**

**Figure 5-21: Spatial distribution of the local LAI anomalies for the 2018 wheat season (demo-site West, Wallonia)**



### 5.2.3 Multiannual trends and potential changes based on SAR data from S-1

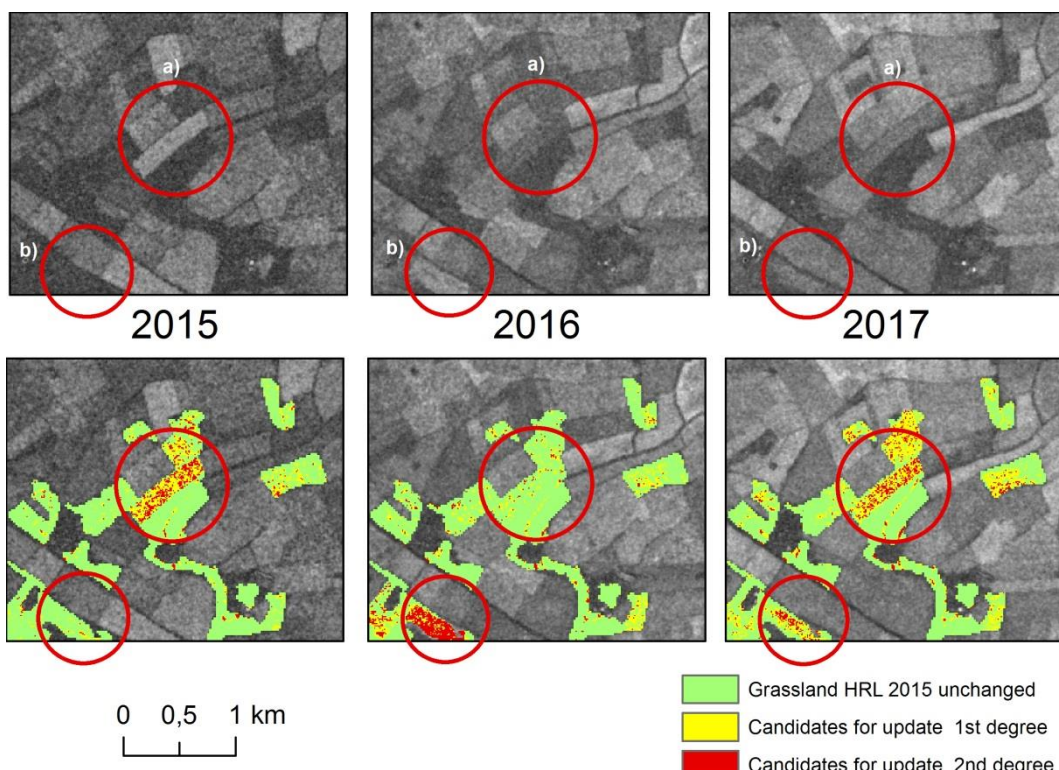
Based on the methodology presented in chapter 4.3 results for the demo site Belgium and the HRLs Forest and Grassland were calculated and analysed.

For the subsequent analysis of multiannual trends based on S-1 data, the complete time series of 2015, 2016 and 2017 had to be pre-processed (note that within WP32 only the time series of 2017 has been processed). Due to time constraints, the pre-processing could only be performed computing the sigma nought backscattering instead of the flattened gamma nought. However, it is envisaged to perform the same analysis with the S-1 time series data pre-processed to the flattened gamma nought in the second phase of the project. Hence, also the analysis on the usability of the gamma nought backscattering will feed back into the WP32 deliverable.

The multi-annual trend analysis has been performed for the a) Grassland HRL, and b) Forest HRL. In the following, the results of these analyses are described into detail.

#### **Grassland**

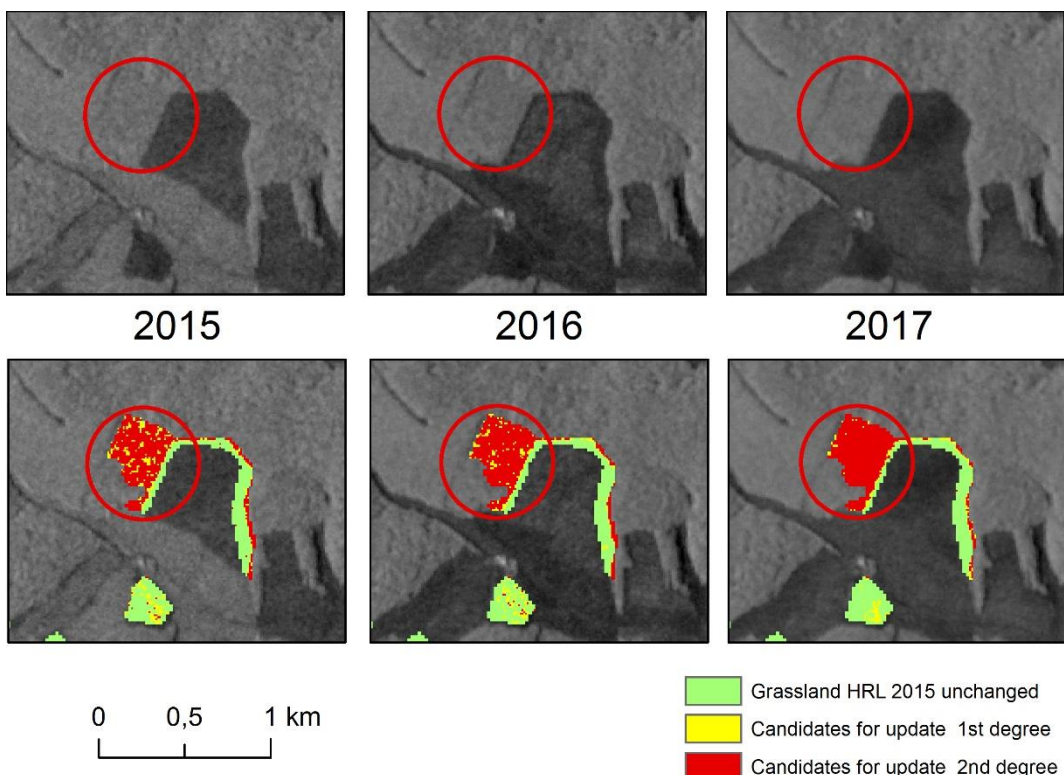
Figure 5-225 and Figure 5-23: present two different areas of the Belgium test site where grassland areas were detected for a possible update of the HRL Grassland class. Based on visual inspection of the processed tiles the suggested approach shows promising results for the Grassland HRL where agricultural and forested areas in the grassland HRL where detected for an update.



**Figure 5-22: First example of HRL grass updates for three consecutive years. Above: background layer for visual comparison of surrounding land cover. Below: detected pixels for possible update**

Figure 5-22 shows an area dominated by agricultural use. Here, the temporal behaviour of few distinct fields varies from the mean temporal behaviour of the grassland class. The field marked by the large red circle seems to be grassland in 2016. However, it does not show the same characteristics in the S-1 feature space in 2015 and 2017. Hence, it is questionable that this field is really grassland in 2016, but rather an agricultural field, which has been in fallow in 2016 as a usual practise in agricultural crop rotation. Due to the similarity of grassland and fallow land, this field could have been detected as grassland in the HRL Grassland in 2016. The same could also be true for the field marked by the smaller red circle, although the years of the fallow situation differ.

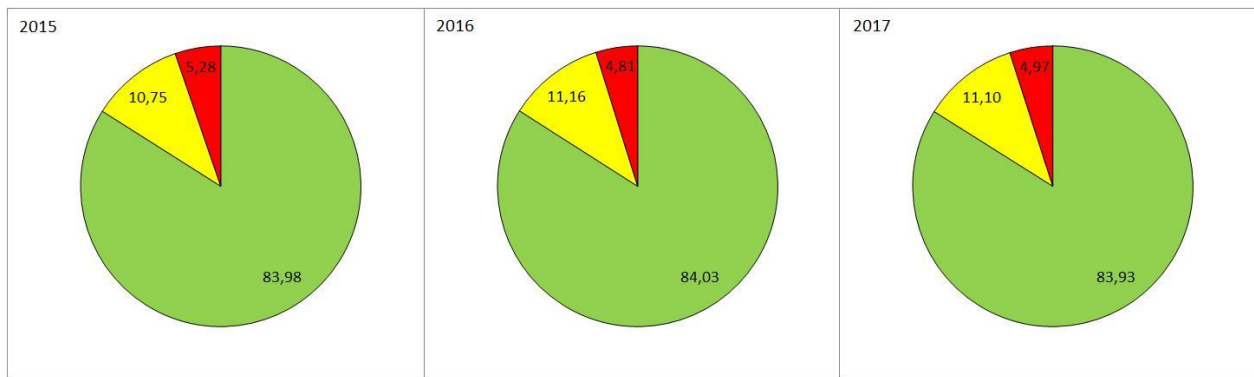
Figure 5-23 shows an area dominated by forests. Here, the field marked by the red circle, which has been classified as grassland in the HRL Grassland, does not show the usual characteristics of grassland in the S-1 feature space in all three years. It can be assumed that this field could rather be a young forest which has been afforested just recently and thus, behaviourist characteristics are similar to grassland. Furthermore, it seems that more pixels are classified to the 2<sup>nd</sup> degree category of change over the years, which could indicate that the forested area is growing and becoming denser.



**Figure 5-23: Second example of HRL grass updates for three consecutive years. Above: background layer for visual comparison of surrounding land cover. Below: detected pixels for possible update**

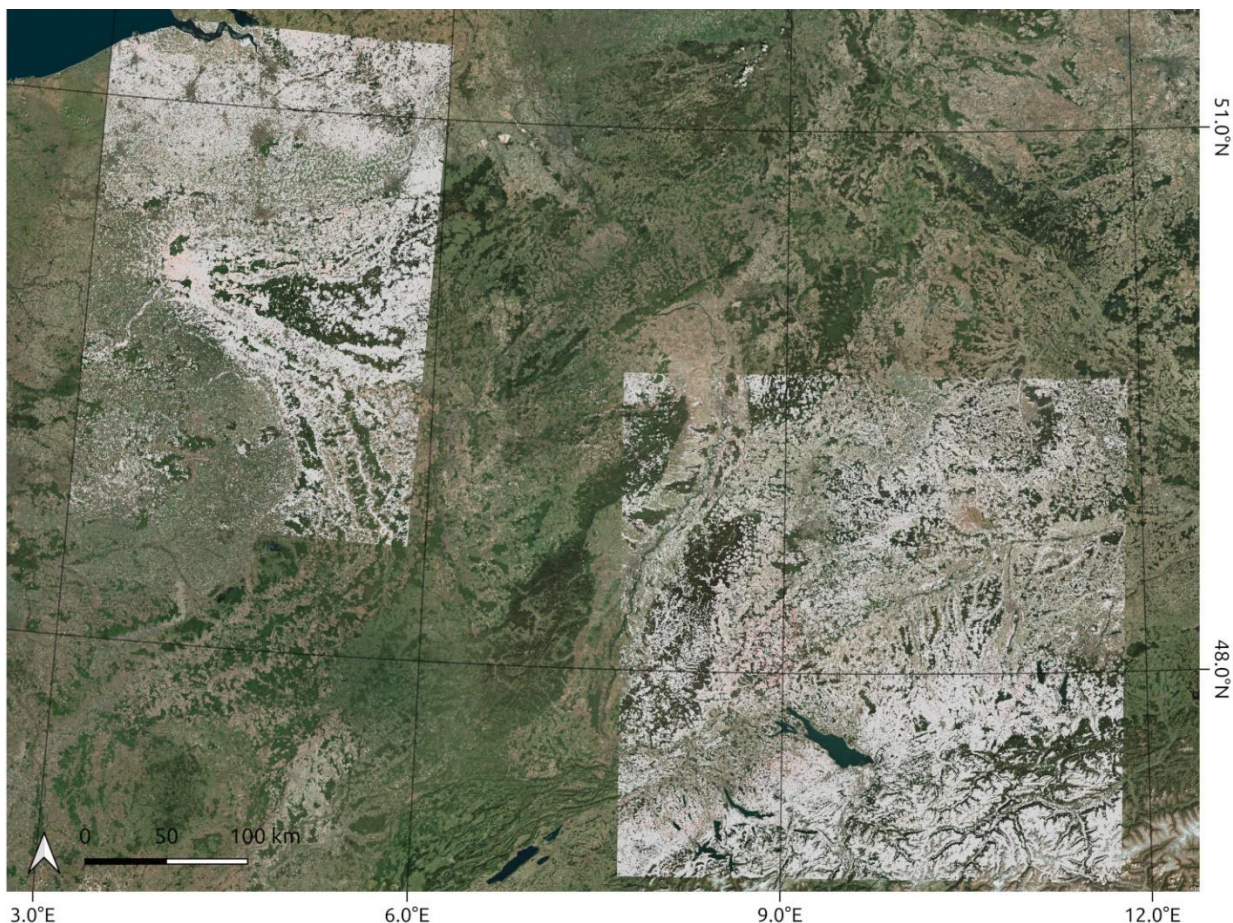
However, there seem to be are two major sources of misclassification: this approach wrongly detects a) few pixels as well as small patches of pixels which might still belong to the original class (due to the speckle within the SAR data); and b) potential change in areas influenced by radar shadow (e.g., at the border of forests). This could be resolved by applying on the one hand a further filtering of the original dataset by means of a multitemporal filter in case of the speckle and by using the flattened gamma nought instead of the sigma nought data.

The rate of total detected pixels for update for the demo site over the three years is visualized in Figure 5-24. It shows that approximately 84% of HRL Grassland pixels were stable and that the rate of category 2 was around 5%. The rate for category 1 within  $\pm 2$  standard deviations) was around 11%. This category includes also many noise pixels and will probably decline if object-based and /or areas-based analyses are included in addition to pixel-level analysis.



**Figure 5-24: Identified pixels (in %) for update across three years of the demosite for HRL grass. Stable and not change pixels (green), category 1 for update (yellow), category 2 for update (red).**

#### Phase II



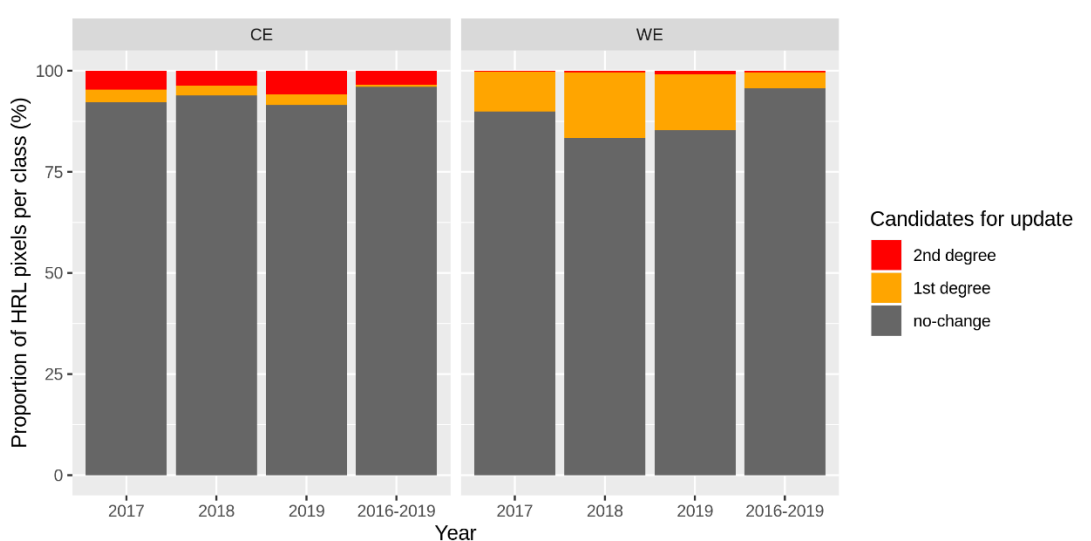
**Figure 5-25 Overview over the TSI Grassland aggregate layers 2016-2019 for the demonstration sites West and Central. Note that the appearance of high percentage grassland cover is due to overview resampling for better display at the large scale of this figure.**

Figure 5-25 Overview over the TSI Grassland aggregate layers 2016-2019 for the demonstration sites West and Central. Note that the appearance of high percentage grassland cover is due to overview resampling for better display at the large scale of this figure. Figure 5-25 shows an overview over the produced multi-annual TSI aggregate prototypes (2016-2019) for the West and Central sites. The statistics of the relative number of affected pixels gives a different picture in the two demonstration sites (Figure 5-26). For the central site, aggregated across all years, 96.03% of grassland pixels were flagged as no-change, 0.51% were flagged as 1<sup>st</sup> degree candidates and 3.46% were flagged as 2<sup>nd</sup> degree potential change candidates. Contrastingly, while in the demonstration site West also 95.67% of grassland pixels

were categorized as no change overall, almost all detected potential changes were found in the 1<sup>st</sup> degree potential change category (3.99%) and almost none in the 2<sup>nd</sup> degree category (0.35%).

Considering each year individually led to higher numbers of pixels being flagged as either change category (Figure 5-26). Apart from classification errors, this is an indication of the influence of the multiple drivers to which the TSI is sensitive as discussed in Section 4.3. In particular in the demonstration site West the individual year's TSIs of the 1<sup>st</sup> degree potential change category were much more frequent (9.88%, 16.20% and 13.84% for the years 2017 to 2019), but not consistent, resulting in the reduction to 3.99% in the multi-year TSI.

This importance of aggregating over changes in single years is also shown in Figure 5-27 Temporal development of the Grassland TSI over three consecutive years as well as their fusion into the more robust aggregated 2016 – 2019 TSI in the demonstration site Central. Figure 5-27, which shows an example of the TSI in the years 2017, 2018 and 2019 as well as their aggregated TSI. The aggregated TSI shows a much clearer picture of potential update candidates. Moreover, interestingly it is mostly, although not exclusively, 2<sup>nd</sup> degree changes which are stable throughout the years. This could be an indication that the threshold for 1<sup>st</sup> degree change candidates (i.e. 2 standard-deviations around the mean) was chosen too conservatively and flags intra-class variability which is not related to changes, because it is not stable over the years.



**Figure 5-26 Proportion of HRL grassland pixels belonging to one of the TSI change classes for the Central site (left) and the West site (right).**

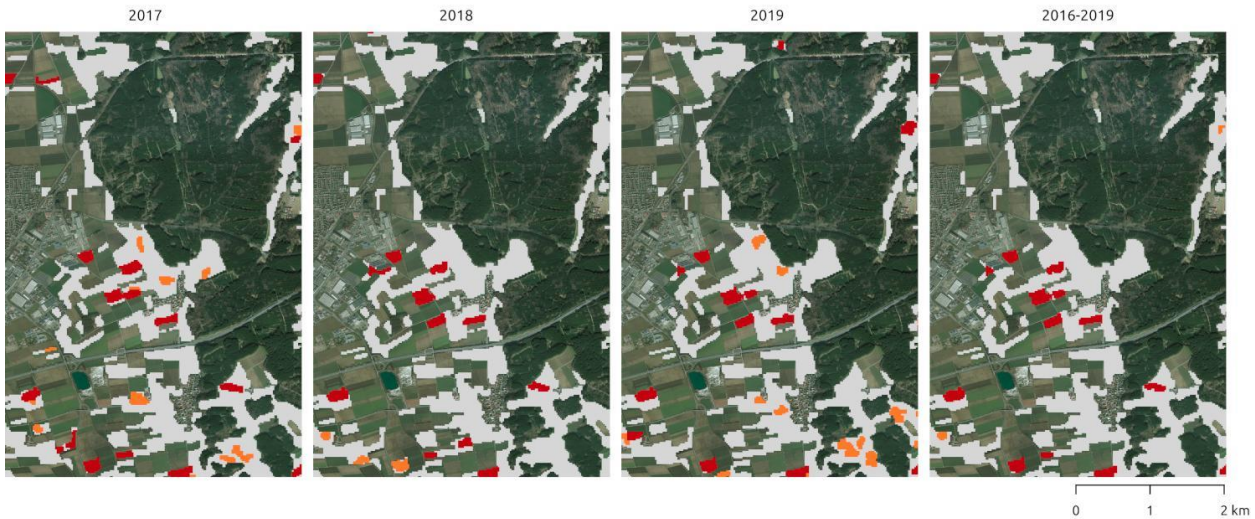


**Figure 5-27 Temporal development of the Grassland TSI over three consecutive years as well as their fusion into the more robust aggregated 2016 – 2019 TSI in the demonstration site Central.**

### Forest

The approach was also tested for the Forest HRL. In the following, the examples for the Forest HRL are presented and discussed. Figure 5-28 and Figure 5-29 show two examples of the demosite West where candidate areas for HRL updates were detected. In both figures, certain areas (marked by circles) were detected, where the S-1 feature space characteristics were significantly different from the typical class characteristics for all 3 years. It seems that these “changes” were detected for areas which are affected by terrain and canopy height induced effects (higher backscattering from slopes facing the sensor, lower backscattering from slope away from the sensor). Unfortunately, the effects of terrain are quite obvious which leads to an identification of many change areas not because of a class change but rather because the received signal differs significantly depending on the slope.

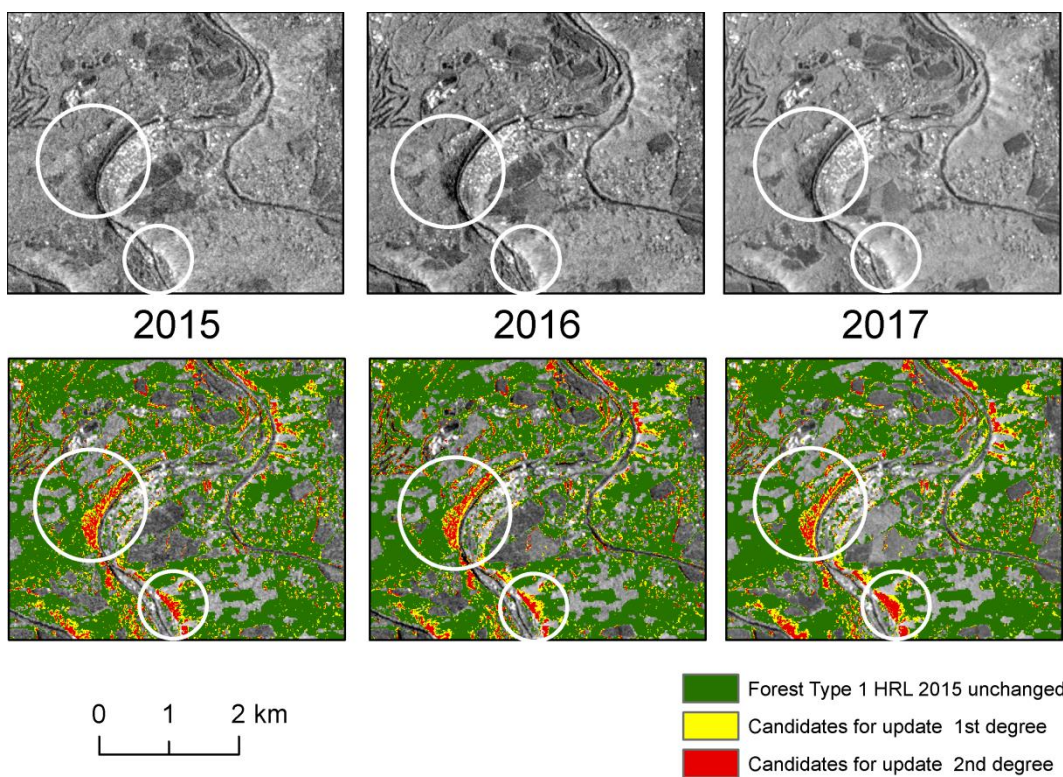


**Figure 5-28: First example of HRL forest updates for three consecutive years. Above: background layer for visual comparison of surrounding land cover. Below: detected pixels for possible update**

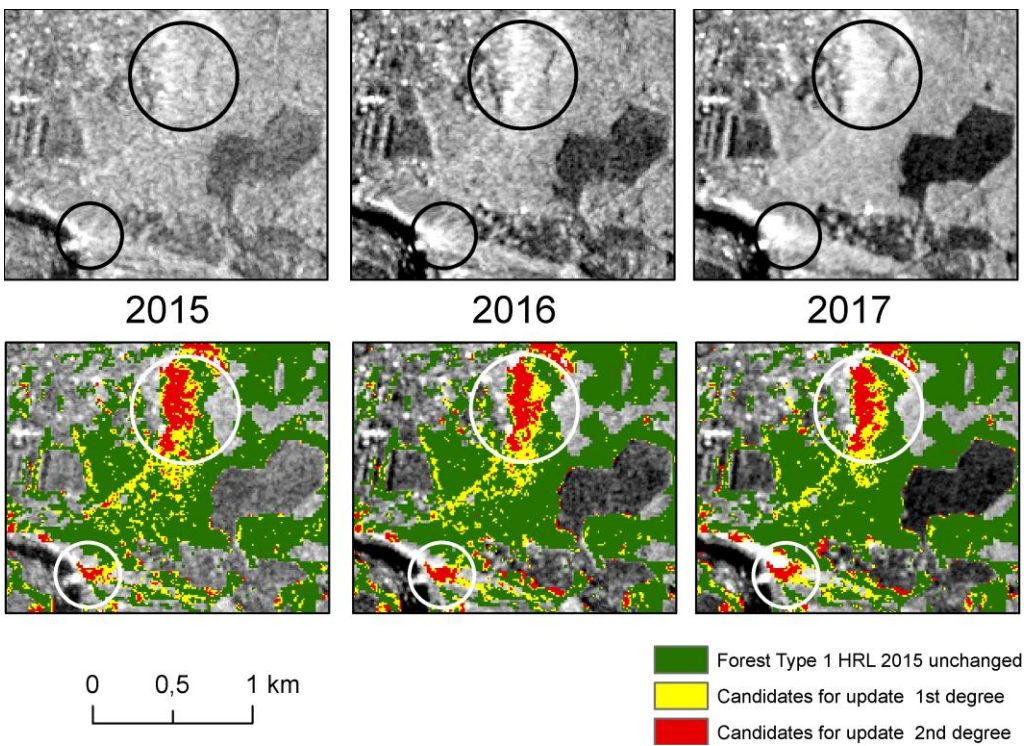


**Figure 5-29: Second example of HRL forest updates for three consecutive years. Above: background layer for visual comparison of surrounding land cover. Below: detected pixels for possible update**

Particularly regarding the HRL Forest, the use of different input data (e.g. gamma nought where the influence of terrain is less dominant) could result in a more realistic update. Apart from the identified pixels influenced by terrain effects, the approach also found areas where forest was indeed replaced by another class. Figure 5-30 shows one example (marked by circles) where non-forested pixels are detected for an update. These areas are adjacent to actual forest and were either misclassified in the HRL Forest or were indeed deforested.

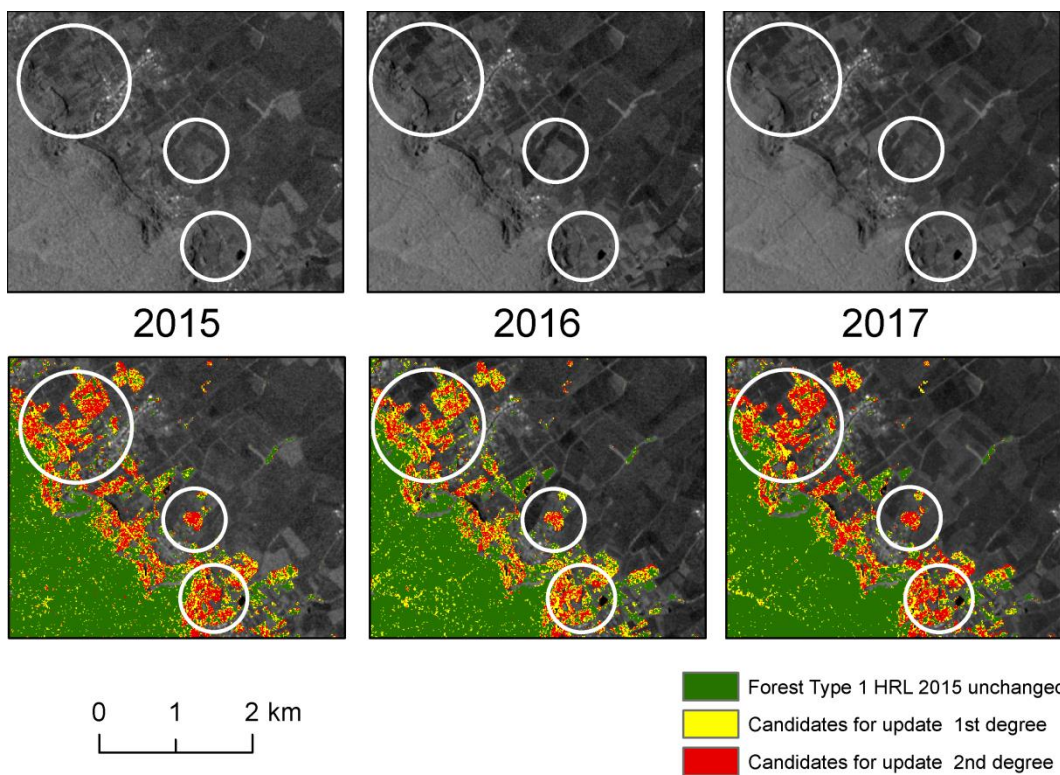


**Figure 5-30: Third example of HRL forest updates for three consecutive years. Above: background layer for visual comparison of surrounding land cover. Below: detected pixels for possible update**

## Conclusion

Building on the method development in phase I, in phase II in total 24 S-1 TSI prototype layers were produced, covering the demonstration sites West and Central for the years 2017, 2018 and 2019, and focusing on the HRL classes Grassland, Deciduous Forest and Coniferous Forest.

The TSI derived from S-1 time-series has been found to provide an informative metric for the identification of pixels which stray far from the class mean in feature space or which are in fact changing the LC class and are likely candidates for an update during the next HRL production. Challenges from phase one of noisy pixel-based TSI values could be overcome by subsequent filtering for 0.5ha MMU.

While the approach does highlight potentially changing areas, it remains challenging to disentangle LC changes from gradual changes and other external factors. To a degree, aggregating the individual year's TSIs to an integrated multi-year TSI was found to be beneficial to reduce the amount of noise and increase the confidence into the "potential change indication", however this still cannot not separate actual change from naturally high variability. While the inter-annual aggregation results in more reliable change indicators, very recent changes become more difficult to detect.

Lastly the TSIs as proposed here depend on an accurate HRL classification in the first place. Mapping errors made during HRL production propagate to the TSI. Nevertheless, if mapping errors are minority cases, that is, they did not strongly influence the calculation of the reference class backscatter statistics, the TSI may in fact flag such pixels, not because they are "changing" from the HRL class but because they were miss-classified in the first place. Due to the nature of the TSI implementation highlights only the loss / conversion of a given HRL class, but not a gain thereof. While not the aim of this prototype, obtaining gain from the intermediate backscatter metrics could be achieved by other methods such as a clustering or other forms of feature space delineation.

Overall for GRA a higher proportion of pixels were counted towards the potential change categories of 1<sup>st</sup> and 2<sup>nd</sup> degree than for DLT coniferous or DLT deciduous. This may reflect a number of things. First, grassland backscatter may exhibit higher variability than forest backscatter due to the more pronounced phenology, hence the TSI is more likely to flag pixels as potential changes. Second, forest TSIs may require different threshold settings, which needs to be explored with actual in-situ data. Or third, there are indeed more changes in grasslands than in forest cover.

While, after visual inspection of all prototypes, the grassland TSI appears sensible, this cannot be stated for the forest TSIs at the moment. Further ground-truth aided adjustments of the thresholds must be investigated. Also regarding the grassland TSI it appears likely that it should receive further region specific tuning and that setting two constant thresholds may be insufficient. Nevertheless, even if the TSI does not necessarily only flag LC changes, it is expected to be a helpful resource for feature space exploration, which can be helpful, for example for stratified sampling or stratified validation of HRL layers.

### 5.2.4 Emergence date detection

The objective was to compare different VIs and detection methods to provide an accurate estimation of the emergence date at the field level. This experience demonstrated for maize that the relative threshold yields the most accurate estimate of the emergence date (about 10 days accuracy), probably due to the iterative adjustment process. More specifically, this method applied on NDVI time series provided a SD of 8.3 days and MAD of 7.4 days. Very similar results were obtained from MSAVI time series (I.e. a SD of 8.5 days and MAD of 7.4 days) with a very low coefficient of variation (2.9%) (Table 3-1Table 5-4). The results obtained for maize are most likely to be appropriate to other crops. The sunflower results are reported here because to the limited validation dataset.

Surprisingly, the absolute and relative thresholds do not present significantly different results, although the variations in sowing densities appear to affect the index values. This might notably be due to a relatively good homogeneity of the observed fields (high quality fields) and/or the good weather conditions for the entire region for this year.

The relative threshold method is more flexible and can deal with the diversity of situations at a larger scale. Density, cultivar, management practices are often quite different over large areas and absolute threshold might rapidly prove inaccurate. Therefore, the relative threshold was recommended for scaling up this product over large regions as fully documented in the report of WP34. To apply this method, it is however necessary to wait for a crop type product (report of WP44) because the parameters are currently crop-specific. This crop type product is generally available at the mid-season. Later on parameter values might probably be used for multiple crops but this would require further investigation. At the field level, this method might also help in detecting anomalies or within field spatial patterns relevant to precision agriculture.

The main drawback of the relative threshold is that it will output a result regardless of the real vegetation status. A combination of an absolute threshold discriminating bare and cropped soils with a relative threshold might prove useful. Furthermore, these threshold methods are also strongly impacted by a saw-tooth pattern of observation, which was very limited in this dataset. For more erratic observations, a logistic interpolation might prove very useful to smooth the index time-series.

It is also worth mentioning that the best method for emergence date detection depends on the application. Indeed, if one is interested in near-real time results, the time-lag value or the need to wait for the maximum value might be more decisive than the accuracy of the method to make a choice. One might prefer a method robust to outliers, or, on the contrary, a method that half of the time gives very accurate results. One might prefer a method that gives good relative results for a within field application and not valuing the exact emergence date estimation.

**Table 5-4: Comparison of the calibration and monthly samples for all methods for MSAVI**

MSAVI			
	calib	monthly sample	
Highest slope	SD	13.6	10.7
	MAD	8.9	8.9
Inflection point	SD	19.7	9.4
	MAD	7.4	8.9
Base logistic	SD	14.1	17.5
	MAD	13.3	17.8
Maximum value	SD	17.6	13.0
	MAD	19.3	14.8
Absolute threshold (linear interpolation)	SD	10.8	9.8
	MAD	8.9	8.9
	min	SD	SD
Relative threshold (linear interpolation)	SD	9.8	9.0
	MAD	7.4	5.9
	min	SD	SD

Absolute threshold (logistic interpolation)	SD	10.2	9.1
	MAD	11.9	10.4
	min	SD	MAD
Relative threshold (logistic interpolation)	SD	9.4	8.5
	MAD	7.4	7.4
	min	SD	MAD

The emergence date map for the demonstration site highlighted an underlying east-west emergence gradient with earlier emergence date in the east (Figure 5-31). On average, fields in the west are planted 45 days later than fields in the east. Besides, in the same location, fields also present some diversity in the emergence date. Pivot irrigation fields in the western area tend to be planted earlier in the season in comparison to rainfed agriculture, in advance of 16 days on average.

The spatial consistency of the results at pixel level provided by the relative threshold allows investigating also the spatial patterns within a field. Indeed relevant and interesting patterns which could not be validated are illustrated for six fields (Figure 5-32) and could be of interest for field monitoring or precision agriculture for instance.

Last but not least, the plant density and the crop row width vary over large regions according to local agriculture practices and meteorological conditions (dry year, drought, etc.). Their respective influence on the NDVI has been assessed carefully and was found rather negligible.

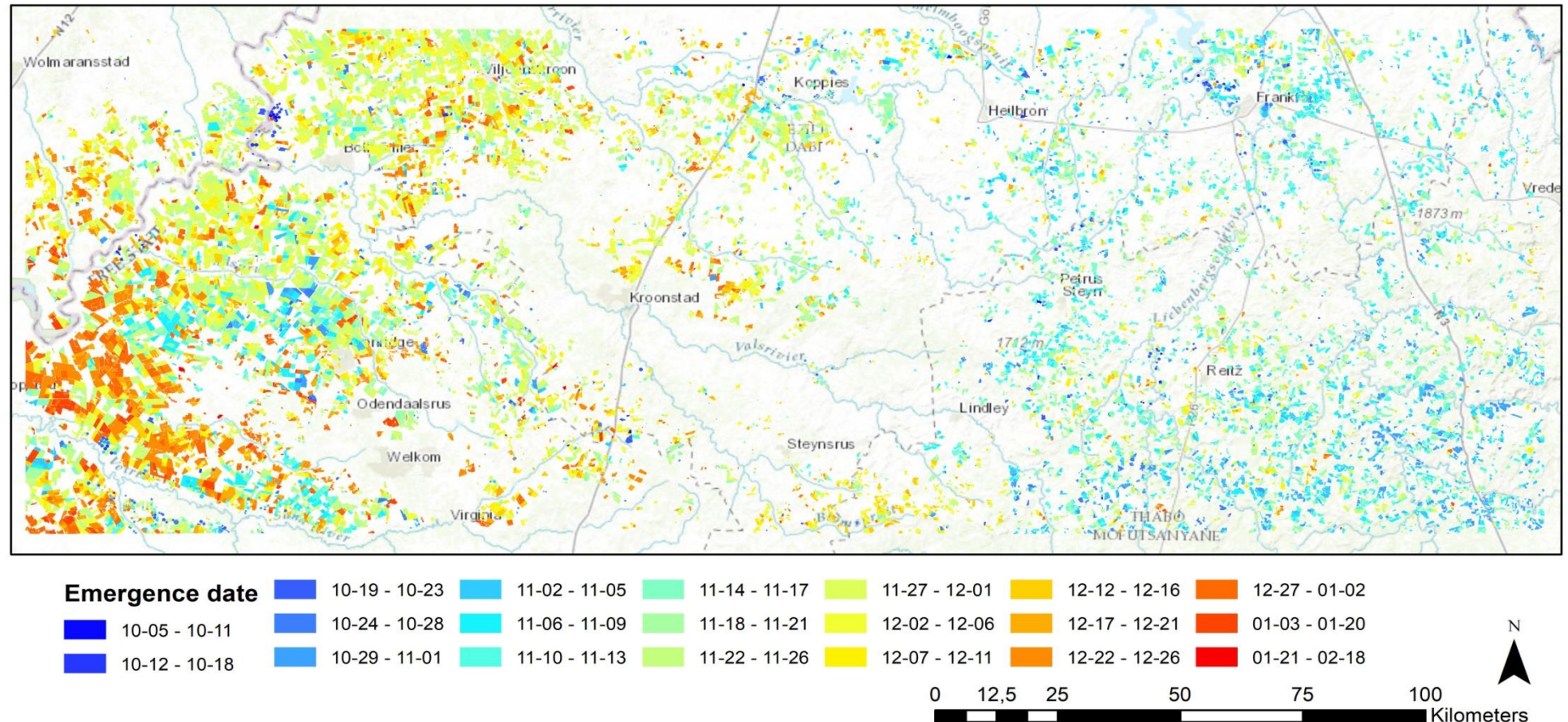
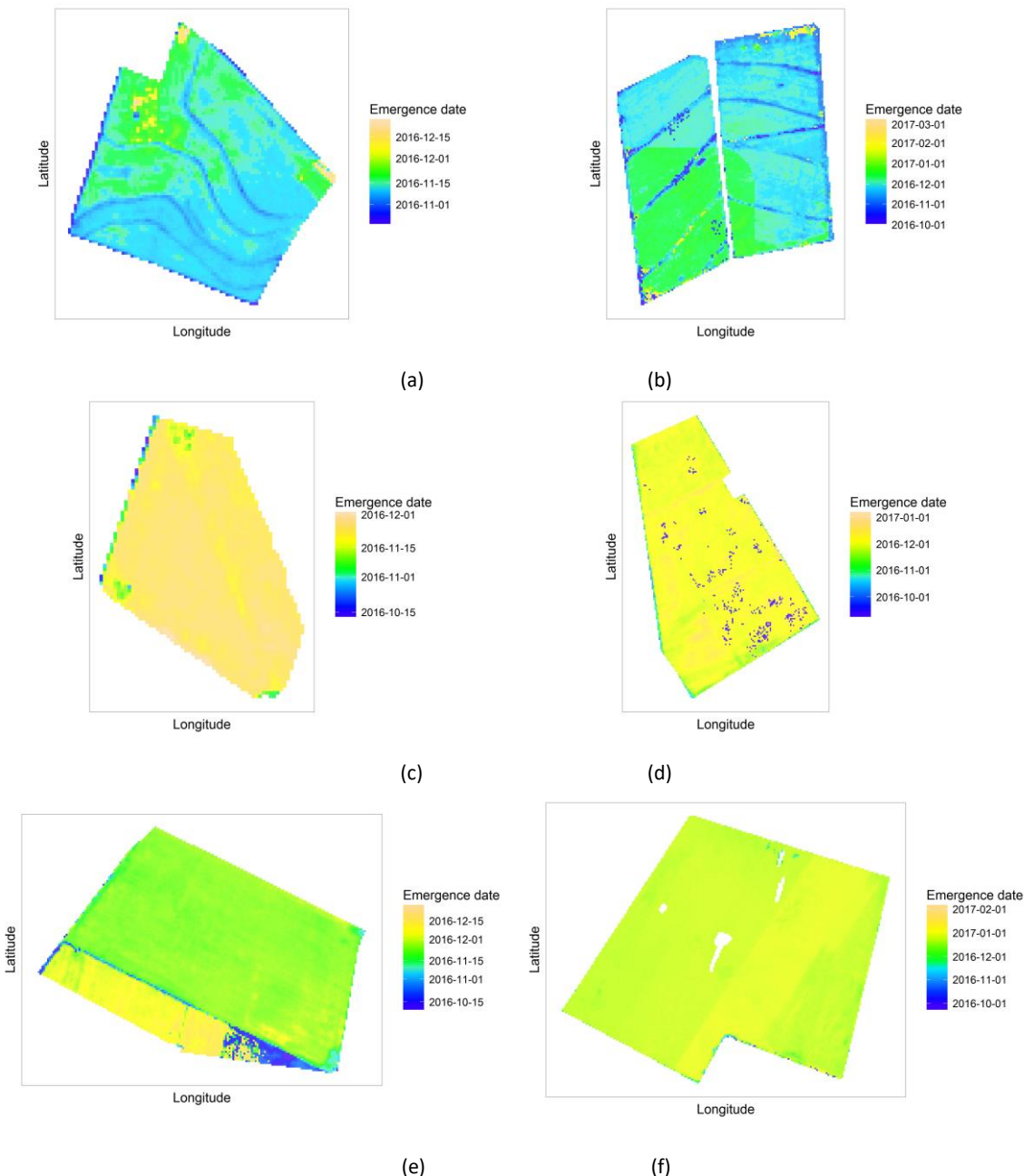


Figure 5-31: Emergence date map for maize in the Free State (South-Africa). A strong gradient of emergence date is highlighted from east to west



**Figure 5-32: Within field emergence date provided at pixel level for six maize fields of the Free State.**

In the phase 2, three main elements have been added: another year for maize in South-Africa, a new crop in South-Africa, and the implementation in the demo-site West.

The method findings and the performances are really very similar (2016-2017 and 2015-2016). It shows that similar accuracies were obtained for the two years, with the relative threshold method on logistic interpolation yielding the most accurate results with a SD of 10.9 days and a MAD of 5.9 days, to be compared to 9.3 and 7.4 days respectively. These results were, however, obtained, adjusting the optimal thresholds values for each year.

The differences between the two years might be explained by the very contrasting weather conditions; 2015-2016 has been marked by a severe drought, very difficult conditions to sow the fields and a delayed planting time while 2016-2017 was a rainy and green season with overall good weather conditions.

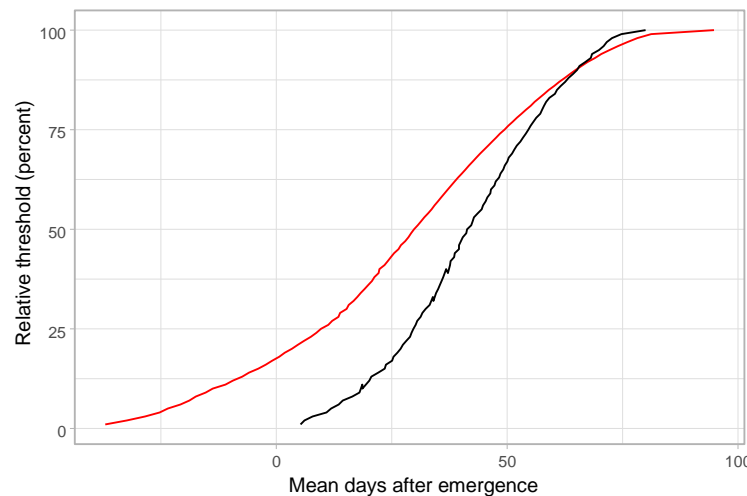


**Figure 5-33: Temporal dynamics of the MSAVI index for the 2016-2017 (red) and 2015-2016 (black) growth seasons. Results are presented for the relative threshold method on logistic interpolation**

In the phase 2, an additional main crop, i.e. sunflower, has been tested using the method established for the maize, calibrated and validated with a more limited number (88 for calibration and 39 for validation). As for maize, the same Relative Threshold method performed the best for sunflower and the SD and MAD are very similar. MSAVI yields the most accurate results with the relative threshold on linear interpolation outperforming the other methods with a SD of [11.7-9.9] days and a MAD of [7.4-7.4] days.

**Table 5-5 Sunflower results for all estimation methods. Results are expressed in days. Results for LAI on logistic interpolation are not presented. The min/bias row corresponds for the calibration sample to the indicator (SD or MAD) which is minimized while bias is the difference between the zero-mean expected validation and validation emergence date estimation.**

		MSAVI		NDVI		Hue index		LAI	
		calib	valid	calib	valid	calib	valid	calib	valid
Inflection point	SD	19.4	17.9	15.1	16.4	22.6	10.9		
	MAD	11.9	11.9	10.4	11.9	13.3	7.4	Not applicable	
	Time-lag	19.8	21.4	25.1	26.0	16.4	14.8		
Base logistic	SD	20.7	16.0	17.6	11.6	26.5	19.1		
	MAD	17.8	13.3	11.9	14.8	14.8	5.2	Not applicable	
	Time-lag	-12.2	-6.0	-2.3	-2.9	-10.2	-4.5		
Maximum value	SD	15.9	18.6	15.8	18.3	17.8	21.5	31.7	35.1
	MAD	15.6	16.3	16.3	18.5	17.0	20.0	19.3	31.1
	Time-lag	77.7	74.8	77.2	76.1	78.0	72.3	35.8	48.6
Absolute threshold (linear interpolation)	SD	15.5	12.1	17.5	13.0	16.7	23.2	25.2	25.9
	MAD	8.9	7.4	8.2	8.9	14.8	16.3	25.2	26.7
	Time-lag	8.35		9.6		19.2		-32.1	
	min/bias	SD	2.4	SD	2.2	SD	-3.6	SD	-0.5

	<b>SD</b>	<b>11.7</b>	<b>9.9</b>	<b>13.2</b>	<b>11.6</b>	<b>13.3</b>	<b>14.1</b>	<b>27.5</b>	<b>34.3</b>
<b>Relative threshold</b>	<b>MAD</b>	<b>7.4</b>	<b>7.4</b>	<b>8.9</b>	<b>6.7</b>	<b>9.6</b>	<b>12.6</b>	<b>22.9</b>	<b>40.0</b>
<b>(linear interpolation)</b>	<b>Time-lag</b>	<b>24.6</b>		<b>26.5</b>		<b>36.5</b>		<b>-15.1</b>	
	min/bias	SD	-1.2	MAD	-0.9	SD	-0.2	SD	-5.8
	SD	15.3	10.8	11.8	11.7	15.9	15.4		
Absolute threshold	MAD	19.3	10.4	14.1	8.9	13.3	14.1	Not appl	
(log. interpolation)	Time-lag	8.7		22.2		21.3			cable
	min/bias	SD	2.9	SD	1.2	SD	-3.6		
	SD	13.3	10.0	11.7	13.1	16.3	14.3		
Relative threshold	MAD	10.4	8.9	10.4	14.8	13.3	11.1		
(log. interpolation)	Time-lag	19.6		24.4		20.7			Not applicable
	min/bias	SD	2.3	SD	0.9	SD	3.1		
	SD	15.2	12.7	18.2	14.2	18.9	12.5	15.1	12.7
Highest slope	MAD	9.6	12.6	11.9	14.8	11.9	15.6	14.1	13.3
	Time-lag	24.6	23.9	23.9	23.4	19.8	21.8	22.3	21.1

In the phase 2, the emergence date detection method developed in South-Africa has been implemented for all the maize fields in the demo-site West (Belgian tiles). The performance of the method was assessed graphically based on the visual analysis of the field profiles as illustrated at the Figure 5-34.

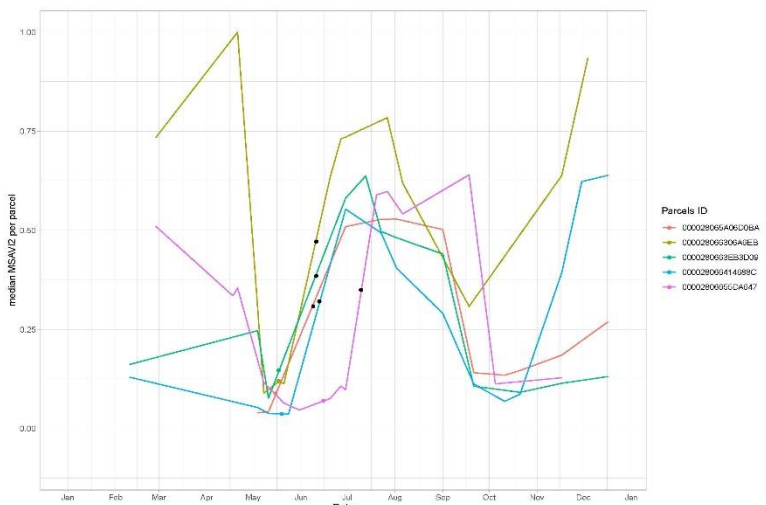


**Figure 5-34: Profile of five maize fields showing the MSAVI average value at field level, the maximum slope point and the detected emergence dates.**

The map of the maize emergence date appears very spatially consistent (Figure 5-35). The bulk of the date distribution is matching the agricultural practices: the sowing date ranges from 20 April till 16 May and the emergence occurs typically 5 to 15 days after sowing. The central part of the area showed the earlier mergence date while the most western fields was the latest. While the detected dates seems quite realistic, a formal quantitative validation is also required. Unfortunately, no precise emergence date observation was available for the demo-site West.

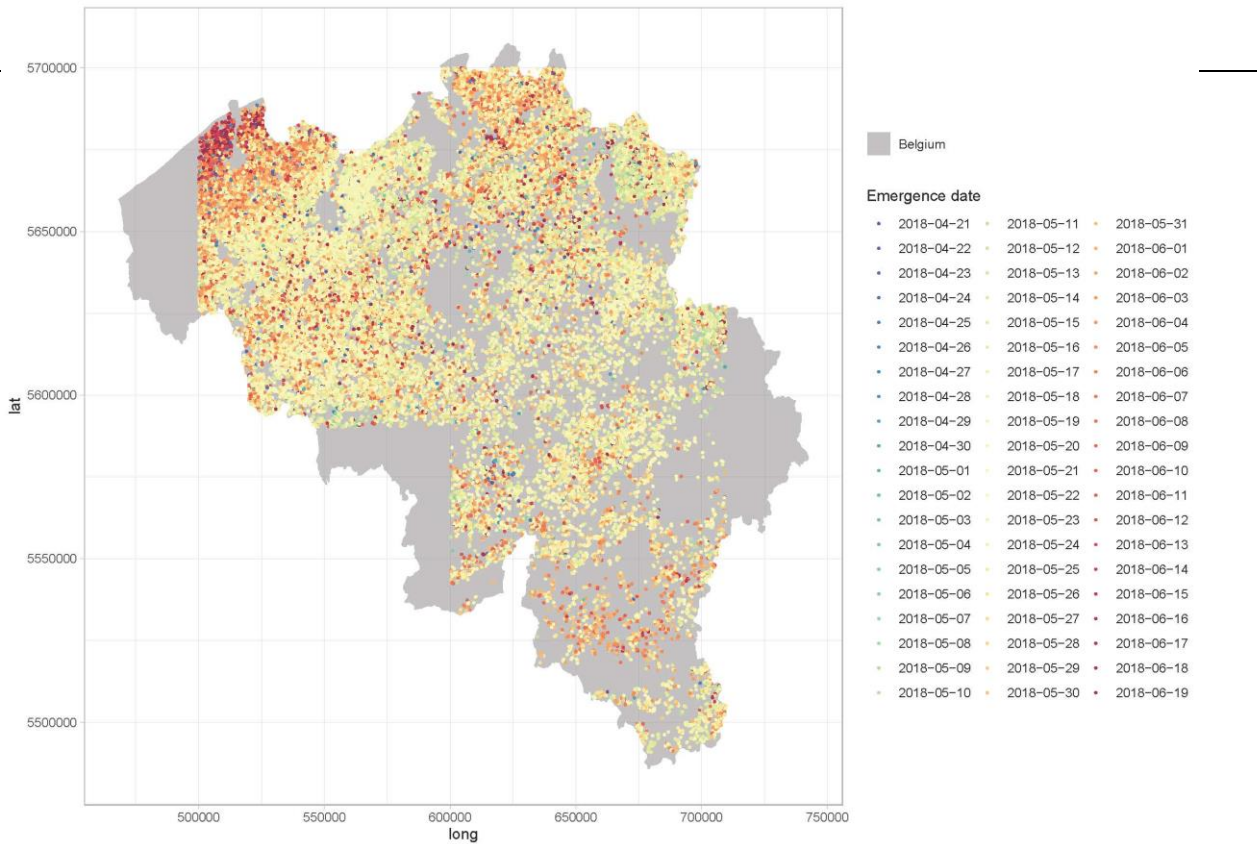


Figure 5-35: Spatial distribution of the maize emergence date in 2018 for the demo-site West (Belgian tiles).

### 5.3 Prototype Specifications

Unlike other prototypes, the phenological products correspond to new services highly required by several key stakeholders. The multiple use of these products makes even more important to work on the harmonization of the specifications between the different phenological products. The maturity of the different prototypes are not at the same level. The local LAI anomaly prototypes and the phenological metrics are matured while the emergence date is only validated and mature for South-Africa. Therefore, it is still early to define precisely all the prototype specifications. Indeed, the recent availability of S-2a and b time series did not allow to run the prototypes on a multi-year approach which is critical for some phenological products.

This section provides a description of the dataset properties and metadata for the implemented prototypes, also referring to “P41.2a - Data Sets of Time Series Derived Indicators and Variables Products”.

The raster products of the ECoLaSS prototypes are delivered as GeoTIFF (\*.tif) with world file (\*.tfw), pyramids (\*.ovr), attribute table (\*.dbf) and statistics (\*.aux.xml), enabling an instant illustration and analysis of the products within Geographic Information System (GIS) software. Each product is accompanied with a product-specific colour table (\*.clr) and INSPIRE-compliant metadata in XML format, and includes the probability layer as an additional raster.

Metadata are provided together with the products as INSPIRE-compliant XML files according to the EEA Metadata Standard for Geographic Information (EEA-MSGI). EEA-MSGI has been developed by EEA to meet needs and demands for inter-operability of metadata. EEA’s standard for metadata is a profile of the ISO 19115 standard for geographic metadata and contains more elements than the minimum required to comply the INSPIRE metadata regulation. Detailed conceptual specifications on EEA-MSGI and other relevant information on metadata can be found at <http://www.eionet.europa.eu/gis>.

Within ECoLaSS, a standardised and harmonised product file naming convention for all prototypes has been developed which is oriented along the already existing naming convention of the CLMS High Resolution Layers. This file naming convention has been applied to all raster prototypes and associated reference files and is documented in the Deliverables of Task 4.

The naming convention consists of the following 7 descriptors:

THEME    YEAR    RESOLUTION    EXTENT    EPSG    TYPE    VERSION  
as follows:

#### THEME

3 letter abbreviation for main products (CGC “crop growth condition”, CED “crop emergence date”).

#### REFERENCE YEAR

2017 in four digits; change products in four digits (e.g. 1517)

#### RESOLUTION

Four-digit (020m and 010m for raster or VECT for vector)

#### EXTENT

2-digit code for demonstration-sites (CE (central), NO (north), WE (west), SW (southwest), SE (southeast), SA (South Africa), ML (Mali))

#### EPSG

5-digit EPSG code (geodetic parameter dataset code by the European Petroleum Survey Group) “03035” for the European LAEA projection

#### TYPE

prototype

#### VERSION

3-digit code “v01”

#### EXAMPLE:

“DLT\_2017\_010m\_NO\_03035\_prototype\_v01.tif” stands for: Dominant Leaf Type, 2017 reference year, 10m, Demonstration-site North, European projection (EPSG: 3035), prototype, version 01

“TCC\_1517\_020m\_NO\_03035\_prototype\_v01.tif” stands for: Tree Cover Change, 2015-2017 change period, 20m, Demonstration-site North, European projection (EPSG: 3035), prototype, version 01

The following 29 prototypes files as part of **D11.4 – P41.2b – Data Sets of Time Series-derived Indicators and Variables (Issue 2)** in the demosites Central, South West and South Africa were submitted:

- PHL\_2018\_010m\_CE\_03035\_prototype\_v01.tif
- TSI\_CONIF\_2016-2019\_020m\_CE\_03035\_prototype\_v01.tif
- TSI\_CONIF\_2017\_020m\_CE\_03035\_prototype\_v01.tif
- TSI\_CONIF\_2018\_020m\_CE\_03035\_prototype\_v01.tif
- TSI\_CONIF\_2019\_020m\_CE\_03035\_prototype\_v01.tif
- TSI\_DECID\_2016-2019\_020m\_CE\_03035\_prototype\_v01.tif
- TSI\_DECID\_2017\_020m\_CE\_03035\_prototype\_v01.tif
- TSI\_DECID\_2018\_020m\_CE\_03035\_prototype\_v01.tif

- TSI\_DECID\_2019\_020m\_CE\_03035\_prototype\_v01.tif
- TSI\_GRA\_2016-2019\_020m\_CE\_03035\_prototype\_v01.tif
- TSI\_GRA\_2017\_020m\_CE\_03035\_prototype\_v01.tif
- TSI\_GRA\_2018\_020m\_CE\_03035\_prototype\_v01.tif
- TSI\_GRA\_2019\_020m\_CE\_03035\_prototype\_v01.tif
- EMD\_1617\_010m\_SA\_32735\_prototype\_v01.tif
- PHL\_2018\_010m\_SW\_03035\_prototype\_v01.tif
- EMD\_2018\_010m\_WE\_03035\_prototype\_v01.tif
- LAM\_2018\_010m\_WE\_03035\_prototype\_v01.tif
- TSI\_CONIF\_2016-2019\_020m\_WE\_03035\_prototype\_v01.tif
- TSI\_CONIF\_2017\_020m\_WE\_03035\_prototype\_v01.tif
- TSI\_CONIF\_2018\_020m\_WE\_03035\_prototype\_v01.tif
- TSI\_CONIF\_2019\_020m\_WE\_03035\_prototype\_v01.tif
- TSI\_DECID\_2016-2019\_020m\_WE\_03035\_prototype\_v01.tif
- TSI\_DECID\_2017\_020m\_WE\_03035\_prototype\_v01.tif
- TSI\_DECID\_2018\_020m\_WE\_03035\_prototype\_v01.tif
- TSI\_DECID\_2019\_020m\_WE\_03035\_prototype\_v01.tif
- TSI\_GRA\_2016-2019\_020m\_WE\_03035\_prototype\_v01.tif
- TSI\_GRA\_2017\_020m\_WE\_03035\_prototype\_v01.tif
- TSI\_GRA\_2018\_020m\_WE\_03035\_prototype\_v01.tif
- TSI\_GRA\_2019\_020m\_WE\_03035\_prototype\_v01.tif

**Table 5-6: Detailed specifications for primary CGC status layer of the demonstration site West**

Crop Growth Condition	Acronym	Product category			
CGC_2017_VECT_WE_03035_prototype_v01.shp	CGC	Primary Status Layer			
<b>Reference year</b>					
2017					
<b>Extent</b>					
Demonstration site West					
<b>Geometric resolution</b>					
Vector layers					
<b>Coordinate Reference System</b>					
European ETRS89 LAEA projection					
<b>Geometric accuracy (positioning scale)</b>					
LPIS geometric standards					
<b>Thematic accuracy</b>					
NA					
<b>Data type</b>					
Shapefile with float 32-bits for attribute					
<b>Minimum mapping unit (MMU)</b>					
LPIS MMU					
<b>Necessary attributes</b>					
LAI anomaly					
<b>Attribute coding (Thematic attribute values)</b>					
Real-signed values					
<b>Metadata</b>					
XML metadata files are to be produced according to INSPIRE metadata standards					
<b>Delivery format</b>					
Shapefile					
<b>Colour Table</b>					
ArcGIS *.lyr format					
Class Name	Red	Green	Blue		
Sever Negative Anomaly “anomaly < -2”	255	46	46		
Light Negative Anomaly “-2 <= anomaly < -1”	255	149	0		
No Anomaly “-1 <= anomaly < =1”	240	240	240		
Light Positive Anomaly “1 < anomaly < = 2”	128	255	0		
Severe Positive Anomaly “anomaly > 2 ”	0	82	0		

**Table 5-7: Detailed specifications for primary CED status layer of the demonstration site South-Africa**

Crop Emergence Date	Acronym	Product category
CED_2017_VECT_SA_32735_prototype_v01.shp	CED	Primary Status Layer
<b>Reference year</b>		
2016-2017		
<b>Extent</b>		
Demonstration site South-Africa		
<b>Geometric resolution</b>		
Vector layers		
<b>Coordinate Reference System</b>		
WGS84 - UTM zone 35 South		
<b>Geometric accuracy (positioning scale)</b>		
LPIS geometric standards		
<b>Thematic accuracy</b>		
NA		
<b>Data type</b>		
Shapefile with integer 16-bits for attribute		
<b>Minimum mapping unit (MMU)</b>		
LPIS MMU		
<b>Necessary attributes</b>		
Emergence		
<b>Attribute coding (Thematic values)</b>		
Integer values		
<b>Metadata</b>		
XML metadata files are to be produced according to INSPIRE metadata standards		
<b>Delivery format</b>		
Shapefile		
<b>Colour Table</b>		
ArcGIS *.lyr format		

**Table 5-8: Detailed specifications for PHL of the demonstration site South-West**

Crop Emergence Date	Acronym	Product category
PHL_2018_010m_SW_03035_prototype_v01	PHL	Phenological Layer
<b>Reference year</b>		
2018		
<b>Extent</b>		
Demonstration site South-West		
<b>Geometric resolution</b>		
10 meters		
<b>Coordinate Reference System</b>		
European ETRS89 LAEA projection		
<b>Geometric accuracy (positioning scale)</b>		
LPIS geometric standards		
<b>Thematic accuracy</b>		
NA		
<b>Data type</b>		
GeoTIFF with attribute table		
<b>Minimum mapping unit (MMU)</b>		
LPIS MMU		
<b>Necessary attributes</b>		
Istartgrow, startgrowt, endgrowth, max, startdecre, enddecreas		
<b>Attribute coding (Thematic values)</b>		
float values		
<b>Metadata</b>		
XML metadata files are to be produced according to INSPIRE metadata standards		
<b>Delivery format</b>		
Geotiff		
<b>Colour Table</b>		
ArcGIS *.lyr format		

**Table 5-9: Detailed specifications for the Time Series Indicator prototypes.**

Time Series Indicator	Acronym	Product category			
	TSI	Primary Status Layer			
<b>Reference year</b>					
2018					
<b>Geometric resolution</b>					
Pixel resolution 20m x 20m, fully conform with the EEA reference grid					
<b>Coordinate Reference System</b>					
European ETRS89 LAEA projection					
<b>Geometric accuracy (positioning scale)</b>					
Less than half a pixel. According to ortho-rectified satellite image base delivered by ESA.					
<b>Thematic accuracy</b>					
NA					
<b>Data type</b>					
8bit unsigned raster with LZW compression					
<b>Minimum Mapping Unit (MMU)</b>					
Pixel-based (0.5ha)					
<b>Necessary attributes</b>					
Raster value, count, class name, area (in km <sup>2</sup> ), area percentage (taking outside area not into account)					
<b>Raster coding (thematic pixel values)</b>					
0: no-change					
1: potential change, 1 <sup>st</sup> degree					
2: potential change, 2 <sup>nd</sup> degree					
255: not HRL class or background					
<b>Metadata</b>					
XML metadata files according to INSPIRE metadata standards					
<b>Delivery format</b>					
GeoTIFF					
<b>Colour table</b>					
ArcGIS *.clr format					
Class Code	Class Name	Red	Green	Blue	
0	all non-grass areas	215	215	215	
1	potential change, 1 <sup>st</sup> degree	255	128	0	
2	potential change, 2 <sup>nd</sup> degree	186	0	0	
255	not HRL class or background	0	0	0	

In addition to the prototype layers, probability layers are provided as a by-product where it applies. The additional raster in the product folder serves as one of the accuracy parameters that are described in detail in the WP33 final report [AD07] and range from 0 to 100%. The higher the percentage the higher the probability is that the respective pixel belongs to the depicted class. In this manner, the probability band depicts the error map at pixel level. Further, areas that are excluded by the referring mask get the value “101”. An overview of the probabilities’ colour palette is given in Table 5-10.

**Table 5-10: Colour palette for the probability layers**

Probabilities					
Class Code	Class Name	Red	Green	Blue	
0-100	Probabilities 0-100%	-	-	-	
101	Areas excluded by binary Mask	128	128	128	
255	Outside Area	0	0	0	

## 6 Conclusion and Outlook

As reported by the Deliverable D3.1: “D21.1a – Service Evolution Requirements Report”, the phenology and the agriculture services are two thematic gaps in the current Copernicus Land Service portfolio. The most frequently voiced new service was indeed a pan-European Agricultural Service, followed by a pan-European Phenology Layer. As expected, these two services are potentially interlinked as the phenology prototype allow capturing the growth cycle of the different crop types in a relevant manner for agriculture monitoring.

This Deliverable describes the methods developed and applied on the Demonstration site West for determining first generic land cover metrics, then crop growth conditions, and finally multiannual trends and potential changes for the specific changes of land covers, i.e. the HRL Grassland and Forest layers. The prototype dealing with the multiannual trends and potential change detection is based on S-1 time series. The prototypical implementation of these phenological products has been achieved on the Demonstration site West.

For the generic land cover metrics, in this second phase, the methodology has been improved in order to cut any manual step, leading to a much more accurate determination of key parameters of the seasonality, in line with the recent ITT on High resolution Vegetation Phenology. It can be noted that the identification of different land cover classes based on vegetation behaviors through the year is an interesting alternative to the traditional segmentation algorithms, and the geometry of the prototypes generated in this second phase have been used as “soft bones” for the creation of the NLC vector products.

In the perspective of updating the Grassland and Forest HRLayers, a more targeted phenological product has been designed to capture the multi-annual trends and the potential changes to be updated in the HRLs. The method relies on the detection of marginal behaviour of the statistical metrics computed from S-1 time series. Three time series corresponding to three years have been processed to highlight the potential changes in the Grassland HRL on one hand and in the Forest HRL on the other hand. While the density of S-1 time series is very interesting, the signal sensitivity to various elements other than change would require to develop additional filters.

The two other phenological prototypes implemented in the phase 1 are directly related to agriculture. The crop growth condition product has been developed and applied to the Demonstration site West for three different crop types (winter wheat, winter barley and maize). The time series of the LAI biophysical variables derived from the S-2 time series, is analysed at field level in relative terms with regards to the neighbouring fields of the same crop (within a radius of 3 km). This product allows to identify local marginal behaviour along the season in terms of crop growth cycle, crop development or management practices. An example of quantitative anomaly derived from the comparison between the LAI profile of each field with its surrounding ones provide a wall-to-wall map of the local growth cycle deviation.

A last phenological prototype concerns the emergence date product for the maize crop in the Demonstration site South Africa. Thanks to a comprehensive methods benchmarking based on a large reference dataset collected on the ground, the relative threshold method has been identified as the most suitable in terms of performance and robustness and applied to a large part of the Free State (South Africa). The validation concluded to an already satisfactory performance while it will necessary improved thanks to the Sentinel-2b availability in the forthcoming years.

In brief, the potential of the Sentinel time series has been clearly demonstrated to provide relevant phenological products. The developed prototype still requires some additional tuning to be considered as candidate for Copernicus services. Thanks to the promising results already obtained or demonstrated, the current availability of S-2a and b time series and the high priority requirements for these phenological products, the phase 2 will focus on the exploitation of the full potential of S-2 and S-1 for the phenological products demonstrating prototype ready for a future implementation potential in the Copernicus environment.

## References

- Ahmadian, Nima et al. (2016). "A New Concept of Soil Line Retrieval from Landsat 8 Images for Estimating Plant Biophysical Parameters". In: *Remote Sensing* 8.9, p. 738 (cit. on pp. 26, 27).
- Atzberger, Clement (2013). "Advances in Remote Sensing of Agriculture: Context Description, Existing Operational Monitoring Systems and Major Information Needs". In: *Remote Sensing* 5.2, pp. 949–981 (cit. on pp. 13, 14, 16).
- Balzter, Heiko et al. (2007). "Coupling of Vegetation Growing Season Anomalies and Fire Activity with Hemispheric and Regional-Scale Climate Patterns in Central and East Siberia". In: *Journal of Climate* 20.15, pp. 3713–3729 (cit. on p. 18).
- Baret, Frédéric and Samuel Buis (2008). "Estimating Canopy Characteristics from Remote Sensing Observations: Review of Methods and Associated Problems". In: *Advances in land remote sensing: system, modelling, inversion and application*. Ed. by Shunlin Liang. OCLC: 255604777. S.l.: Springer, pp. 173–201 (cit. on pp. 22, 23).
- Baret, Frédéric et al. (1986). "Contribution au suivi radiométrique de cultures de céréales". OCLC: 490210643. PhD thesis. S.l.: [s.n.] (cit. on p. 25).
- Battude, Marjorie et al. (2016). "Estimating maize biomass and yield over large areas using high spatial and temporal resolution Sentinel-2 like remote sensing data". In: *Remote Sensing of Environment* 184, pp. 668–681 (cit. on pp. 19, 28).
- Berjón, A. J. et al. (2013). "Retrieval of biophysical vegetation parameters using simultaneous inversion of high resolution remote sensing imagery constrained by a vegetation index". In: *Precision Agriculture* 14.5, pp. 541–557 (cit. on pp. 13, 14, 16, 23).
- Bernardi, Michele et al. (2016). *Crop Yield Forecasting: Methodological and Institutional Aspects (FAO)*. Food and Agriculture Organization (cit. on p. 37).
- Brown, M.E., K.M. de Beurs, and M. Marshall (2012). "Global phenological response to climate change in crop areas using satellite remote sensing of vegetation, humidity and temperature over 26 years". In: *Remote Sensing of Environment* 126, pp. 174–183 (cit. on pp. 19, 20, 72).
- Bsaibes, Aline et al. (2009). "Albedo and LAI estimates from FORMOSAT-2 data for crop monitoring". In: *Remote Sensing of Environment* 113.4, pp. 716–729 (cit. on p. 38).
- Cable, Jeffrey et al. (2014). "Agricultural Monitoring in Northeastern Ontario, Canada, Using MultiTemporal Polarimetric RADARSAT-2 Data". In: *Remote Sensing* 6.3, pp. 2343–2371 (cit. on p. 25).
- Campos-Taberner, Manuel et al. (2016). "Multitemporal and multiresolution leaf area index retrieval for operational local rice crop monitoring". In: *Remote Sensing of Environment* 187, pp. 102–118 (cit. on pp. 16, 24, 27).
- Che, Mingliang et al. (2014). "A New Equation for Deriving Vegetation Phenophase from Time Series of Leaf Area Index (LAI) Data". In: *Remote Sensing* 6.6, pp. 5650–5670 (cit. on pp. 13, 20, 24).
- Chen, Zhongxin et al. (2008). "Monitoring and management of agriculture with remote sensing". In: *Advances in land remote sensing: system, modelling, inversion and application*. Ed. by Shunlin Liang. OCLC: 255604777. S.l.: Springer, pp. 397–421 (cit. on pp. 13, 14, 28).
- Cong, Nan et al. (2013). "Changes in satellite-derived spring vegetation green-up date and its linkage to climate in China from 1982 to 2010: a multimethod analysis". In: *Global Change Biology* 19.3, pp. 881–891 (cit. on p. 18).
- Crop monitor for AMIS* (2016). 34. GEOGLAM (cit. on p. 72).
- De Bernardis, Caleb et al. (2016). "Particle Filter Approach for Real-Time Estimation of Crop Phenological States Using Time Series of NDVI Images". In: *Remote Sensing* 8.7, p. 610 (cit. on pp. 14, 22).
- de Beurs, Kirsten M. and Geoffrey M. Henebry (2010). "Spatio-Temporal Statistical Methods for Modelling Land Surface Phenology". In: *Phenological Research*. Ed. by Irene L. Hudson and Marie R. Keatley. Dordrecht: Springer Netherlands, pp. 177–208 (cit. on pp. 14, 16–20).
- Department of Agriculture, Forestry {and} Fisheries (DAFF) (2017). *Summary Commercial Crops database at the provincial level* (cit. on p. 33).

- Doktor, Daniel et al. (2014). "Extraction of Plant Physiological Status from Hyperspectral Signatures Using Machine Learning Methods". In: *Remote Sensing* 6.12, pp. 12247–12274 (cit. on p. 21).
- Duchemin, Benoît et al. (2008). "A simple algorithm for yield estimates: Evaluation for semi-arid irrigated winter wheat monitored with green leaf area index". In: *Environmental Modelling & Software* 23.7, pp. 876–892 (cit. on pp. 19, 24).
- Duveiller, Grégory, Frédéric Baret, and Pierre Defourny (2011a). "Crop specific green area index retrieval from MODIS data at regional scale by controlling pixel-target adequacy". In: *Remote Sensing of Environment* 115.10, pp. 2686–2701 (cit. on pp. 16, 24).
- Duveiller, Grégory et al. (2011b). "Retrieving wheat Green Area Index during the growing season from optical time series measurements based on neural network radiative transfer inversion". In: *Remote Sensing of Environment* 115.3, pp. 887–896 (cit. on p. 16).
- EEA. (2019). Call for tenders EEA/DIS/R0/19/007.
- Eilers, P. H. C. (2003). A Perfect Smoother. *Analytical Chemistry Journal*, 75(14), 3631-3636. doi: 10.1021/ac034173t
- Eklundh, Lars et al. (2003). "Investigating the use of Landsat thematic mapper data for estimation of forest leaf area index in southern Sweden". In: *Canadian Journal of Remote Sensing* 29.3, pp. 349–362 (cit. on pp. 15, 24).
- Esch, T., Üreyen, S., Zeidler, J., Metz-Marconcini, A., Hirner, A., Asamer, H., Tum, M., Böttcher, M., Kuchar, S., Svaton, V., & Marconcini, M. (2018). Exploiting big earth data from space – first experiences with the timescan processing chain. *Big Earth Data*, 2(1), 36-55. doi:10.1080/20964471.2018.1433790
- Gao, Bo-Cai (1996). "NDWI—A normalized difference water index for remote sensing of vegetation liquid water from space". In: *Remote sensing of environment* 58.3, pp. 257–266 (cit. on p. 15).
- Gitelson, Anatoly A. (2004). "Wide dynamic range vegetation index for remote quantification of biophysical characteristics of vegetation". In: *Journal of plant physiology* 161.2, pp. 165–173 (cit. on p. 15).
- Gessner, U.; Machwitz, M.; Esch, T.; Tillack, A.; Naeimi, V.; Kuenzer, C.; Dech, S. Multi-sensor mapping of West African land cover using MODIS, ASAR and TanDEM-X/TerraSAR-X data. *Remote Sens. Environ.* 2015, 164, 282–297.
- González-Sanpedro, M.C. et al. (2008). "Seasonal variations of leaf area index of agricultural fields retrieved from Landsat data". In: *Remote Sensing of Environment* 112.3, pp. 810–824 (cit. on pp. 16, 23, 24).
- Hagolle, O., & Morin, D. (2015). Design Justification File: benchmarking for L3 monthly composite product. Sen2Agri project. ESA.
- Hatfield, Jerry L. and John H. Prueger (2010). "Value of Using Different Vegetative Indices to Quantify Agricultural Crop Characteristics at Different Growth Stages under Varying Management Practices". In: *Remote Sensing* 2.2, pp. 562–578 (cit. on p. 27).
- Hoefsloot, Peter et al. (2012). *Combining crop models and remote sensing for yield prediction - concepts, applications and challenges for heterogeneous, smallholder environments: report of CCFAS-JRC Workshop at Joint Research Centre, Ispra, Italy, June 13-14, 2012*. OCLC: 878764318. Luxembourg: Publications Office (cit. on pp. 14, 16).
- Hosseini, Mehdi et al. (2015). "Estimation of Leaf Area Index (LAI) in corn and soybeans using multi-polarization C- and L-band radar data". In: *Remote Sensing of Environment* 170, pp. 77–89 (cit. on p. 16).
- Huete, A et al. (2002). "Overview of the radiometric and biophysical performance of the MODIS vegetation indices". In: *Remote Sensing of Environment* 83.1, pp. 195–213 (cit. on p. 15).
- Huetrich, C., Gessner, U., Herold, M., Strohbach, B. J., Schmidt, M., Keil, M., et al. (2009). On the suitability of MODIS time series metrics to map vegetation types in dry savanna ecosystems: A case study in the Kalahari of NE Namibia. *Remote Sensing*, 1, 620–643.
- Hüttich, Christian et al. (2009). "On the Suitability of MODIS Time Series Metrics to Map Vegetation Types in Dry Savanna Ecosystems: A Case Study in the Kalahari of NE Namibia". In: *Remote Sensing* 1.4, pp. 620–643 (cit. on p. 16).

- Islam, Akm Saiful and Sujit Kumar Bala (2008). "Assessment of Potato Phenological Characteristics Using MODIS-Derived NDVI and LAI Information". In: *GIScience & Remote Sensing* 45.4, pp. 454–470 (cit. on p. 15).
- Jager, J. M. de, A. B. Potgieter, and W. J. van den Berg (1998). "Framework for forecasting the extent and severity of drought in maize in the Free State Province of South Africa". In: *Agricultural Systems. Drought Policy, Assessment and Declaration* 57.3, pp. 351–365 (cit. on p. 33).
- Jain, Meha et al. (2016). "Mapping Smallholder Wheat Yields and Sowing Dates Using MicroSatellite Data". In: *Remote Sensing* 8.10, p. 860 (cit. on p. 29).
- Jiang, Zhangyan et al. (2007). "Interpretation of the modified soil-adjusted vegetation index isolines in red-NIR reflectance space". In: *Journal of Applied Remote Sensing* 1.1, pp. 013503–013503–12 (cit. on p. 15).
- Johann, Jerry A. et al. (2013). "Data mining techniques for identification of spectrally homogeneous areas using NDVI temporal profiles of soybean crop". In: *Engenharia Agrícola* 33.3, pp. 511–524 (cit. on p. 17).
- Jones, Matthew O. et al. (2012). "Satellite passive microwave detection of North America start of season". In: *Remote Sensing of Environment* 123, pp. 324–333 (cit. on p. 25).
- Jonsson, P., & Eklundh, L. (2002). Seasonality extraction by function fitting to time-series of satellite sensor data. *IEEE transactions on Geoscience and Remote Sensing*, 1824-1832.
- Kang, S (2003). "A regional phenology model for detecting onset of greenness in temperate mixed forests, Korea: an application of MODIS leaf area index". In: *Remote Sensing of Environment* 86.2, pp. 232–242 (cit. on p. 24).
- Klein, I., Gessner, U., & Kuenzer, C. (2012). Regional land cover mapping and change detection in Central Asia using MODIS time-series. *Applied Geography*, 35(1–2), 219–234.
- Koetz, Benjamin et al. (2005). "Use of coupled canopy structure dynamic and radiative transfer models to estimate biophysical canopy characteristics". In: *Remote Sensing of Environment* 95.1, pp. 115–124 (cit. on p. 23).
- Koyer, Hans-Werner, Parvaiz Ahmad, and Nicole Geissler (2012). "Abiotic Stress Responses in Plants: An Overview". In: *Environmental Adaptations and Stress Tolerance of Plants in the Era of Climate Change*. Ed. by Parvaiz Ahmad and M.N.V. Prasad. DOI: 10.1007/978-1-4614-0815-4\_1. New York, NY: Springer New York, pp. 1–28 (cit. on p. 14).
- Lauvernet, Claire (2005). "Variational assimilation of remote sensing data into canopy functioning models : use of the adjoint model and add of some spatial constraints." PhD thesis. Université Joseph-Fourier - Grenoble I (cit. on pp. 23, 25).
- Leys, Christophe et al. (2013). "Detecting outliers: Do not use standard deviation around the mean, use absolute deviation around the median". In: *Journal of Experimental Social Psychology* 49.4, pp. 764–766 (cit. on p. 48).
- Liu, Jiangui, Elizabeth Pattey, and Guillaume Jégo (2012). "Assessment of vegetation indices for regional crop green LAI estimation from Landsat images over multiple growing seasons". In: *Remote Sensing of Environment* 123, pp. 347–358 (cit. on pp. 23, 24, 27).
- Lobell, David B. et al. (2003). "Remote sensing of regional crop production in the Yaqui Valley, Mexico: estimates and uncertainties". In: *Agriculture, Ecosystems & Environment* 94.2, pp. 205–220 (cit. on p. 24).
- Lobell, David B. et al. (2013). "Satellite detection of earlier wheat sowing in India and implications for yield trends". In: *Agricultural Systems* 115, pp. 137–143 (cit. on p. 17).
- Lopez-Sanchez, J. M., S. R. Cloude, and J. D. Ballester-Berman (2012). "Rice Phenology Monitoring by Means of SAR Polarimetry at X-Band". In: *IEEE Transactions on Geoscience and Remote Sensing* 50.7, pp. 2695–2709 (cit. on pp. 14, 25, 26).
- Marinho, Eduardo et al. (2014). "From Remotely Sensed Vegetation Onset to Sowing Dates: Aggregating Pixel-Level Detections into Village-Level Sowing Probabilities". In: *Remote Sensing* 6.11, pp. 10947–10965 (cit. on pp. 28, 29, 31, 39).

- Meroni, M. et al. (2014). "Early detection of biomass production deficit hot-spots in semi-arid environment using FAPAR time series and a probabilistic approach". In: *Remote Sensing of Environment* 142, pp. 57–68 (cit. on p. 24).
- Merzlyak, Mark and Anatoly Gitelson (1995). "Why and What for the Leaves Are Yellow in Autumn? On the Interpretation of Optical Spectra of Senescing Leaves (*Acer platanoides L.*)" In: *Journal of Plant Physiology* 145, pp. 315–320 (cit. on p. 24).
- Moulin, Sophie et al. (1997). "Global-scale assessment of vegetation phenology using NOAA/AVHRR satellite measurements". In: *Journal of Climate* 10.6, pp. 1154–1170 (cit. on p. 18).
- Naylor, Rosamond (2011). "Expanding the boundaries of agricultural development". In: *Food Security* 3.2, pp. 233–251 (cit. on p. 13).
- Nguy-Robertson, Anthony L. et al. (2014). "Estimating green LAI in four crops: Potential of determining optimal spectral bands for a universal algorithm". In: *Agricultural and Forest Meteorology* 192-193, pp. 140–148 (cit. on pp. 15, 24).
- Njoku, Eni G., ed. (2014). *Encyclopedia of Remote Sensing*. Encyclopedia of Earth Sciences Series. DOI: 10.1007/978-0-387-36699-9. New York, NY: Springer New York (cit. on p. 15).
- Palacios-Orueta, Alicia et al. (2012). "Derivation of phenological metrics by function fitting to time-series of Spectral Shape Indexes AS1 and AS2: Mapping cotton phenological stages using MODIS time series". In: *Remote Sensing of Environment* 126, pp. 148–159 (cit. on pp. 15, 16, 19, 22).
- Peddle, D. R. and A. M. Smith (2005). "Spectral mixture analysis of agricultural crops: Endmember validation and biophysical estimation in potato plots". In: *International Journal of Remote Sensing* 26.22, pp. 4959–4979 (cit. on pp. 21, 26).
- Pekel, Jean-François et al. (2011). "Development and Application of Multi-Temporal Colorimetric Transformation to Monitor Vegetation in the Desert Locust Habitat". In: *IEEE Journal of Selected Topics in Applied Earth Observations and Remote Sensing* 4.2, pp. 318–326 (cit. on pp. 26–29, 40, 69).
- Pinty, B. et al. (2009). "On the need to observe vegetation canopies in the near-infrared to estimate visible light absorption". In: *Remote Sensing of Environment* 113.1, pp. 10–23 (cit. on p. 15).
- Province, Free State (2005). *Free State Province Provincial Growth and Development Strategy (PGDS) 2005–2014*. Bloemfontein, p. 18 (cit. on p. 33).
- Reed, Bradley C. et al. (1994). "Measuring phenological variability from satellite imagery". In: *Journal of Vegetation Science* 5.5, pp. 703–714 (cit. on pp. 17, 18, 28).
- Roberts, D. A., M. O. Smith, and J. B. Adams (1993). "Green vegetation, nonphotosynthetic vegetation, and soils in AVIRIS data". In: *Remote Sensing of Environment* 44.2, pp. 255–269 (cit. on p. 26).
- Rondeaux, Geneviève, Michael Steven, and Frédéric Baret (1996). "Optimization of Soil-Adjusted Vegetation Indices". In: *Remote Sensing of Environment* (cit. on pp. 26, 27).
- Sakamoto, Toshihiro et al. (2005). "A crop phenology detection method using time-series MODIS data". In: *Remote Sensing of Environment* 96.3, pp. 366–374 (cit. on pp. 19, 28).
- Sakamoto, Toshihiro et al. (2010). "A Two-Step Filtering approach for detecting maize and soybean phenology with time-series MODIS data". In: *Remote Sensing of Environment* 114.10, pp. 2146–2159 (cit. on pp. 13, 14, 16, 19, 21, 22, 78).
- Schulze, R.E. (2007). *South African Atlas of Climatology and Agrohydrology*. 1489/1/06. Pretoria, South Africa: Water Research Commission (cit. on p. 34).
- Schwartz, Mark D. and Jonathan M. Hanes (2010). "Intercomparing multiple measures of the onset of spring in eastern North America". In: *International Journal of Climatology* 30.11, pp. 1614–1626 (cit. on p. 20).
- Tits, Laurent et al. (2013). "Integration of in situ measured soil status and remotely sensed hyperspectral data to improve plant production system monitoring: Concept, perspectives and limitations". In: *Remote Sensing of Environment* 128, pp. 197–211 (cit. on p. 27).
- Tsubo, M. and S. Walker (2007). "An assessment of productivity of maize grown under water harvesting system in a semi-arid region with special reference to ENSO". In: *Journal of Arid Environments* 71.3, pp. 299–311 (cit. on p. 33).
- Tucker, Compton (1978). "Red and Photographic Infrared Linear Combinations for Monitoring Vegetation". In: (cit. on pp. 14, 15).

- USDA - National Agricultural Statistics Service (2016). URL: [https://www.nass.usda.gov/Publications/National\\_Crop\\_Progress/Terms\\_and\\_Definitions/](https://www.nass.usda.gov/Publications/National_Crop_Progress/Terms_and_Definitions/) (visited on 12/31/2016) (cit. on p. 28).
- Varmuza, Kurt and Peter Filzmoser (2016). *Introduction to Multivariate Statistical Analysis in Chemometrics*. Google-Books-ID: S4btqolgGPOC. CRC Press. 328 pp. (cit. on p. 47).
- Verhegghen, Astrid (2013). "Global land surface vegetation phenology using 13 years of SPOT VEGETATION daily observations". PhD thesis. Université catholique de Louvain (cit. on p. 18).
- Vicente-Guijalba, Fernando, Tomas Martinez-Marin, and Juan M. Lopez-Sanchez (2014). "Crop phenology estimation using a multitemporal model and a Kalman filtering strategy". In: *IEEE Geoscience and Remote Sensing Letters* 11.6, pp. 1081–1085 (cit. on pp. 13, 25).
- Vintrou, Elodie et al. (2014). "A Comparative Study on Satellite- and Model-Based Crop Phenology in West Africa". In: *Remote Sensing* 6.2, pp. 1367–1389 (cit. on p. 13).
- Vyas, Swapnil et al. (2013). "Extracting Regional Pattern of Wheat Sowing Dates Using Multispectral and High Temporal Observations from Indian Geostationary Satellite". In: *Journal of the Indian Society of Remote Sensing* 41.4, pp. 855–864 (cit. on p. 28).
- Wardlow, Brian D., Jude H. Kastens, and Stephen L. Egbert (2006). "Using USDA Crop Progress Data for the Evaluation of Greenup Onset Date Calculated from MODIS 250-Meter Data". In: *Photogrammetric Engineering & Remote Sensing* 72.11, pp. 1225–1234 (cit. on p. 29).
- Weiss, Marie et al. (2000). "Investigation of a model inversion technique to estimate canopy biophysical variables from spectral and directional reflectance data". In: *Agronomie* 20.1, pp. 3–22 (cit. on p. 23).
- Wessels, Konrad et al. (2011). "Remotely sensed vegetation phenology for describing and predicting the biomes of South Africa: Remotely sensed vegetation phenology of South Africa's biomes". In: *Applied Vegetation Science* 14.1, pp. 49–66 (cit. on p. 34).
- White, Michael A., Peter E. Thornton, and Steven W. Running (1997). "A continental phenology model for monitoring vegetation responses to interannual climatic variability". In: *Global Biogeochemical Cycles* 11.2, pp. 217–234 (cit. on pp. 15, 17).
- White, Michael A. et al. (2002). "Satellite Evidence of Phenological Differences Between Urbanized and Rural Areas of the Eastern United States Deciduous Broadleaf Forest". In: *Ecosystems* 5.3, pp. 260–273 (cit. on p. 28).
- Wiggs, Giles and Peter Holmes (2011). "Dynamic controls on wind erosion and dust generation on west-central Free State agricultural land, South Africa". In: *Earth Surface Processes and Landforms* 36.6, pp. 827–838 (cit. on p. 33).
- Wohlfart, C., Liu, G., Huang, C., Kuenzer, C., (2016). A River Basin over the Course of Time: Multi-temporal Analyses of Land Surface Dynamics in the Yellow River Basin (China) based on Medium Resolution Remote Sensing Data. *Remote Sens.* 8, 186, 1–25.
- Yang, Hao et al. (2014). "Temporal Polarimetric Behavior of Oilseed Rape (*Brassica napus* L.) at C-Band for Early Season Sowing Date Monitoring". In: *Remote Sensing* 6.11, pp. 10375–10394 (cit. on p. 25).
- Zadoks, Jan C., Ting T. Chang, and Cal F. Konzak (1974). "A decimal code for the growth stages of cereals". In: *Weed research* 14.6, pp. 415–421 (cit. on p. 14).
- Zeng, Linglin et al. (2016). "A hybrid approach for detecting corn and soybean phenology with time-series MODIS data". In: *Remote Sensing of Environment* 181, pp. 237–250 (cit. on pp. 13, 17, 19, 22, 28).
- Zhang, Xiaoyang et al. (2003). "Monitoring vegetation phenology using MODIS". In: *Remote sensing of environment* 84.3, pp. 471–475 (cit. on pp. 14, 20, 28).